

TRANSFORMATION AND STABILIZATION OF PLANT RESIDUE ORGANIC
NITROGEN

A Dissertation

Presented to the Faculty of the Graduate School

Of Cornell University

In Partial Fulfillment of the Requirements for the Degree of

Doctor of Philosophy

by

Dorisel Torres

©2018 Dorisel Torres

TRANSFORMATION AND STABILIZATION OF PLANT RESIDUE ORGANIC NITROGEN

Dorisel Torres, Ph.D.

Cornell University 2018

Plant residues are a promising source of carbon-neutral biomass that can be used to produce pyrogenic organic matter (PyOM) with small-scale pyrolysis systems. These residues can be considerably rich in nitrogen (N) and their thermal transformation through pyrolysis can serve as a mechanism of N retention in terrestrial ecosystems. This study focused on three main areas of the process transformation and stabilization of plant residue organic N; (1) the availability of plant residues for the production of PyOM; (2) the operating conditions of pyrolysis cookstoves which affect the production of C and N pollutants and heat transfer for cooking and (3) the thermal and biological transformation of organic N from plant residues.

In a plant residue resource availability analysis, a segmentation protocol was developed to evaluate the multiresolution segmentation (MRS) quality of an agricultural high resolution image. High quality image segmentation is essential for subsequent classification and quantification of plant residue availability. The main segmentation error occurred when an image object was missing in the segmentation layer. Missing objects can result in considerable over or underestimation of plant residue availability, depending on the final land cover classification.

The subsequent thermal conversion of plant residues was performed in an indirect pyrolysis cookstove. The rate of pyrolysis fuel consumption was the main driver of carbon monoxide (CO) and nitric oxide (NO) emissions and heat output of the stove accounting for up to 70% of the variation in multivariate linear regression analysis. Meaning that the speed of

cooking and the choice of fuel used, significantly affected the production of gaseous pollution while the amount of fuel used controlled the amount of heat produced for cooking.

Finally, the thermal transformation of organic matter nitrogen (OM-N) into PyOM-N was characterized using N near edge X-ray absorption fine structure. Our study revealed that the formation of aromatic N heterocycles was significantly correlated ($R^2=0.44$; $p<0.0001$) with the initial N content in uncharred OM. In an incubation study, PyOM-C mineralization was inhibited by aromatic N heterocycles found in extracted PyOM, while aromatic N heterocycles in oxygenated rings found in the PyOM extract promoted PyOM-C mineralization. These findings support that PyOM-C mineralization is affected by the molecular structure of N rather than N content or C:N ratio.

BIOGRAPHICAL SKETCH

Dorisel was born and raised in Puerto Rico. She is a Chemical Engineer and Horticulture graduate from the University of Puerto Rico, Mayagüez. She decided to pursue her career in Soil Sciences after working on an organic farm in California and serving as a volunteer for Global Services Corps in Tanzania. She conducted research for her master's degree in Biochar Systems for Smallholder farms in Kenya, under the supervision of Dr. Johannes Lehmann. She received her master's degree in 2011. Her experience working in developing nations offered Dori the opportunity to focus her career goals and subsequently led her to pursue her doctorate in Soil Sciences. She started her doctorate in the Lehmann lab after being awarded the NSF Graduate Research Fellowship in Food Systems and Poverty Reduction IGERT. Her doctorate research work took her back to Kenya and expanded on the research on biochar systems with a focus on resource use, energy and emissions and nitrogen and carbon in pyrogenic organic matter.

To Kevin and Max
The two loves of my life,
No matter what we do or where we end up, you will always be home

ACKNOWLEDGEMENTS

I would like to sincerely express my gratitude to Dr. Johannes Lehmann, my committee chair, for his support, guidance and patience during all these years of work. I would also like to thank Dr. Elizabeth Fisher and Dr. Allison Power, for the advice and amazing support which they both provided throughout the years of research and dissertation writing. I think they are amazing examples of women in science. My entire committee has been amazing, they never lost faith in seeing me through this process. Thanks for believing in me.

To Kevin, my partner in life, I lack enough words to express how blessed I am for all your support. Your faith in me never wavered even in the hardest moments. Your unconditional love and support kept me going through years of field work, lab research and writing. The last push of the doctorate might have been the hardest but I hope that from this moment on we find peace and move forward. Thanks for believing in me, sticking it through and helping me achieve my educational and career goals. I love you!!!!

I would also like to thank Maximiliano, the joy of my heart. I hope that someday you look at this and realize how hard I was working to be able to provide you the life that you deserve. You are a bright and amazing little boy and I can see you soaring high in life. My best advice to you is dream big and go for it. I am in awe of you right now and I am sure I always will. Thanks for being my awesome travel partner and thanks for being such a patience little boy that has allowed me to move him around while I try to finish my dissertation. I had a blast with you in Puerto Rico. You taught me to take in the world at a different pace and I absolutely love it.

I would like thank Akio Enders, for all the support he provided in the process of designing and executing experiments. And for holding the experimental fort when I was away

conducting field work in Kenya or other parts of the world. Many thanks to Kelly Hanley, who dealt with a lot of financial and technical logistics so I could complete my research. Thanks, to all the staff at ICRAF in Nairobi and Kisumu, who participated in the logistical support of field work in Western Kenya. I also want to thank the farmers who participated in the study; without their cooperation, support and participation none of this work would have been possible. I would like to also acknowledge my amazing field crew, Manoah Obwayo, Zablon Khatima, Julie Awour, Samuel Omollo, Nicolas Ochieng, Nicholas Otieno, Dominic Atundo, Moses Otieno, Brian Owiti, Andrew Osir, Azinapher Mideva, Fred, Willis Okatch. For two and half years this crew was my family. We spent every day together and worked side by side. This crew worked long and hard hours without complaining. The work they did was exceptional, we all learned together and from each other. They made me laugh and kept me on my toes. They will always hold a special place in my heart.

Finally, to Morgan Ruelle and Christian D. Guzman, I would like to say, thank you. For being true friends and colleagues. I appreciate the time you took to talk me through difficult times, to talk research and to read manuscripts. All the time we spent together during the IGERT and thereafter has allowed me to have a greater perspective on research, academia and life in general. I would like to also thank, Rachel Hestrin for being such an incredible editor of all the written materials I sent her during my doctorate work and an incredibly supportive friend.

Financial support was provided by National Science Foundation (NSF) -Integrative Graduate Education and Research Traineeship (IGERT) program and Cornell's Provost Diversity Fellowship. The research and travel for my dissertation was funded by Yossie Hollander and the Fondation des Fondateurs, Atkinson Center for a Sustainable Future- Cornell, NSF-BREAD (grant number IOS-0965336), NSF-IGERT, Environmental Protection Agency-P3 Student

Design Competition for Sustainability (grant number SU835341 and SU835548),
Biogeochemistry and Environmental Biocomplexity Research Award (BEB), Bradfield Award
from Cornell's Department of Soil and Crop Sciences and Mario Einaudi Center for International
Studies.

TABLE OF CONTENTS

BIOGRAPHICAL SKETCH	iii
ACKNOWLEDGEMENTS	v
TABLE OF CONTENTS	viii
LIST OF FIGURES	ix
LIST OF TABLES	xv
CHAPTER 1: OPTIMAL SEGMENTATION PARAMETERS FOR OBJECT-BASED IMAGE ANALYSIS: APPLICATION TO COMPLEX AGRICULTURAL LANDSCAPES	17
Abstract	17
1. Introduction	19
2. Description of study area and data	22
3. Methodology	24
4. Experimental results	32
5. Discussion	42
6. Conclusion	50
Acknowledgments	51
References	52
CHAPTER 2: CARBON AND NITROGEN EMISSIONS RATE AND HEAT TRANSFER OF AN INDIRECT PYROLYSIS BIOMASS COOKSTOVE	56
Abstract	56
1. Introduction	57
2. Materials and methods	59
3. Results and discussion	65
4. Conclusions	73
Acknowledgments	75
References	76
CHAPTER 3: THERMOCHEMICAL AND BIOLOGICAL TRANSFORMATION OF ORGANIC NITROGEN IN PLANT RESIDUES	81
Abstract	81
1. Introduction	83
2. Materials and Methods	86
3. Results	91
4. Discussion	105
5. Conclusion	110
Acknowledgements	111
References	112
APPENDIX A	117
APPENDIX B	129

LIST OF FIGURES

Figure 1. 1: Map of the study area and reference object data set. (a) The study area is located in western Kenya, within the Yala watershed (highlighted in yellow); (b) the mid-Yala block is located between the Kakamega and Vihiga districts and spans an area of 100km² and has a mixture of agricultural and forested land; (c) high resolution image (WV-2) 1km² grid and delineated reference polygons for different classes. 23

Figure 1.2: Workflow diagram for segmentation quality analysis. Methods and processing steps used for the analysis of image segmentation quality. 25

Figure 1.3: Schematic of image segmentation and the creation of image object segments. Segmentation process consists of multiple levels to create image objects. (a) Level 0, segmentation parameters are applied for the partitioning image and subsequent merging of similar regions based on the homogeneity between pixels; segments created at this level are candidate segments; (b) Level 1, image object criteria is applied to determine which segments correspond to the reference object; a candidate segment become a corresponding image object when 50% of its area is within the boundaries of the reference object; these are sub-objects with respect to the upper level of segmentation; (c) Level 2, the final object image object is created by merging all corresponding image object segments that compose the reference object. Topological and arithmetic measures are illustrated; (d) an object is undetected or missing when the image object and reference object do not correspond to the same class; (e) too many objects is caused by the over-partitioning of one reference object into numerous small image objects; (f) over- and under-segmentation happen when the image object either overextends beyond the boundaries of the reference object or the image object does not intersect the reference object in its entirety. 27

Figure 1.4: Geometric congruence indices. (a) Normalized area difference index and (b) Normalized perimeter difference index as a function of scale, shape for small and large field size class..... 33

Figure 1.5: Topological congruence indices. (a) Under-segmentation index and (b) Over-segmentation index variation as a function of scale and shape for small and large field size class. 36

Figure 1.6: Arithmetic congruence indices. (a) Too many objects index and (b) Undetected object index and (b) variation as a function of scale and shape for small and large field size class. 38

Figure 1.7: Overall segmentation quality index variation as a function of scale, shape, and compactness for small and large field size class..... 40

Figure 1.8: Maximum overall segmentation quality index (OSI) and geometric, topological and numerical congruence indices as a function of scale. The maximum value all of the geometric, spatial and numerical congruence indices as a function of the scale for (a) small objects and (c) large objects. Maximum overall segmentation quality index (OSI) for (b) small objects and (d) large objects. Geometric indices are represented by solid grey circles and open circles which denote the normalized area difference index (nAdi) and normalized perimeter difference index (nPdi) respectively. Solid grey and open squares represent the topological indices of under (Useg)

and over-segmentation index (OSeg) respectively. Arithmetic congruence indices are symbolized by solid grey and open triangles for the many objects penalization index (mOi) and undetected object index (Udi) respectively. The solid black line and vertical rectangles represent the combination of all the segmentation accuracy indices in the overall segmentation quality index (OSI). Each data point represents the average for each index (n=81). Error bars ± 1 SE. 41

Figure 1.9: Effect of scale parameter on mean segment size. Mean segment size as scale parameter increases for (a) small size objects and (b) large size objects..... 43

Figure 1.10: Illustration of the variation in topological and arithmetic indices as a function of scale. A subset of segmentation at various scales, 8, 28 and 100, to illustrate how segmentation indices change with increasing scale values for (a) small objects and (b) large objects. Comparison between the reference object (red) and the image object (blue) of geometric and topological characteristics. Image object segments (yellow) which correspond to the reference object. 44

Figure 1.11: Illustration of the variation geometric, topological and arithmetic indices as a function of shape. Overlapping image object and reference layer, which illustrates how segmentation quality changes with increasing shape values 0.1, 0.5, 0.9. A subset of the segmentation for (a) small objects at fixed scale 8 and (b) large objects at fixed scale 40. Image objects (blue) and image sub-objects (yellow) compared to the reference layer (red). 46

Figure 2. 1:Schematic of cookstove setup and gaseous sampling system 61

Figure 2.2: Gas pollutant emissions concentration of CO, NO and CO₂ for wood pellets pyrolyzed in an indirect pyrolysis cookstove. Green horizontal lines represent the varying phases of pyrolysis happening during the cooking test. Phase (I) is pre and early pyrolysis, Phase (II) main pyrolysis and Phase (III) is post-pyrolysis. The lines also indicate the time at which a new pot of cooking water was placed over the cookstove..... 66

Figure 2.3: Short-term average for gaseous emission rates and heat input to water. The quantity of each gaseous emissions as a function of time for (a) CO₂, (b) NO and (c) CO and (d) the heat input to cooking water (Q_w). Each point (n=485) represents a short-term average determined from data from eleven water boiling tests. Grey circles and black circles in (b) represent low N content woody biomass and high-N-content of herbaceous biomass (corn and switchgrass)..... 67

Figure 3. 1: Nitrogen contents of uncharred OM and PyOM as a function of pyrolysis temperature. Nitrogen contents as a function of temperature for uncharred OM and PyOM of (a) maize leaves, (b) ryegrass, (c) willow leaves, (d) willow wood and (e) maize stalks at three different pyrolysis temperatures. Grey circles and black circles represent high- and low-N content OM and PyOM, respectively. 92

Figure 3.2: Nitrogen K-edge NEXAFS spectra of uncharred initial OM, entire PyOM (py-), extracted PyOM (e-), and the toluene extract of PyOM (tol-) as a function of pyrolysis temperature for maize leaves. (a) Low N-containing maize leaves, and (b) high N-containing maize leaves. Black lines represent the peak centers associated with selected key spectral features: 398.78 eV for C=N bonds in aromatic six-membered rings, 401.3 eV for C-N bonds in aromatic five-

membered rings, and 405.76 eV for N-H bonds. Spectra of additional OM shown in Appendix Figs. B.3-6..... 95

Figure 3.3: Proportion of aromatic nitrogen functional groups for PyOM at different pyrolysis temperatures and all types of biomass. (a) Aromatic C=N in 6-membered rings putative represents the proportion of the total spectral absorption intensity corresponding to spectral features at 398.1 eV, (b) aromatic C=N in 5 and 6-membered rings containing 1 and 2N atoms, represents the proportion of the total absorption intensity of the sum of spectral features at 398.73 and 399.93 eV, (c) aromatic C=N in 6-membered oxygenated rings with represent the proportion of the total absorption intensity spectral feature at 399.4 eV (d) aromatic C-N in 6-membered oxygenated rings with represent the proportion of the total absorption intensity spectral feature at 400.74 eV, (e) aromatic C-N in 5-membered rings with delocalized pairs of electrons from aromatic N from 5-membered rings (containing one or two N atoms), represent the proportion of the total absorption intensity of the sum of spectral features at 401.3 and 402.13 eV, and (f) exocyclic N bonded to aromatic 6 membered rings represent the proportion of the total absorption intensity of the sum of spectral features at 403 and 403.61 eV and (g) quaternary N represent the proportion of the total absorption intensity spectral feature at 400.9 eV 98

Figure 3.4: Effects of nitrogen contents on the formation of N functional groups. (a) Sum of all aromatic N heterocycles as a function of N contents in PyOM, (b) proportion of quaternary N in PyOM as a function of N contents, and (c) sum of all N exocyclic N attached to a 6-membered aromatic ring as a function of N contents in PyOM expressed as a proportion of the total absorption intensity (left y-axis). Plots are fitted with significant regression lines: Total aromatic N = $58.1 + 4.78x$, $R^2 = 0.44$, $p < 0.0001$; Quaternary N = $7.2 - 1.36x$, $R^2 = 0.29$, $p = 0.0002$; Exocyclic N bonded to 6-membered aromatic rings = $25.1 - 2.29x$, $R^2 = 0.43$, $p < 0.0001$ 100

Figure 3.5: Cumulative C mineralized as a proportion of added C. (a) Cumulative C mineralization over time for maize leaves dried at 60°C and PyOM pyrolyzed at 350°C and 700°C, and (b) cumulative C mineralization for PyOM pyrolyzed at 350°C and 700°C. Black circles, diamonds and squares represent high N-containing maize leaves while grey circles, diamonds and squares represent low N-containing maize leaves. 102

Figure 3.6: Relationship between the carbon-to-nitrogen ratio and the mineralization of OM or PyOM-C. White circles, grey squares and black squares represent OM, PyOM at 350°C and 700°C, respectively. Lines indicate linear regression: OM: = $1.53 - 0.004x$, $p = 0.05$, $R^2 = 0.40$; PyOM-C at 350° C: $y = 0.15 - 0.0008x$, $p = 0.27$, $R^2 = 0.15$; PyOM-C at 700° C: $y = 0.03 - 0.0002x$, $p = 0.21$, $R^2 = 0.22$ 103

Figure 3.7: Relationship between cumulative PyOM-C mineralized and ratios of N functional groups from the PyOM toluene extract as observed by N K-edge NEXAFS. (a) Actual vs. multiple regression model predicted response values for cumulative PyOM-C mineralized, (b) relationship between cumulative PyOM-C mineralized and aromatic C=N in 6-membered rings, and (c) aromatic C=N in oxygenated 6-membered rings. 104

Figure A. 1: Main components of the pyrolysis cookstove	122
Figure A. 2: Secondary air inlets are bent in to induce swirl.....	122
Figure A. 3: Mass histories	123
Figure A. 4: Instantaneous measurements of selected independent operating parameters.....	126
Figure A. 5: Pyrolysis and water temperatures for wood pellet	127
Figure B. 1: N K-edge TEY NEXAFS spectra of N standard compounds. (a) Mineral N and amino acid compounds. (b) Six-membered ring heterocycles with one or two N substitutions.	132
Figure B. 2: N K-edge TEY NEXAFS spectra of N standard compounds. (a) Nitro functional groups. (b) Five-membered ring heterocycles with one or two N substitutions. (c) Heterocycles with one or two keto groups attached. (d) Structure bearing five and six membered heterocyclic rings and quaternary N.....	133
Figure B. 3: Nitrogen contents as a function of temperature for uncharred OM and PyOM for all types of studied biomass. Means and standard deviation (n=14 except for uncharred OM n=15). Different capital letters indicate significant differences (p<0.05) between treatments.	134
Figure B. 4: Nitrogen K-edge NEXAFS spectra of uncharred initial OM, entire PyOM (py-), extracted PyOM (e-), and the toluene extract of PyOM (tol-) as a function of pyrolysis temperature for willow leaves. (a) High N-containing willow leaves, and (b) low N-containing willow leaves. Black lines represent the peak centers associated with selected key spectral features: 398.78 eV for C=N bonds in aromatic 6-membered rings, 401.3 eV for C-N bonds in aromatic 5-membered rings, and 405.76 eV N-H bonds.	135
Figure B. 5: Nitrogen K-edge NEXAFS spectra of uncharred initial OM, entire PyOM (py-), extracted PyOM (e-), and the toluene extract of PyOM (tol-) as a function of pyrolysis temperature for maize stalks residues. (a) Low N-containing maize stalks residues, and (b) high N-containing maize stalks residues. Black lines represent the peak centers associated with selected key spectral features: 398.78 eV for C=N bonds in aromatic 6-membered rings, 401.3 eV for C-N bonds in aromatic 5-membered rings, and 405.76 eV N-H bonds.	136
Figure B. 6: Nitrogen K-edge NEXAFS spectra of uncharred initial OM, entire PyOM (py-), extracted PyOM (e-), and the toluene extract of PyOM (tol-) as a function of pyrolysis temperature for willow wood residues. (a) Low N-containing willow wood residues, and (b) high N-containing willow wood residues. Black lines represent the peak centers associated with selected key spectral features: 398.78 eV for C=N bonds in aromatic 6-membered rings, 401.3 eV for C-N bonds in aromatic 5-membered rings, and 405.76 eV N-H bonds.	137
Figure B. 7: Nitrogen K-edge NEXAFS spectra of uncharred initial OM, entire PyOM (py-), extracted PyOM (e-), and the toluene extract of PyOM (tol-) as a function of pyrolysis temperature for ryegrass residues. (a) Low N-containing ryegrass residues, and (b) high N-containing ryegrass residues. Black lines represent the peak centers associated with selected key spectral features:	

398.78 eV for C=N bonds in aromatic 6-membered rings, 401.3 eV for C-N bonds in aromatic 5-membered rings, and 405.76 eV N-H bonds..... 138

Figure B. 8: Cumulative C mineralized on the basis of per unit C added rye grass residues. (a) Cumulative C mineralization for rye grass residues dried at 60°C and PyOM pyrolyzed at 350°C and 700°C at low and high N contents, and (b) cumulative C mineralization for PyOM at 350°C and 700°C only. Black circles, diamonds and squares represent low N-containing rye grass residues, while grey circles, diamonds and squares represent high N-containing rye grass residues. 139

Figure B. 9: Cumulative C mineralized on the basis of per unit C added willow leaves. (a) Cumulative C mineralization over time for willow leaves dried at 60°C and PyOM pyrolyzed at 350°C and 700°C, and (b) cumulative C mineralization for PyOM at 350°C and 700°C. Black circles, diamonds and squares represent low N-content willow leaves, while grey circles, diamonds and squares represent high N-containing willow leaves..... 140

Figure B. 10: Cumulative C mineralized on the basis of per unit C added willow wood residues. (a) Cumulative C mineralization over time for willow wood residues dried at 60°C and PyOM pyrolyzed at 350°C and 700°C, and (b) cumulative C mineralization for PyOM at 350°C and 700°C. Black circles, diamonds and squares represent low N-containing willow wood residues, while grey circles, diamonds and squares represent high N-containing willow wood residues. 141

Figure B. 11: Cumulative C mineralized on the basis of per unit C added maize stover. (a) Cumulative C mineralization over time for maize stover dried at 60°C and PyOM pyrolyzed at 350°C and 700°C, and (b) cumulative C mineralization for PyOM at 350°C and 700°C. Black circles, diamonds and squares represent low N-containing maize stalks, while grey circles, diamonds and squares represent high N-containing maize stalks..... 142

Figure B. 12: Extracted mineral N in the form of NH_4^+ and NO_3^- . (a) Nitrogen mineralization for OM with low and high N content, (b) nitrogen mineralization over time for PyOM produced at 350°C with low and high N content, and (c) nitrogen mineralization over time for PyOM produced at 700°C with low and high N content. Black vertical bars represent extractable mineral N (NH_4^+ and NO_3^-) before the incubation started, while grey vertical bars represent total extractable mineral N at day 50 of the incubation. The bars are an average of duplicates for day 0 and 4 replicates at day 50 (ML: maize leaves, MS: maize stover, RG: Ryegrass, WL: willow leaves, WW: willow wood). 143

Figure B. 13: Relationship between cumulative PyOM-C mineralized and ratios of N functional groups from PyOM identified by N K-edge XANES. (a) Actual vs. predicted response values using a multiple regression model for cumulative PyOM-C mineralized, (b) relationship between cumulative PyOM-C mineralized and aromatic C=N in 6-membered rings (putative) from PyOM after extraction, and (c) relationship between cumulative PyOM-C mineralized and aromatic C=N in 6-membered rings (secondary peak)..... 144

Figure B. 14: Relationship between cumulative PyOM-C mineralized and ratios of N functional groups from PyOM after extraction identified by N K-edge XANES. (a) Actual vs. predicted response values using a multiple regression model for cumulative PyOM-C mineralized, and (b)

relationship between cumulative PyOM-C mineralized and aromatic C=N in 6-membered rings
(putative) from PyOM after extraction. 145

LIST OF TABLES

Table 1.1: Total area for each class in the study region (n=2397).....	26
Table 1.2: Reference object basic statistics per object size and class.....	28
Table 1.3: Optimum segmentation parameter combination for scale, shape, and compactness identified by the OSI for, global scene, per size class and land cover class and hierarchical segmentation.	49
Table 2.1: Quantities measured directly, at 1-second intervals during the burn cycle	63
Table 2.2: Independent variables (representing stove operating conditions) and dependent variables (representing key stove outputs) in the stepwise regression models.....	63
Table 2.3: Stepwise regression input variables, resulting predictor variables and coefficient of determination. The predictor variables are listed in decreasing order of importance.....	69
Table 2.4: Stepwise regression coefficients and collinearity statistics of regression models.....	71
Table A.1:Moisture content of pyrolysis and combustion biomass fuels at the time of individual stove tests. See Deng et al., (2018) for moisture data from additional tests.....	118
Table A.2: Elemental composition and higher and lower heating values (HHV, LHV) of triplicate samples of biomass fuel, biochar and wood charcoal (n=3) Each row of biochar properties represents a separate stove test. Each row of wood properties represents a different batch of wood, used in several stove tests. Fuel, wood charcoal and biochar properties for additional stove tests appear in Deng et al., (2018).....	119
Table B.1:Elemental composition for OM and PyOM of all feedstocks.....	146
Table B.2: pH and inorganic NH ₄ -N and NO ₃ -N concentrations for OM and PyOM of all feedstocks.....	147
Table B.3: Major features of TEY N K-edge NEXAFS spectra collected from N standard compounds. Peak centers and half widths at half maximum (hwhm) are shown in eV.	148
Table B.4: N K-edge NEXAFS TEY peak assignments used in deconvolution model.	149
Table B.5: Proportion of absorption area (%) of N bonds measured with N K-edge NEXAFS for maize leaf OM and PyOM components.....	150
Table B.6: Proportion of absorption regions (%) of N bonds measured with N K-edge NEXAFS for maize stover OM and PyOM components.	151
Table B.7: Proportion of absorption regions (%) of N bonds measured with N K-edge NEXAFS for ryegrass OM and PyOM components.	152

Table B.8: Proportion of absorption regions (%) of N bonds measured with N K-edge NEXAFS for willow wood OM and PyOM components..... 153

Table B.9: Proportion of absorption regions (%) of N bonds measured with N K-edge NEXAFS for willow leaf OM and PyOM components..... 154

CHAPTER 1: OPTIMAL SEGMENTATION PARAMETERS FOR OBJECT-BASED IMAGE ANALYSIS: APPLICATION TO COMPLEX AGRICULTURAL LANDSCAPES

Abstract

Image segmentation quality is critical to the final accuracy of map classification, yet its evaluation is often done by visual inspection, which is subjective and can introduce considerable error to the classification process. In this study, we present an innovative protocol to assess multiresolution segmentation (MRS) quality using a supervised evaluation method. We tested the performance of this method in a complex agricultural environment using high spatial and spectral resolution satellite images. Geometric, topological and arithmetic congruence indices were combined into a global “overall segmentation quality index” (OSI), and the impact of the segmentation parameters (i.e., scale, shape, and compactness) on each index was quantified. Optimum segmentation parameters were selected according to the maximum value reached by OSI. The scale and shape segmentation parameters affected geometric, topological and arithmetic measures significantly ($p < 0.0001$). The scale parameter generated inter-scale variation for all indices of 58% and 23% for small and large objects respectively, except many object index (mOi). The mOi experienced the greatest change by an average of 102% by scale value 30. The undetected objects index decreased by 92, and 48% for small (47 m^2) and large (1157 m^2) objects across scales. The shape caused approximately 50% less variation for the indices when compared to the variation caused by scale. The shape parameter had different effects on arithmetic measures across scales. At small scales, object over-partitioning decreased by 190% with an increase in shape from 0.1 to 0.9. At coarse scales, as shape increased from 0.1 to 0.9,

the undetected object index decreases by as much as 56%. Within a scale, geometric and topological measures were positively affected by smaller shape values but had different effects on arithmetic measures. Higher shape values improved all measures at coarser scales. OSI for our study was 0.83, using a single set of parameters to partition and extract all features in the image. There were tradeoffs associated with using a single set of parameters, considering that high under-segmentation and missing objects could introduce considerable error in subsequent classification steps.

Keywords: Multiresolution segmentation, Reference objects, Shape, Segmentation quality, Intra-scale variation, Inter-scale variation

1. Introduction

Geographic Object-Based Image Analysis (GEOBIA) is a novel framework which can prove to be advantageous (Blaschke, 2010) for the analysis of complex agricultural high-resolution images compared to conventional pixel-based procedures. GEOBIA requires a two-step process which includes image segmentation and classification. The segmentation process partitions an image into homogenous, non-overlapping and meaningful objects (Hay and Castilla, 2008; Blaschke et al., 2014; Witharana and Civco, 2014; Ma et al., 2015). The classification process assigns a class (e.g., land cover or land use type) to each segmented object based on its spectral, geometric, spatial, texture and contextual information (Baatz and Schäpe, 2000; Blaschke et al., 2014; Witharana and Civco, 2014). The resulting map accuracy relies on both the segmentation quality and classification accuracy. However, most research has focused on classification accuracy which fails to account for the morphology of geographic objects (Persello and Bruzzone, 2010), even though segmentation quality is an integral step in improving final map accuracy (Baatz and Schäpe, 2000; Baatz et al., 2008; Liu et al., 2012).

Image segmentation is executed by algorithms that rely on a set of parameters that create image objects, which can be related to a geographical element (Hay and Castilla, 2008). Among the different segmentation methods available (Haralick and Shapiro, 1985; Pal and Pal, 1993), region growing algorithms partition an image by merging adjacent image objects which share homogenous spatial and spectral features (Espindola et al., 2006; Gao et al., 2011); this is the foundation of the multiresolution segmentation algorithm (MSR) (Baatz and Schäpe, 2000). Scale (SC), shape (SH), and compactness (CP) are the parameters that control the creation of image objects and determine the final features attributed to the segments. To date, the selection of parameters that produce high-quality segmentation through rigorous empirical evaluation has

proven to be complicated given the multitude of parameter combinations possible (Witharana and Civco, 2014). Many studies have opted (Anders et al., 2011; Johnson et al., 2015; Ma et al., 2015; O’Connell et al., 2015) to consider only the effect of the SC parameter on segmentation quality, citing that SC is the most important parameter controlling the heterogeneity threshold for the creation of an object (Drăguț et al., 2014). As SC increases, the heterogeneity threshold increases, which controls the average size of the object. While the SC parameter determines the size of an object, SH and CP change the heterogeneity criteria by weighing shape or texture homogeneity, respectively (Baatz and Schäpe, 2000). Very little has been studied (Liu et al., 2012; Zhang et al., 2015) on the effects of SH and CP on segmentation quality. We suggest that while SC delineates the size of a segment across scales, SH and CP can lead to significant variations in the segment features affecting overall segmentation quality and, ultimately, classification accuracy.

Segmentation quality assessment and the selection of “best” segmentation parameters have relied heavily on visual inspection and “trial and error” methods, which is subjective, unreliable and non-transferable (Persello and Bruzzone, 2010; Arvor et al., 2013; Ye et al., 2018). Recently, various authors (Zhan et al., 2005; Möller et al., 2007; Clinton et al., 2010; Liu et al., 2012; Witharana and Civco, 2014; Zhang et al., 2015) have attempted to normalize the process of image segmentation quality assessment using the empirical discrepancy method, also known as the supervised evaluation method (Zhang, 1996). The empirical discrepancy method requires the use of reference image objects delineated by the user. Measures are used to evaluate congruence of multiple features between a segmented object and a reference object. Numerous measures have been developed based on geometric, spatial and arithmetic features of objects (Zhang, 1996; Wang et al., 2004; Zhan et al., 2005; Schöpfer et al., 2008; Clinton et al., 2010;

Anders et al., 2011; Liu et al., 2012; Lizarazo, 2014; Zhang et al., 2015). It is simple to evaluate each measure individually, yet, assessing the best sets of parameters using multiple individual indices is difficult. Some studies have overcome this problem by ranking the measures (Clinton et al., 2010). However, this causes plurality, meaning multiple set of parameters can be used to partition the image. An alternative way of addressing this problem is to evaluate multiple measures concurrently and to develop a combination of measures which evaluates segmentation quality. A single overall segmentation quality index evaluates the effect of all measures together by finding the set of parameters that returns the segmentation that shares the highest congruence to the reference data. The advantage of this method is that a single set of parameters can be used to segment and extract all features in an image at once, which increases the efficiency of analysis but generates some significant tradeoffs. For example, achieving high overall segmentation quality could mean low congruence of one or more individual measures. Various studies (Clinton et al., 2010; Liu et al., 2012) have proposed a variety of individual measures and their combination, however, it is not clear how each of the segmentation parameters affects each measure individually and how each measure affects the final overall segmentation quality.

This study focuses on how segmentation quality is affected by segmentation parameters, specifically regarding geometrical, topological and arithmetic measures. We hypothesize that all the parameters contribute to the variation of these measures and that topological measures have the greatest effect on overall segmentation quality. We also propose an overall segmentation quality index (OSI) which combines both local and global measures to assess segmentation. Our objectives were to: (1) assess how the MRS algorithm parameters (SC, SH, and CP) affect the individual indices to evaluate segmentation quality; (2) define a global segmentation index that

can select the best segmentation parameters; (3) validate the segmentation process by comparing segmentation results to reference data.

2. Description of study area and data

We tested the segmentation protocol in an agroforestry site of approximately 100 km², (Figure 1.1) located in the Yala River Basin in Western Kenya. The site is located within the Vihiga and Kakamega districts at latitude 0° 7' 51.57'' N and longitude 34° 49' 13.01'' E (Kuyah et al., 2012). The site is characterized by moderate to steep sloping terrain with an elevation between 1430 and 1720 masl. Land cover is mainly crops, woodland and farming households. The study area represents both managed agricultural and unmanaged natural areas, which result in a complex image that contains objects with contrasting sizes and shapes.

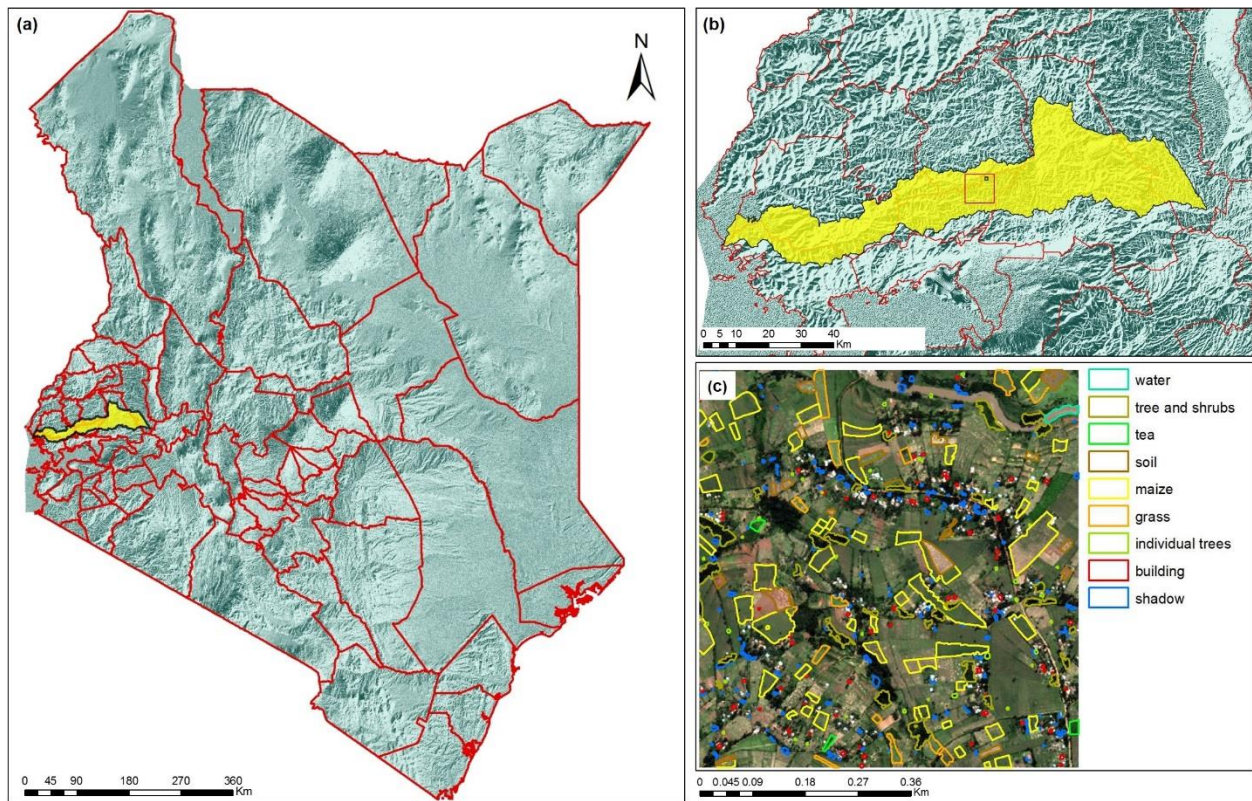


Figure 1. 1: Map of the study area and reference object data set. (a) The study area is located in western Kenya, within the Yala watershed (highlighted in yellow); (b) the mid-Yala block is located between the Kakamega and Vihiga districts and spans an area of 100km² and has a mixture of agricultural and forested land; (c) high resolution image (WV-2) 1km² grid and delineated reference polygons for different classes.

High spatial resolution digital imagery was acquired in July 2010 by the WV-2 satellite. The WV-2 dataset included a single panchromatic (PAN) image and multi-spectral (MS) 4-band image with a spatial resolution of 0.5 m and 2.0 m respectively. The MS image was pan-sharpened to obtain a high spectral and spatial resolution image.

3. Methodology

The image segmentation protocol consists of three main steps (Figure 1.2). First, we manually partitioned a high-resolution digital image to create the reference data. The image was also partitioned using a computer-assisted segmentation algorithm (Figure 1.3a-c). We then determined local (per each reference object), global measures (per sum of all reference objects) for each partition and calculated congruence indices between algorithm-generated (segmented) data and reference data. Finally, individual indices were combined into a final overall segmentation quality index. The next sections provide additional details on the processing steps.

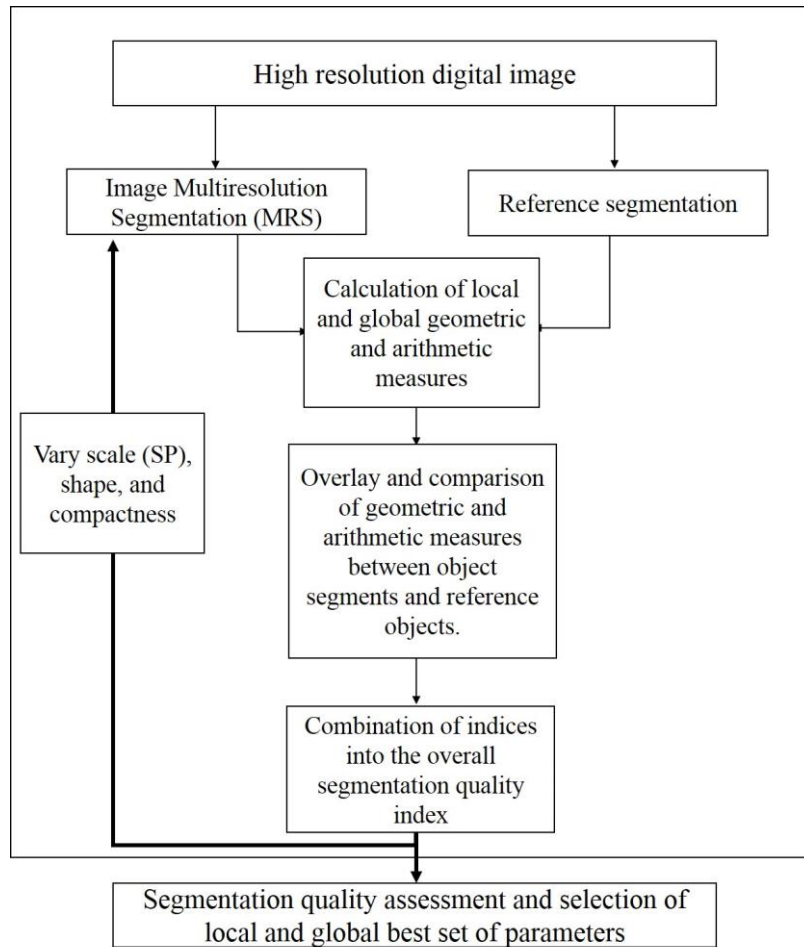


Figure 1.2: Workflow diagram for segmentation quality analysis. Methods and processing steps used for the analysis of image segmentation quality.

3.1. Data preparation and selection of reference data

The initial step in the process of supervised segmentation is to create a reference layer used to evaluate segmentation quality. We created the reference layer in ArcGIS 10.3.1 software (ESRI Inc., Redlands, CA, USA), by manually vectorizing all classes in the image. We used a normalized difference vegetation index (NDVI) layer and soil-adjusted vegetation index (SAVI) to assist in the process of delineating multiple classes. We confirmed the class of each delineated polygon via field visits. We used the sampling design tool 10.0 (NOAA Biogeography Branch, Silver Spring, MD) in ArcGIS 10.3.1 to perform a stratified random sampling (Stehman et al.,

2012; Ma et al., 2015) and create the final reference layer. The classes of interest included in the study were, buildings, grass, maize, shadow, soil, tea, individual trees, trees/shrubs and water (Table 1.1). A total of 387 reference objects (Figure 1.1c) were selected among the different classes (Table 1.2), representing 20% of the total area of the image area. Reference samples for each of the classes were selected proportionally to the area of the class. We further divided the classes into small and large objects according to their average size. Small objects included, buildings, shadows and individual trees, and large object included grass, maize, soil, tea, trees/shrubs, and water.

Table 1.1: Total area for each class in the study region (n=2397)

Class	Count	Class Area (m ²)			
		Min	Max	Average	st dev
building	355	5.22	300.99	43.87	28.02
grass	181	8.36	2757.62	402.81	527.24
maize	320	18.53	15516.37	1258.29	1390.85
shadow	764	2.11	870.44	55.11	81.53
soil	187	10.08	2683.93	316.58	450.69
tea	12	169.04	4637.24	874.58	1214.09
individual trees	203	2.32	55.22	27.18	14.36
trees/shrubs	371	55.39	6135.14	427.04	690.53
water	4	597.45	5122.73	2968.14	2045.72

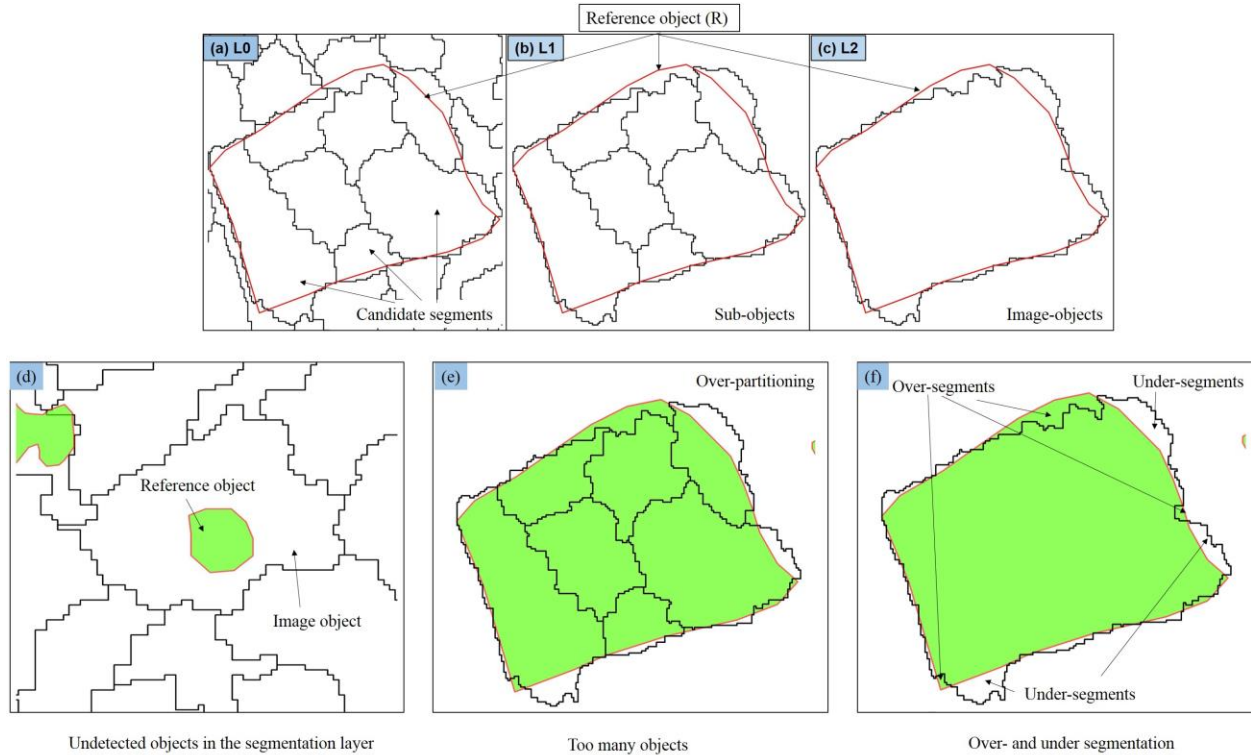


Figure 1.3: Schematic of image segmentation and the creation of image object segments. Segmentation process consists of multiple levels to create image objects. (a) Level 0, segmentation parameters are applied for the partitioning image and subsequent merging of similar regions based on the homogeneity between pixels; segments created at this level are candidate segments; (b) Level 1, image object criteria is applied to determine which segments correspond to the reference object; a candidate segment become a corresponding image object when 50% of its area is within the boundaries of the reference object; these are sub-objects with respect to the upper level of segmentation; (c) Level 2, the final object image object is created by merging all corresponding image object segments that compose the reference object. Topological and arithmetic measures are illustrated; (d) an object is undetected or missing when the image object and reference object do not correspond to the same class; (e) too many objects is caused by the over-partitioning of one reference object into numerous small image objects; (f) over- and under-segmentation happen when the image object either overextends beyond the boundaries of the reference object or the image object does not intersect the reference object in its entirety.

Table 1.2: Reference object basic statistics per object size and class

Object classification		Object Area (m ²)			
Class	Sample size	Min	Max	Average	st dev
Small objects	264	3.53	397.44	47.00	44.95
building	72	13.78	97.00	43.72	19.10
shadow	150	3.53	397.44	52.01	56.02
individual trees	42	11.78	157.83	34.76	26.65
Large objects	123	141.55	8877.01	1157.60	1242.33
grass	15	286.02	2771.42	986.34	693.34
maize	54	189.46	8877.01	1481.79	1592.45
soil	19	220.90	2735.46	846.85	745.17
tea	3	444.38	752.10	616.67	157.14
trees/shrubs	31	141.55	4625.12	899.30	955.80
water	1	1754.28	1754.28	1754.28	0.00

3.2. Image segmentation

We applied the multiresolution segmentation algorithm (MRS), in eCognition 9.0 software (Trimble Geospatial, Munich, Germany) to partition the image. The algorithm is a bottom-up technique that creates image objects by merging neighboring regions with spatial and spectral homogeneity based on image layer weight, SC, SH and CP (Baatz and Schäpe, 2000). The SC defines the highest limit for spectral and spatial heterogeneity to create an image object (Ma et al., 2015). Two pairs of measures, color and shape; and compactness and smoothness define homogeneity. Each measure within a pair is weighted to determine its significance to the homogeneity criteria. The SH determines whether an image object will be created based on spatial or spectral homogeneity. When the SH measure is low, the color (image layer values) of the image object will have more spectral homogeneity. If the SH measure is high, the image object will have higher spatial homogeneity. The SH defines the compactness and smoothness which determine the textural homogeneity of an image object.

Multiple sets of image objects were generated based on different combinations of SC, SH and CP parameters. We evaluated the scale parameter between 2-30 and 35-100 at increment intervals of 2 and 5, respectively. The shape and compactness were evaluated from 0.1-0.9 with increments of 0.1. The different combination of segmentation parameters resulted in 2349 unique sets of image objects.

3.3. Measures and indices for segmentation quality assessment

Individual measures were determined based on the geometry, topology and the number of matching image objects rather than spectral information (de Bruin et al., 1999; Zhan et al., 2005; Möller et al., 2007; Clinton et al., 2010). Congruence indices were used to quantify the degree of agreement between the reference objects and the segmented objects for each measure. We redefined some of the measures to enable a mathematical comparison.

3.3.1. Geometric congruence indices

Multiple geometric measures (Lucieer and Stein, 2002; Clinton et al., 2010) were defined based on the area and perimeter of the objects. Each of the measures was normalized to standardize the value range, resulting in a corresponding index. The first measure is the area congruence between the image objects and the reference object; this measure is similar to Area Fit Index (AFI), defined by (Lucieer and Stein, 2002). We define the normalized area difference index (nAdi) as:

$$nAdi = 1 - \left| \frac{(A_o - A_r)}{A_r} \right| \quad (1)$$

where A_o is the area of the image object and denotes the sum of the area of all the image objects that overlap the reference object by more than 50% and A_r , is the area of the reference object. The index is continuous between [0, 1]; if nAdi is 1, then the area of the image object is the same when compared to the reference object. Similarly, the normalized perimeter difference index

(nPdi), measures the congruence in the perimeter between the image object and the reference object and is defined as follows:

$$nPdi = 1 - \left| \frac{(P_o - P_r)}{(P_r)} \right| \quad (2)$$

where P_o , is the perimeter of the image object and P_r , is the perimeter of the corresponding reference object. The nPdi also has a range of [0, 1], 1 denoting perfect congruence of the perimeter between the image object and the reference object.

3.3.3. Topological congruence indices

We measured topological characteristics related to containment (de Bruin et al., 1999; Möller et al., 2007) to establish the degree of over- (Oseg) and under-segmentation (USeg) between objects (Lucieer and Stein, 2002; Möller et al., 2007). OSeg occurs when the overlap area between the objects is smaller than the area of the reference object (Figure 1.3f). The portion of the reference object which remains without being segmented is the over-segment. USeg occurs when the image object area is larger than the overlap area. The portion of the image object that overextends the reference object is known as the under-segment.

We define the over-segmentation index (OSeg) as:

$$OSeg = 1 - \left| \frac{(A_r \setminus A_o)}{(A_r)} \right| \quad (3)$$

where $A_r \setminus A_o$ is the area of the over-segment, i.e., the area of the reference object which is not part of image object segment, and A_r is the area of the reference object.

The under-segmentation index (USeg) is:

$$USeg = 1 - \left| \frac{(A_o \setminus A_r)}{(A_o)} \right| \quad (4)$$

where $A_o \setminus A_r$ symbolizes the under-segment, i.e., the area of the image object segment which is not part of the area of the reference object, and A_o is the area of the object segment. Both

indices are continuous between [0,1]; a value of 1 denotes perfect intersection between the image object and the reference object for both indices.

3.3.2. Arithmetic congruence indices

Two arithmetic measures were evaluated to determine the number of matching image object segments to the corresponding reference object. We defined the two measurements as the many objects index (mOi) and undetected object index (Udi):

$$mOi = \frac{\# \text{Classified objects}}{\# \text{sub-objects}} \quad (5)$$

$$Udi = \frac{\# \text{Classified objects}}{\# \text{Reference objects}} \quad (6)$$

Where #Classified objects represent the number of image object segments detected for a given class, #sub-objects is the number of image object segments created for a given set of parameters corresponding to a reference object, and #Reference objects is the number of objects of interest. A value of 1 for the mOi and Udi means a one to one congruence between objects. If mOi is less than 1, many small image objects segments were created per corresponding reference object (Figure 1.3e). An Udi value of less than 1, indicates that for a given class, there will be one or more missing reference objects in the segmentation layer (Figure 1.3d).

3.3.3. Overall segmentation quality index

To evaluate segmentation quality and determine the best set of parameters, we propose the overall segmentation quality index (OSI). The OSI is a global index [0,1] based on the average of geometric, topological and arithmetic indices previously described and it is mathematically defined as:

$$OSI = \frac{\left(\frac{nAdi+nPdi}{2}\right) + \left(\frac{OSeg+USEg}{2}\right) + mOi + Udi}{4} \quad (7)$$

An OSI of 1 denotes perfect congruence between the image objects and the reference object.

3.4. Statistical analysis

All statistical analyses were performed using JMP version 12.0.1 (SAS Institute, 2015). We used nested standard least squares ($p \leq 0.05$) to determine the effect of segmentation parameters on the different indices.

We used the nonparametric Wilcoxon test to compare SC and SH statistical differences among indices. If the test was significant ($p < 0.001$), we employed the Dunn's test to compare each SC and SH combination to a control. We used the lowest SC and SH and CP, which was 2, 0.1 and 0.1, respectively.

4. Experimental results

4.1. Relationship of segmentation quality indices to scale and shape

For the geometric, topological, arithmetic and overall segmentation quality indices, there was a significant difference with scale and shape ($p < 0.0001$); compactness had no significant effect on any of the indices.

4.1.2. Variation in the geometric congruence indices

For both small and large objects (Table 1.2) the nAdi decreased significantly (Figure 1.4a) with an increase in scale ($p < 0.0001$). As the scale increased from 2 to 100, the average nAdi decreased by 79% and 23% for small and large objects, respectively. nAdi decreased significantly ($p < 0.001$) beyond scale values of 18 (small objects) and 40 (large objects) when compared to the nAdi for scale value 2. The SH caused the nAdi to change across scales and within scales (Figure 1.4a). At SC 2-14, nAdi was approximately 0.98, for SH 0.1-0.9. As the SC increased from 14-26, shape 0.7, had the highest average nAdi of 0.96. At SC above 26, lower

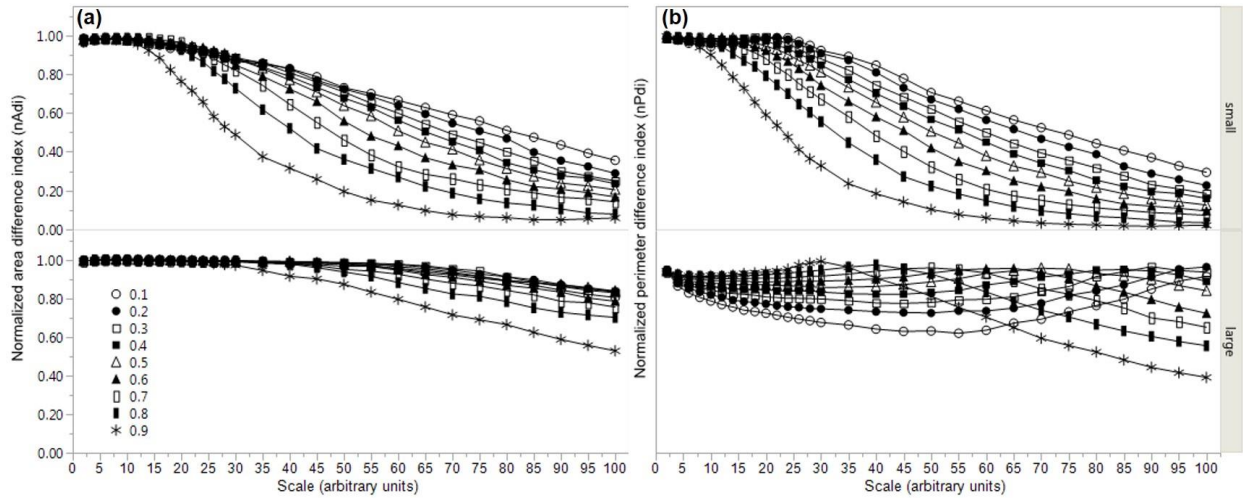


Figure 1.4: Geometric congruence indices. (a) Normalized area difference index and (b) Normalized perimeter difference index as a function of scale, shape for small and large field size class.

SH values (0.1-0.5) resulted in highest nAdi. With increasing SH from 0.1 to 0.9, the average nAdi changed by 34% and 9% for small and large objects, respectively, with increasing SH.

For small sized objects (Figure 1.4b), the mean nPdi decreased 86% with increasing SC values. At SC 2-14, SH value of 0.6 resulted in a mean nPdi of 0.99. For SC values between 14 and 26, a lower SH value of 0.3 resulted in a nPdi of 0.98. At SC above 26, the nPdi was highest at SH of 0.1.

For large-sized objects, nPdi decreases by 19% when the scale increase from 2 to 100. On average, SH values of 0.1 and 0.9 caused the lowest nPdi, while shape value 0.5, caused the highest nPdi (0.89). Between scales values from 2 to 26, an increase in SH from 0.1-0.9 caused an increase in the nPdi of 29%. nPdi was highest for SH 0.9, in this scale range. Above the scale value of 50, the SH effect reversed. Lower SH values (0.3-0.5) resulted in higher nPdi. The nPdi changed by 45% to 7% for small and large objects, respectively.

4.1.3. Variation in the topological congruence indices

For small size objects, an increase in the SC from 2 to 20 caused a 13% decrease in the OSeg (Figure 1.5a). Oseg increased by 17% above scale 20. However, for large objects, an increase in the SC from 2-60 caused a 12% decrease in the OSeg. Above scale value 60, the OSeg increased by 3%. For small objects, at lower SC values (2-14), as the shape increased from 0.1 to 0.9; over-segmentation also increased by 6%. From SC values 14-100, as SH values increased the over-segmentation decreased. For larger objects, from scale 2-26, lower SH values resulted in lower over-segmentation. Beyond an SP value of 26, the effect of SH shifts, SH values of 0.3-0.6- result in the highest OSeg index. The SH caused the average Oseg to increase by 5% for small objects and decrease 4% for large objects.

The USeg decreased with SC and SH for both small- and large-size objects (Figure 1.5b). Across SC, the USeg decreased by 30% and 17% for small- and large-size objects, respectively. SH value of 0.1 caused the highest USeg index between the scales of 2 to 100 for small and large objects. The SH caused the USeg to change by 11% for small objects and 8% for large objects, across scales.

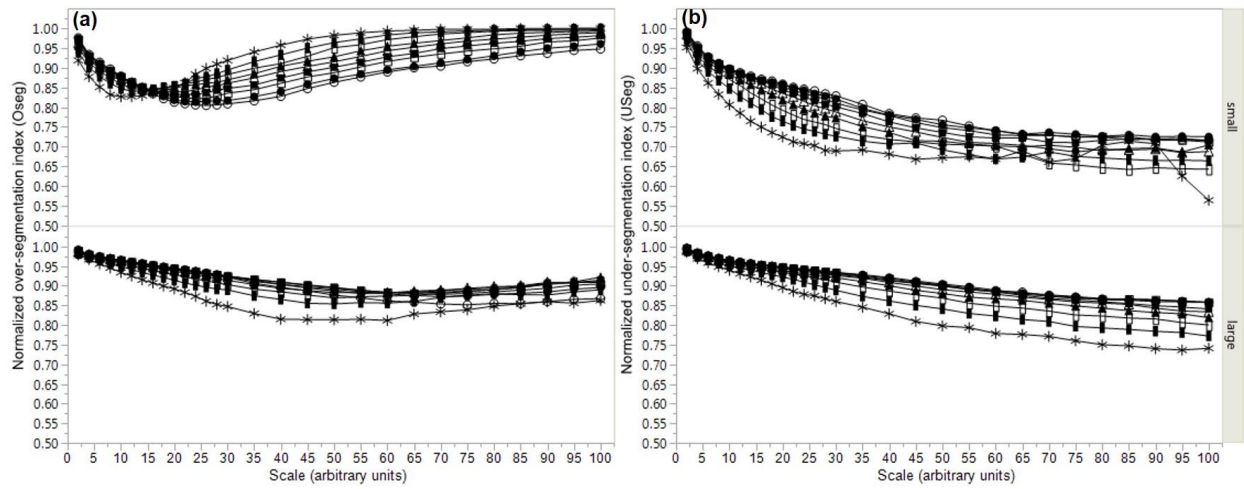


Figure 1.5: Topological congruence indices. (a) Under-segmentation index and (b) Over-segmentation index variation as a function of scale and shape for small and large field size class.

4.1.4. Variation in the arithmetic congruence indices

At SC 2, there was only 2 and 0.1% congruence in the mOi between the number of objects and the reference objects for both small and large objects, respectively (Figure 1.6a). For small objects, the mOi increased 50-fold by SC 30. Above scale 30, it continued to increase until it reached perfect congruence between objects by SC 100. For large objects at scale 100, there was a congruence of 76% between the number of image object segments and reference objects. mOi did not reach a maximum of 1 for larger objects, indicating that the scale parameter was not large enough to create a perfect one-to-one congruence. Higher values of SH (0.7-0.9) resulted in a higher mOi for all objects. On average the mOi, increased by 27% and 40% as the SH increased from 0.1 to 0.9.

As SC and SH increased, the undetected objects index decreased (Figure 1.6b) for both object size classes. The Udi remained nearly 1 for both small and large objects until it reached an SC of 6 and 30, respectively, at which point the number of missing objects increased. For small objects, as many as 92% of the objects were missing by SC value 100, while for large objects 48% of the objects were missing. For small objects, SH (0.1-0.4) resulted in higher nUdi between SC values of 2 to 14. At SC above 14, an SH value of 0.1 always caused the highest nUdi. For large objects, between SC values of 2-26, Udi remained near 1 at SH values of 0.1-0.9. Beyond SC 26, lower SH values resulted in the detection of the highest number of objects. The SH, caused the average Udi to decrease by 45% and 18% for small and large objects respectively.

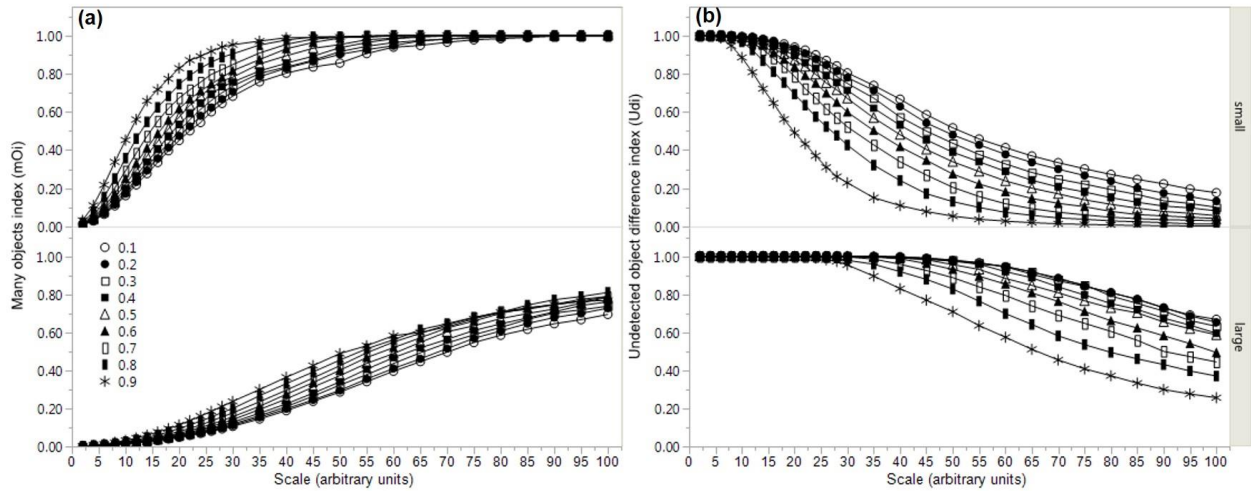


Figure 1.6: Arithmetic congruence indices. (a) Too many objects index and (b) Undetected object index and (b) variation as a function of scale and shape for small and large field size class.

4.2. Variation in the Overall Segmentation Quality Index

The mean OSI for small objects was highest at 0.79 at an SC value of 18 (Fig 1.7). The OSI changed by 30% as the SC scale increased from 2 to 100. At SC values of between 2 and 26, increasing SH values produced a small increase in the OSI except at an SH value of 0.9, which reduced the OSI. Between SC values of 26 and 100, the SH value of 0.1 caused the highest OSI.

For large reference objects, the highest average OSI was at an SC value of 55, and it changed by 2% as SC increased from 2 to 100. An increase in the SH (0.1-0.5) caused a 3% increase in the average OSI. However, an increase in the SH (0.5-0.9) led to a decrease in the OSI of 8%. OSI was the highest above an SC of 26 and as SH shifted from higher to lower values.

4.3. Global, per class and hierarchical best segmentation parameters

Best segmentation parameters for multiple scenarios in our study were determined using the OSI (Figure 1.8 and Table. 1.3). When the image was partitioned using a single set of parameters, the highest OSI is 0.83. Irrespective of the size of the objects the OSI did not change, however, per class, segmentation caused the highest OSI; the OSI was the highest for shadows and lowest for water. The OSI increased by up to 20% when the classes were segmented individually.

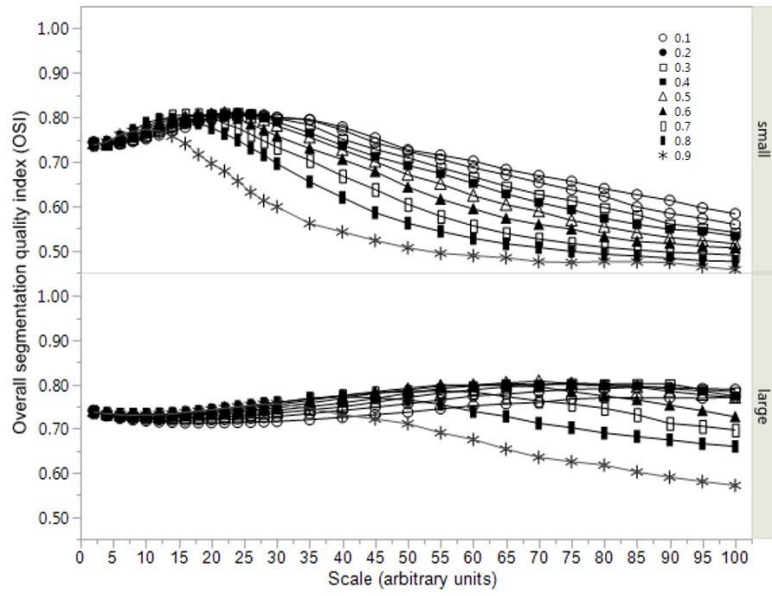


Figure 1.7: Overall segmentation quality index variation as a function of scale, shape, and compactness for small and large field size class.

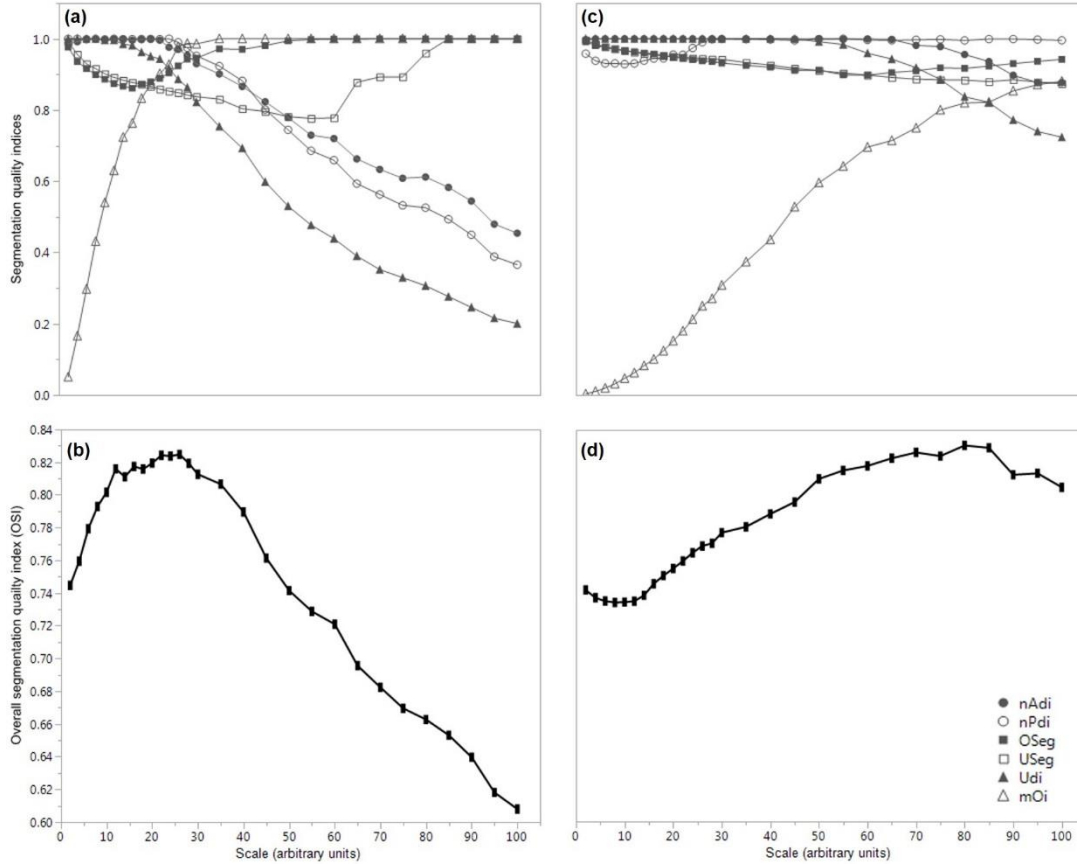


Figure 1.8: Maximum overall segmentation quality index (OSI) and geometric, topological and numerical congruence indices as a function of scale. The maximum value all of the geometric, spatial and numerical congruence indices as a function of the scale for (a) small objects and (c) large objects. Maximum overall segmentation quality index (OSI) for (b) small objects and (d) large objects. Geometric indices are represented by solid grey circles and open circles which denote the normalized area difference index (nA di) and normalized perimeter difference index (nP di) respectively. Solid grey and open squares represent the topological indices of under (U seg) and over-segmentation index (O Seg) respectively. Arithmetic congruence indices are symbolized by solid grey and open triangles for the many objects penalization index (m O i) and undetected object index (U di) respectively. The solid black line and vertical rectangles represent the combination of all the segmentation accuracy indices in the overall segmentation quality index (OSI). Each data point represents the average for each index ($n=81$). Error bars ± 1 SE.

5. Discussion

The selection of specific segmentation parameters to extract objects in an image constitutes a challenge, and often the selection is defined by the user's objective. Understanding how the segmentation parameters affect individual segmentation quality indices allows the user to design the best approach for the delineation and extraction of objects in an image. Our results suggest that scale and shape cause considerable variation in segmentation quality indices. Scale causes inter-scale variation, while the SH causes inter- and intra-scale variation.

5.1. Inter-scale variation

In the MRS algorithm, scale designates the maximum heterogeneity allowed within the image objects. Thus, as the scale parameter increases, more variability is allowed and hence a larger object size (Figure 1.9). Since the scale parameter controls the object size, it is expected to affect the different indices accordingly. For geometric indices, the smallest scale resulted in the highest congruence between image objects and reference objects. Our findings are consistent with (Liu et al., 2012), who reported that the segmentation quality rate (QR) is optimum at the smallest scale. At the smallest scale, single or few pixel image objects are created which correctly adjust and delineate the objects geometric characteristics. As the scale increases, the image object no longer conforms to the geometric characteristics of the reference object, and therefore the congruence between objects decreases.

Topological and arithmetic indices were also affected by inter-scale variation, yet the scale parameter had contrasting effects on the mOi and Udi, and OSeg and Useg (Figure 1.10). At lower scales, many image object segments are generated per corresponding reference object which led to a low many objects index. In contrast, the Udi is maximum at 1 because all objects

are classified. However, as segment size increases with scale, image object segments overlap multiple reference objects, and thus one or more reference objects are missing because they are assigned to the incorrect image object. On the other hand, a larger image object size reduces the penalization for generating too many image objects per reference object. There are tradeoffs between these two indices; the overlap of multiple reference objects by a segment has a much greater effect on the subsequent classification and mapping analysis than over-partitioning of an image object (Möller et al., 2007; Kim et al., 2011; Ma et al., 2017). The topological indices are complementary to the mOi and Udi but are affected differently by the scale. The initial decrease in OSeg and USeg was expected as the size of the image object increased with scale. Initially, the image object will intersect with the reference object almost entirely, yet as image object size increases the image object becomes larger than the reference object. Therefore, there is no longer over-segmentation but rather an increase in under-segmentation. The number of image objects simultaneously decrease in the segmented layer and under-segmentation increases.

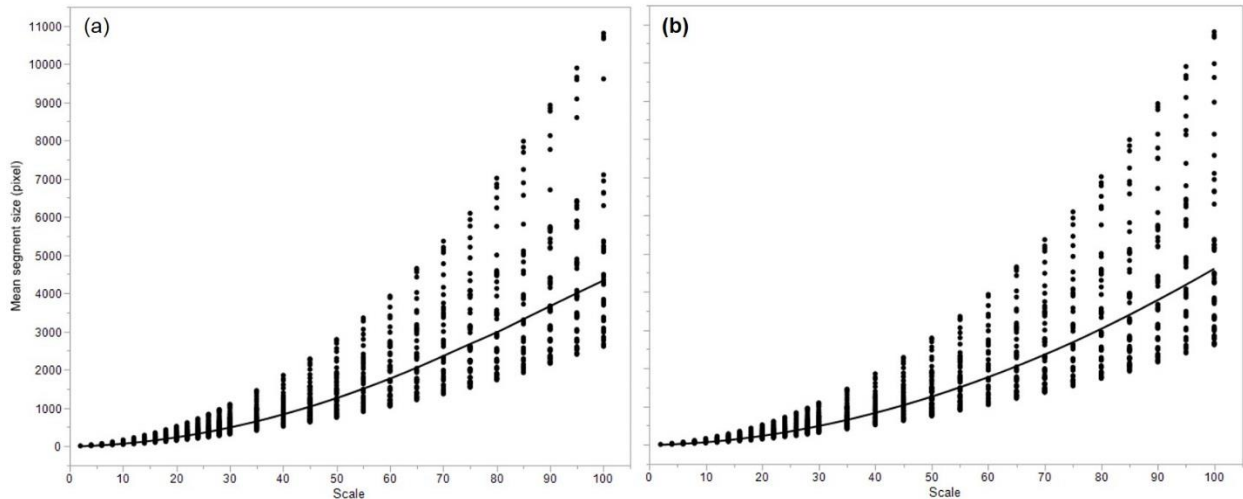


Figure 1.9: Effect of scale parameter on mean segment size. Mean segment size as scale parameter increases for (a) small size objects and (b) large size objects.

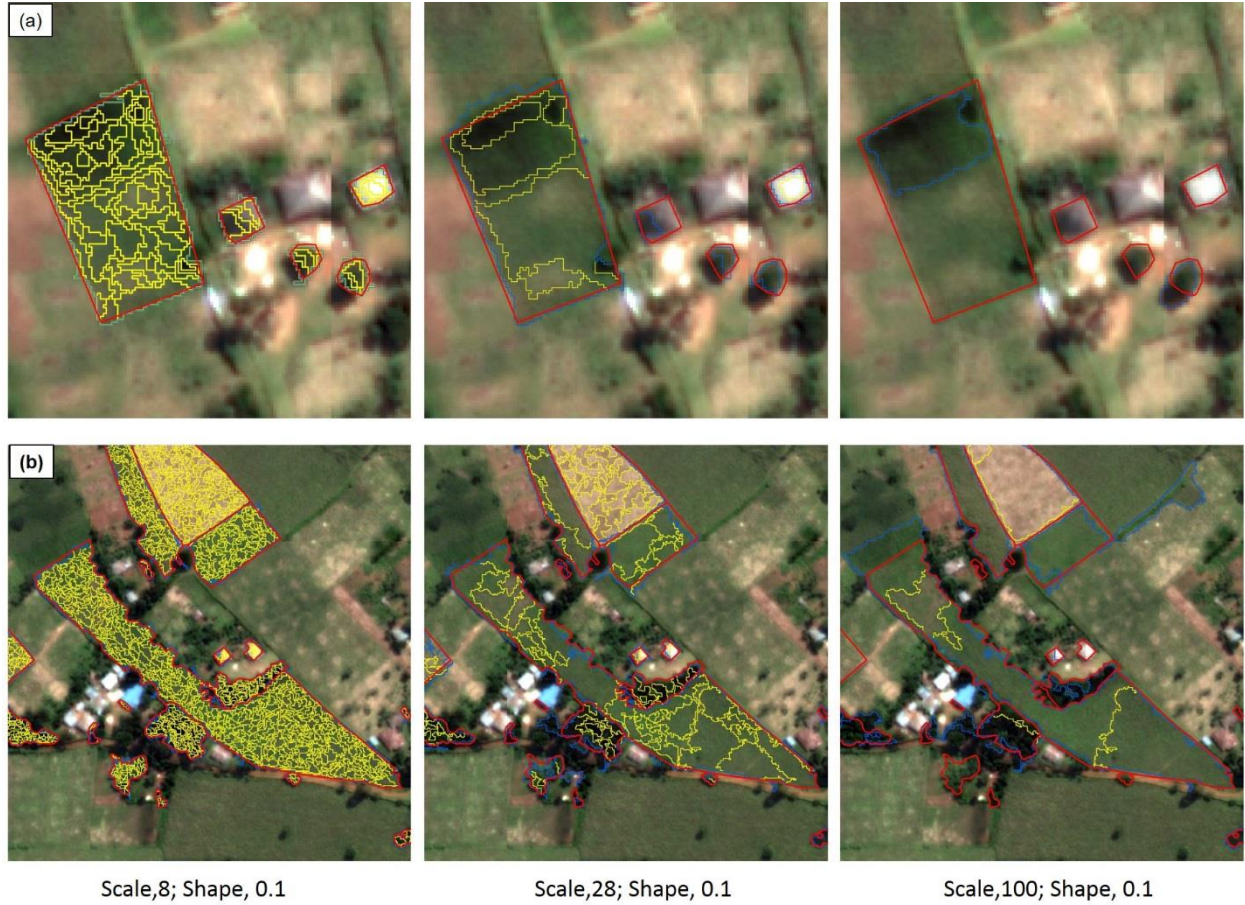


Figure 1.10: Illustration of the variation in topological and arithmetic indices as a function of scale. A subset of segmentation at various scales, 8, 28 and 100, to illustrate how segmentation indices change with increasing scale values for (a) small objects and (b) large objects. Comparison between the reference object (red) and the image object (blue) of geometric and topological characteristics. Image object segments (yellow) which correspond to the reference object.

5.2. Shape effect

Most studies focus on the effect of scale on segmentation and neglect to consider how shape and compactness can affect final segmentation accuracy. For the image studied, shape and compactness created variability for all the indices; however, shape introduced significant variability. Our results demonstrated that the shape parameter caused inter- and intra-scale variation. The shape parameter weights the color criterion against the geometric characteristics

of the object segment (Baatz and Schäpe, 2000; Tian and Chen, 2007; Pu, 2011). The shape parameter generated different effects between indices. For example, the nAdi, nPdi, and mOi showed higher congruence between objects when the shape parameter was larger, while OSeg, USeg and, Udi, had higher congruence at lower shape values (Figure 1.11). These findings suggest that larger shape values and lower scale values better define the geometric characteristics of objects. On the other hand, OSeg, USeg, and Udi were affected more by the spectral information within a scale. (Zhang et al., 2015) reported similar findings using precision and recall measures to assess segmentation quality. Their study concluded that a higher shape generally led to lower segmentation quality due to higher OSeg and Useg. As the segmentation scale increases, the effects of the parameters gradually shift for the nAdi, nPdi and OSeg. While the spectral information results in a higher area and perimeter congruence within a scale, the topological characteristics result in lower over-segmentation. Several studies (Laliberte et al., 2010; Pu and Landry, 2012) have reported that the color criterion creates objects that better represent real-world objects. According to our findings, this is accurate if the objects of interests have large areas, however, when the object of interest has a small area such as those in our study (47 m^2), the shape criteria exhibited greater influence on segmentation quality than did color criteria.

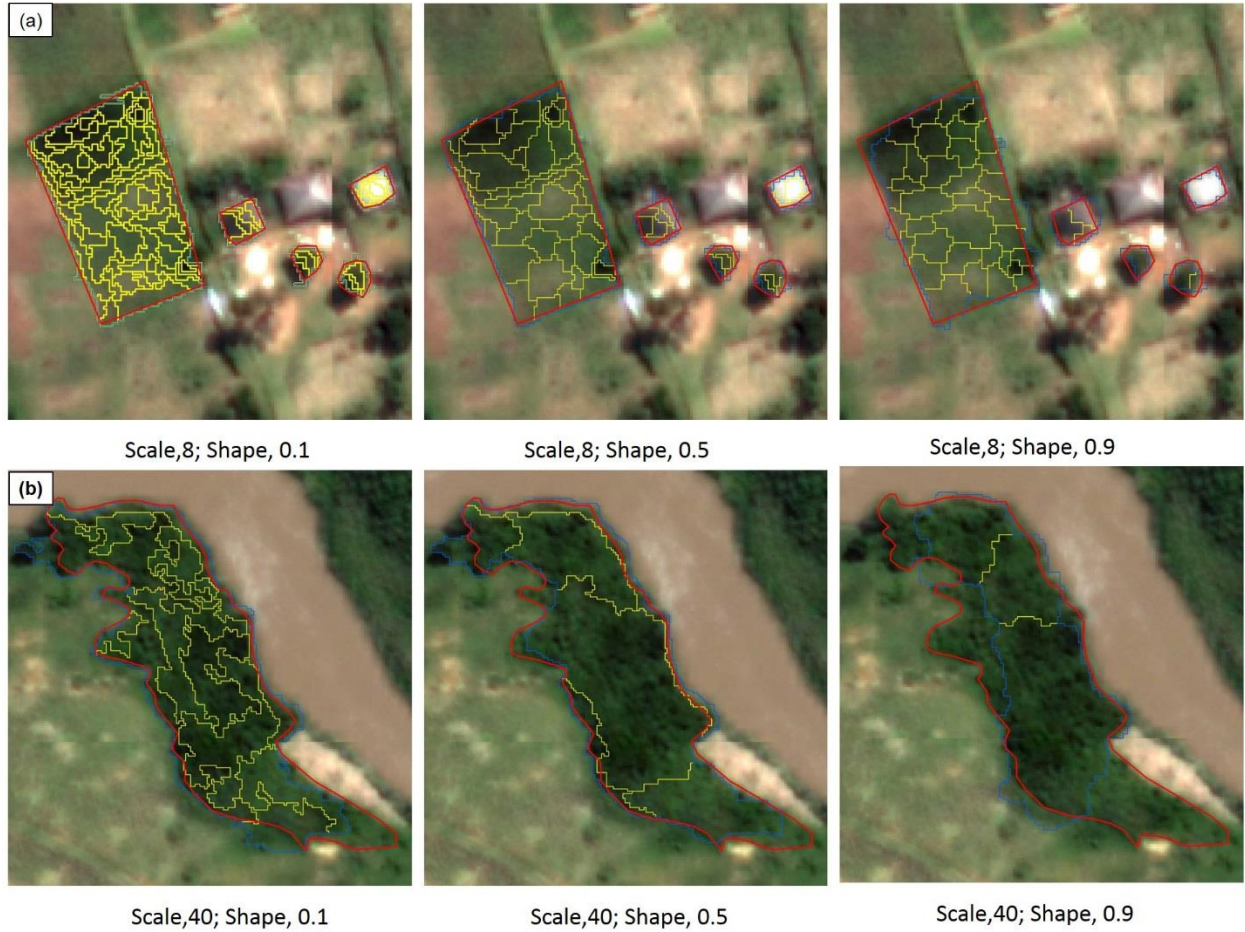


Figure 1.11: Illustration of the variation geometric, topological and arithmetic indices as a function of shape. Overlapping image object and reference layer, which illustrates how segmentation quality changes with increasing shape values 0.1, 0.5, 0.9. A subset of the segmentation for (a) small objects at fixed scale 8 and (b) large objects at fixed scale 40. Image objects (blue) and image sub-objects (yellow) compared to the reference layer (red).

5.3. Segmentation quality assessment

The selection of best segmentation parameters is based on the evaluation of geometric, topological and arithmetic indices that measures the congruence between image objects created in comparison to reference objects. If segmentation quality were evaluated based on individual indices, the best combination of parameters would result in the highest congruence and the least variability. For most of the indices, except the mOi, this means that the smallest scale, shape, and compactness values produce the highest congruence. These parameters generate numerous single or few pixel image objects that conform perfectly to the reference object, maximizing each index. Combining segmentation indices into one index prevents the selection of the smallest set of parameters.

The shape of the curve for OSI (Figure 1.8a-b) reached a maximum value, which represented the set of parameters that resulted in the highest overall segmentation quality for small objects. However, there are tradeoffs associated with the selection of the set of parameters with the highest OSI. While some of the geometric indices, nAdi and nPdi were highest until they reached the best set of parameters, the nUdi and USeg started decreasing at lower scale values. These two indices are mainly affected by the increasing size of image objects. Larger image objects can overlap multiple reference objects, and therefore, the reference objects are undetected and under-segmented. Under-segmentation and missing reference objects are considered an error in segmentation (Liu et al., 2012; Ma et al., 2015) which can cause additional errors downstream in image analysis. Interestingly, small-size objects were also affected by over-partitioning, but as the scale value increased, it reached its maximum at the optimum set of parameters. The generation of numerous small image objects is not considered as critical of an

error as the Udi or Useg (Kim et al., 2011; Liu et al., 2012; Witharana and Civco, 2014; Ma et al., 2015).

Segmentation quality of larger-size objects (Figure 1.8c-d) was affected differently by the indices. Unlike small objects, the Udi does not affect the OSI until scales above 50. However, the mOi affected the OSI significantly, changing across scale and never reaching its maximum value. The lack of perfect agreement between the number of image objects and reference objects suggest that reference objects were larger than the scale range selected. The small variation of the OSI across the scale range suggest that most of the indices were stable and remained at maximum throughout the segmentation. While the OSI is highest at a scale of 80, the Udi suggests that a scale parameter of approximately 40 would prevent any objects from being missed.

The indices which measure under-segmentation and undetected objects are the most important in selecting a set of optimum segmentation parameters. Therefore, different classes require different segmentation parameters. When all features are extracted using a single set of segmentation parameters, the overall segmentation quality will be lower (Table. 1.3). A hierarchical segmentation would avoid undetected objects or under-segmentation. An initial level of segmentation would choose a set of parameters that segments the image such that no objects are missing. At a higher level of segmentation, other criteria can be used to select the optimum set of parameters.

Table 1.3: Optimum segmentation parameter combination for scale, shape, and compactness identified by the OSI for, global scene, per size class and land cover class and hierarchical segmentation.

Class	Scale	Shape	Compactness	Optimal segmentation index (OSI)
Size class				
Small	26	0.3	0.4	0.83
Large	80	0.5	0.3	0.83
Land cover				
building	16	0.6	0.5	0.97
grass	22	0.6	0.4	0.93
maize	16	0.5	0.8	0.97
shadow	14	0.3	0.2	0.99
soil	22	0.5	0.7	0.95
tea	18	0.2	0.7	0.96
tree	12	0.6	0.9	0.98
trees/shrubs	22	0.7	0.4	0.91
water	65	0.3	0.6	0.83
Heirarchical				
Level 1	8	0.7	0.9	0.76
Level 2	80	0.5	0.3	0.83

6. Conclusion

The creation of an overall segmentation quality index is a viable alternative to the trial-and-error method of selecting segmentation parameters. Such an index offers a rigorous yet straightforward method to assess how segmentation can affect multiple object metrics and how these metrics affect overall segmentation quality. In this study, we found associations between the scale and shape parameters to the variability of multiple geometric, topological and arithmetic indices. We also suggest a simple mathematical measure based on congruence between image and reference object to evaluate image segmentation quality and select best segmentation parameters.

Our results suggest that scale and shape control a considerable portion of the variation seen in segmentation quality indices. The scale parameter is responsible for the variation of the indices between objects while the shape parameter impacted variation between objects and within objects. Based on these findings, when extracting a small object from an image, the shape parameter will define better objects of interest. Conversely, the color criterion generates more real-world objects when extracting larger objects. Understanding the variability that each segmentation parameter generates for individual indices ultimately explains the degree to which each index affects the overall segmentation index. Among the indices, the under-segment and undetected objects had the most substantial influence in the final segmentation quality. These two indices generate the highest error in image segmentation.

The segmentation quality assessment process we propose is a simple, objective method to select the best segmentation parameters for user-defined image analysis objectives. If the goal is to partition an entire image at once, then a single set of parameters can be selected which seeks

to maximize the overall segmentation quality index. In this case, there are tradeoffs among the different indices. A hierarchical segmentation with multiple sets of parameters at different segmentation levels is appropriate when the goal is to extract all features in the image without having any loss of objects. The user should define which object characteristics are of importance for segmentation quality. The segmentation quality assessment provides users with geometric, topological and arithmetic information to select the best protocol for segmentation of varying scenarios. These findings need to be verified by future research where the overall segmentation quality assessment protocol is applied to various high resolution images of complex landscapes and compared to other segmentation quality assessments previously proposed. Ultimately, such objective, semi-automated, segmentation protocols must result in image classification accuracies greater than those achieved by previously derived, empirical segmentation methods.

Acknowledgments

This study was supported in part by the National Science Foundation's Basic Research for Enabling Agricultural Development (NSF-BREAD Grant number IOS-0965336) and the Fondation des Fondateurs. DT acknowledges support from the NSF IGERT Program (DGE-0903371). Research of J. M. Peña, which contributed to this project, was financed by the Ramon y Cajal (grant number RYC-2013-14874) Program of the Spanish Ministry of Economy, Industry, and Competitiveness.

References

- Anders N.S., Seijmonsbergen A.C. and Bouten W. (2011) Segmentation optimization and stratified object-based analysis for semi-automated geomorphological mapping. *Remote Sens. Environ.* 115, 2976–2985. <https://doi.org/10.1016/j.rse.2011.05.007>
- Arvor D., Durieux L., Andrés S. and Laporte MA. (2013) Advances in geographic object-based image analysis with ontologies: a review of main contributions and limitations from a remote sensing perspective. *ISPRS J. Photogramm. Remote Sens.* 82, 125–137. <https://doi.org/10.1016/j.isprsjprs.2013.05.003>
- Baatz M., Hoffmann C. and Willhauck G. (2008) Progressing from object-based to object-oriented image analysis. In *Object-Based Image Analysis Lecture Notes in Geoinformation and Cartography*. Springer, Berlin, Heidelberg. pp. 29–42. Available at: http://link.springer.com/chapter/10.1007/978-3-540-77058-9_2 [Accessed May 8, 2018].
- Baatz M. and Schäpe A. (2000) Multiresolution segmentation: an optimization approach for high quality multi-scale image segmentation, in: Strobl, J. (Ed.), . Presented at the Angewandte Geographische Informationsverarbeitung XII. Beiträge zum AGIT-Symposium Salzburg 2000, Karlsruhe, Herbert Wichmann Verlag, pp. 12–23.
- Blaschke T. (2010) Object based image analysis for remote sensing. *ISPRS J Photogramm. Remote Sens.* 65, 2–16.
- Blaschke T., Hay G.J., Kelly M., Lang S., Hofmann P., Addink E., Queiroz Feitosa R., van der Meer F., van der Werff H., van Coillie F. and Tiede D. (2014) Geographic object-based image analysis – towards a new paradigm. *ISPRS J Photogramm. Remote Sens.* 87, 180–191. <https://doi.org/10.1016/j.isprsjprs.2013.09.014>
- de Bruin S., Wielemaker W. G. and Molenaar M. (1999) Formalisation of soil-landscape knowledge through interactive hierarchical disaggregation. *Geoderma* 91, 151–172.
- Clinton N., Holt A., Scarborough J., Yan L. and Gong P. (2010) Accuracy assessment measure for object based image segmentation goodness. *Photogramm. Eng. Remote Sensing* 76, 289–299.
- Drăguț L., Csillik O., Eisank C. and Tiede D. (2014) Automated parameterisation for multi-scale image segmentation on multiple layers. *ISPRS J. Photogramm. Remote Sens.* 88, 119–127. <https://doi.org/10.1016/j.isprsjprs.2013.11.018>
- Espindola G.M., Camara G., Reis I.A., Bins L.S. and Monteiro A.M. (2006) Parameter selection for region-growing image segmentation algorithms using spatial autocorrelation. *Int. J. Remote Sens.* 27, 3035–3040. <https://doi.org/10.1080/01431160600617194>
- Gao Y., Mas J.F., Kerle N. and Pacheco J.A.N. (2011) Optimal region growing segmentation and its effect on classification accuracy. *Int. J. Remote Sens.* 32, 3747–3763. <https://doi.org/10.1080/01431161003777189>

- Haralick R. M. and Shapiro L. G. (1985) Image segmentation techniques. *Comput. Vis. Graph Image Process* 29, 100–132.
- Hay G. J. and Castilla G. (2008) Geographic object-based image analysis (GEOBIA): a new name for a new discipline, in: Blaschke, T., Lang, S., Hay, Geoffrey J. (Eds.), *Object-Based Image Analysis, Lecture Notes in Geoinformation and Cartography*. Springer Berlin Heidelberg, pp. 75–89. https://doi.org/10.1007/978-3-540-77058-9_4
- Johnson B., Bragais M., Endo I., Damasa M.M. and Beatrice M.P. (2015) Image segmentation parameter optimization considering within- and between-segment heterogeneity at multiple scale levels: test case for mapping residential areas using Landsat imagery. *ISPRS Int. J Geoinf.* 4, 2292–2305.
- Kim M., Warner T.A., Madden M. and Atkinson D.S. (2011) Multi-scale GEOBIA with very high spatial resolution digital aerial imagery: scale, texture and image objects. *Int. J. Remote Sens.* 32, 2825–2850. <https://doi.org/10.1080/01431161003745608>
- Kuyah S., Dietz J., Muthuri C., Jamnadass R., Mwangi P., Coe R. and Neufeldt, H. (2012) Allometric equations for estimating biomass in agricultural landscapes: I. Aboveground biomass. *Agric. Ecosys. Environ.* 158, 216–224. <https://doi.org/10.1016/j.agee.2012.05.011>
- Laberte A.S., Browning D.M., Herrick J.E. and Gronemeyer P. (2010) Hierarchical object-based classification of ultra-high-resolution digital mapping camera (DMC) imagery for rangeland mapping and assessment. *J. Spat. Sci.* 55, 101–115. <https://doi.org/10.1080/14498596.2010.487853>
- Liu Y., Bian L., Meng Y., Wang H., Zhang S., Yang Y., Shao X. and Wang B. (2012) Discrepancy measures for selecting optimal combination of parameter values in object-based image analysis. *ISPRS J. Photogramm. Remote Sens.* 68, 144–156. <https://doi.org/10.1016/j.isprsjprs.2012.01.007>
- Lizarazo I. (2014) Accuracy assessment of object-based image classification: another STEP. *Int. J. Remote Sens.* 35, 6135–6156. <https://doi.org/10.1080/01431161.2014.943328>
- Lucieer A. and Stein A. (2002) Existential uncertainty of spatial objects segmented from satellite sensor imagery. *IEEE Trans. Geosci. Remote Sens.* 40, 2518–2521. <https://doi.org/10.1109/TGRS.2002.805072>
- Ma L., Cheng L., Li M., Liu Y. and Ma X. (2015) Training set size, scale, and features in geographic object-based image analysis of very high resolution unmanned aerial vehicle imagery. *ISPRS J. Photogramm. Remote Sens.* 102, 14–27. <https://doi.org/10.1016/j.isprsjprs.2014.12.026>
- Ma, L., Li M., Ma X. Cheng L. Du P. and Liu, Y. (2017) A review of supervised object-based land-cover image classification. *ISPRS J. Photogramm. Remote Sens.* 130, 277–293. <https://doi.org/10.1016/j.isprsjprs.2017.06.001>

- Möller M., Lymburner L. and Volk M. (2007) The comparison index: A tool for assessing the accuracy of image segmentation. *Int. J. Appl. Earth. Obs. Geoinf.* 9, 311–321. <https://doi.org/10.1016/j.jag.2006.10.002>
- O’Connell J., Bradter U. and Benton T.G. (2015) Wide-area mapping of small-scale features in agricultural landscapes using airborne remote sensing. *ISPRS J. Photogramm. Remote Sens.* 109, 165–177. <https://doi.org/10.1016/j.isprsjprs.2015.09.007>
- Pal N. R. and Pal S. K. (1993) A review on image segmentation techniques. *Pattern Recogn.* 26, 1277–1294.
- Persello C. and Bruzzone L. (2010) A novel protocol for accuracy assessment in classification of very high resolution images. *IEEE Trans. Geosci. Remote Sens.* 48, 1232–1244. <https://doi.org/10.1109/TGRS.2009.2029570>
- Pu R. (2011) Mapping urban forest tree species using IKONOS imagery: preliminary results. *Environ. Monit. Assess.* 172, 199–214.
- Pu R. and Landr S. (2012) A comparative analysis of high spatial resolution IKONOS and WorldView-2 imagery for mapping urban tree species. *Remote Sens. Environ.* 124, 516–533. <https://doi.org/10.1016/j.rse.2012.06.011>
- SAS Institute (2015) *JMP Pro.*, SAS Institute Inc, Cary, N.C.
- Schöpfer E., Lang S. and Albrecht F. (2008) Object-fate analysis - spatial relationships for the assessment of object transition and correspondence. In *Object-Based Image Analysis Lecture Notes in Geoinformation and Cartography*. Springer, Berlin, Heidelberg. pp. 785–801. Available at: http://link.springer.com/chapter/10.1007/978-3-540-77058-9_43 [Accessed June 7, 2018].
- Stehman S.V., Olofsson P., Woodcock C.E., Herold M. and Friedl, M.A. (2012) A global land-cover validation data set, II: augmenting a stratified sampling design to estimate accuracy by region and land-cover class. *Int. J. Remote Sens.* 33, 6975–6993. <https://doi.org/10.1080/01431161.2012.695092>
- Tian J. and Chen D.M. (2007) Optimization in multi-scale segmentation of high-resolution satellite images for artificial feature recognition. *Int. J. Remote Sens.* 28, 4625–4644. <https://doi.org/10.1080/01431160701241746>
- Wang L., Sousa W.P. and Gong P. (2004) Integration of object-based and pixel-based classification for mapping mangroves with IKONOS imagery. *Int. J. Remote Sens.* 25, 5655–5668. <https://doi.org/10.1080/014311602331291215>
- Witharana C. and Civco D.L. (2014) Optimizing multi-resolution segmentation scale using empirical methods: exploring the sensitivity of the supervised discrepancy measure euclidean distance 2 (ED2). *ISPRS J. Photogramm. Remote Sens.* 87, 108–121. <https://doi.org/10.1016/j.isprsjprs.2013.11.006>

- Ye S., Pontius Jr. R.G. and Rakshit, R. (2018). A review of accuracy assessment for object-based image analysis: from per-pixel to per-polygon approaches. *ISPRS J. Photogramm. Remote Sens.* 141, 137–147. <https://doi.org/10.1016/j.isprsjprs.2018.04.002>
- Zhan Q., Molenaar M., Tempfli K. and Shi W. (2005) Quality assessment for geo-spatial objects derived from remotely sensed data. *Int. J. Remote Sens.* 26, 2953–2974. <https://doi.org/10.1080/01431160500057764>
- Zhang X., Feng X., Xiao P., He G. and Zhu L. (2015) Segmentation quality evaluation using region-based precision and recall measures for remote sensing images. *ISPRS J. Photogramm. Remote Sens.* 102, 73–84. <https://doi.org/10.1016/j.isprsjprs.2015.01.009>
- Zhang Y.J., 1996. A survey on evaluation methods for image segmentation. *Pattern Recogn.* 29, 1335–1346. [https://doi.org/10.1016/0031-3203\(95\)00169-7](https://doi.org/10.1016/0031-3203(95)00169-7)

CHAPTER 2: CARBON AND NITROGEN EMISSIONS RATE AND HEAT TRANSFER OF AN INDIRECT PYROLYSIS BIOMASS COOKSTOVE

Abstract

Cookstoves where fuel is pyrolyzed or gasified have received much attention due to their potential to reduce environmental and household air pollution (HAP). In this study, an indirect pyrolysis cookstove was investigated to determine how operating conditions influence carbon and nitrogen emission rates and heat input to the cooking water. Multiple linear regression models were developed based on time-resolved measurements. The rate of pyrolysis fuel consumption emerged as the primary driver for the production of CO and NO emissions and heating of water. This parameter alone explained over 70% of the variation in the models for CO, NO and the water heating rate. The CO emission rate had a non-linear dependency on the rate of pyrolysis fuel consumption ($R^2=0.70$, $p<0.0001$), likely because high pyrolysis fuel consumption produced conditions with insufficient air flow for the conversion of C to CO₂. NO emission rates were mainly affected by the rate of N release from the pyrolysis fuel ($R^2=0.74$, $p<0.0001$). However, the pyrolysis temperature also affected the rate of production of NO, accounting for 4% of its variation. The water heating rate has a linear relationship to the rate of pyrolysis fuel consumption ($R^2=0.69$, $p<0.0001$). CO and NO emission rates depend on the speed of cooking and the choice of fuel, as well as on the amount of pyrolysis fuel used. Reduction of CO emissions and increase in efficiency are possible through stove design changes while choosing low-nitrogen pyrolysis fuel can lower NO emissions.

Keywords Indirect pyrolysis cookstove, emissions rate, carbon monoxide emission, nitric oxide emissions, heat transfer to water

1. Introduction

Nearly forty percent of global households use traditional biomass cookstoves to meet their household energy needs (Bonjour et al., 2013; Putti et al., 2015). However, these cookstoves experience conditions of incomplete combustion, producing undesirable gaseous and solid particle emissions (Ballard-Tremeer and Jawurek, 1996; Zhang et al., 1999; Venkataraman and Rao, 2001). Of particular importance are CO and NO, toxic air pollutants, which play a significant role in atmospheric chemistry, climate change (Crutzen and Andreae, 1990; Ludwig et al., 2003; Koppmann et al., 2005) and public health (Lim et al., 2012; Smith et al., 2014). Recent estimates indicate that biomass burning can contribute between 30-50% of global CO emissions (Granier et al., 2000; Holloway et al., 2000) and 20% of NO_x (Granier et al., 2000), an unknown percentage of which is due to biomass cookstoves. The development and use of more efficient biomass cookstoves could reduce the effects of biomass burning on the climate by reducing CO and NO and directly impacting human health (Anenberg et al., 2013).

CO and NO emissions have different formation mechanisms and can vary significantly by cookstove design, fuel type, operating conditions and combustion environment (Lamberg et al., 2017). In previous studies, fuel properties such as moisture content (Yuntenwi et al., 2008), ash content (Venkataraman and Rao, 2001), fuel type and N content (Kituyi et al., 2001; Deng et al., 2018) were found to correlate with the formation of CO and NO. Other factors such as combustion temperatures, air to fuel ratio, and burn rate, (Bhattacharya et al., 2002; Venkataraman et al., 2004; Roy and Corscadden, 2012; Tryner et al., 2014; Tryner et al., 2016) are also associated with CO and NO formation. Transient processes in the cookstove can occur at different time scales, affecting the formation of CO and NO. Some of these transients are associated with the feed rate of the fuel while others are associated with the batch nature of the

cookstove (Venkataraman et al., 2004; Tryner et al., 2014; Tryner et al., 2016; Nielsen et al., 2017). Transients in combustion conditions are important because they affect the formation of CO and NO, in turn causing major fluctuations in emissions rates (Venkataraman and Rao, 2001; Venkataraman et al., 2004; Tryner et al., 2014; Tryner et al., 2016). The transient nature of emissions rates due to varying operating conditions can lead to challenges in the control of CO and NO emissions from cookstoves.

A wide variety of improved cookstoves have been developed (Venkataraman and Rao, 2001; MacCarty et al., 2008; Roden et al., 2009; Jetter et al., 2012), including indirect pyrolysis cookstoves, also known as two-chamber cookstoves (Torres-Rojas et al., 2011; Deng et al., 2018). Indirect pyrolysis cookstoves are designed to produce combustion gases and heat for cooking in two separate chambers. Heat produced from wood burning in the combustion chamber is transferred to a separate batch of fuel in a pyrolysis chamber. As the fuel pyrolyzes, combustible gases evolve and flow into the combustion chamber, where they are further oxidized to produce cooking heat. The stove also produces a solid carbonaceous material in the pyrolysis chamber; this material can be used as fuel for other combustion devices, or as a soil amendment known as biochar (Lehmann, 2007).

The operating conditions in an indirect pyrolysis cookstove change over time, with the heating of the stove and water, the progress of the pyrolysis, and other factors (Deng et al., 2018). Little is known about how these changing operating conditions affect the production of CO and NO. It is worthwhile to investigate the variation of stove outputs with time and the relationship of stove outputs to time-dependent operating parameters. Therefore time-resolved measurements, also referred to as short-term averages, are essential to capture the dependence of stove performance on operating parameters. The variation of these conditions is highly

significant in a stove operating with a batch or semi-batch fuel feeding. Also, short-term average measurements are important for assessing human exposure to pollutants (Clark et al., 2013).

The purpose of this study was to quantify C and N emissions rates and the rate of heat transfer to water under varying operating parameters and to identify the key parameters influencing stove output through multivariate regression analysis. We hypothesized that emissions rate and water heating rate should be proportional to fuel consumption rate. We then sought to identify additional factors of importance, expecting the following to be significant: (a) fuel bound N content will result in a higher NO emissions rate; (b) fuel to air ratio and combustion quenching will be the primary drivers for the production of CO; and (c) the rate of heat transfer to water will depend on the water and gas temperatures.

2. Materials and methods

2.1 Cookstove and fuel description

The cookstove used in the study is a modification of the anila type pyrolysis cookstove first developed by U.N. Ravikumar from the Center for Appropriate Rural Technologies (CART) in India. Our earlier work (Deng et al., 2018), gives a brief description of the indirect pyrolysis cookstove used in this study. Additional images (Appendix Figure A1-2) and description of the operation of the cookstove is given in Appendix A2.1.

The instantaneous performance data set includes results for three different types of fuel; two brands of wood pellets (Instant Heat, Instantheat Wood Pellets Inc., Addison, NY; and Dry Creek, Biomaxx Inc., Pittsford, NY), corn stover pellets and switchgrass pellets (Deng et al., 2018). The pyrolysis fuels provided a range of N and ash content representative of potential solid fuels available to users of the cookstove. All pyrolysis fuels were in the form of pellets (15.8 mm L x 6.4 mm D) to improve experimental repeatability and exclude fuel size as a variable

affecting cookstove performance. Pinewood dowels, which have low N content, were used as the combustion fuel (120 mm L x 15 mm W). After each test, the remaining carbonaceous residue from combustion (referred as charcoal) and pyrolysis (referred as biochar) was collected, subsampled and stored for further analysis.

Solid fuel, charcoal, and biochar heating values were measured by bomb calorimetry using ASTM Standard Method D5865-13 (ASTM, 2013) and ASTM E711 – 87 (2004) (ASTM, 2004) on a Parr model 6200 (Parr Instrument Company, USA) calorimeter. Calculations were done using the lower heating value of fuel, biochar, and charcoal. Elemental composition of all materials was performed by dry combustion (NC2500, Carlo Erba, Italy coupled to a Thermo Scientific Delta V IRMS, Germany). Appendix Table A.1, lists the moisture content of the fuels used in this study. Appendix Table A.2 and Appendix Material in Deng et al. (2018) list the heating value and elemental composition of all fuels, charcoal, and biochar.

2.2. Sampling system and gaseous emissions monitoring

The sampling and gaseous emissions monitoring system details are described in Deng et al. (2018). Briefly, the gaseous emissions were captured using the “hood method” (Ballard-Tremeer and Jawurek, 1999; Venkataraman and Rao, 2001). The sampling system shown in Figure 2.1, consists of a hood attached to air ducts which draw room air through the hood and duct system, using an induced draft fan. Adjusting the speed of the fan controlled the extraction rate of the system. In order to determine the air mass flow rate through the extraction system, we injected a known flow rate of CO₂ into the duct and measured the final well-mixed CO₂ concentration. We used a probe to sample gases in the fully-developed flow region downstream of the duct inlet.

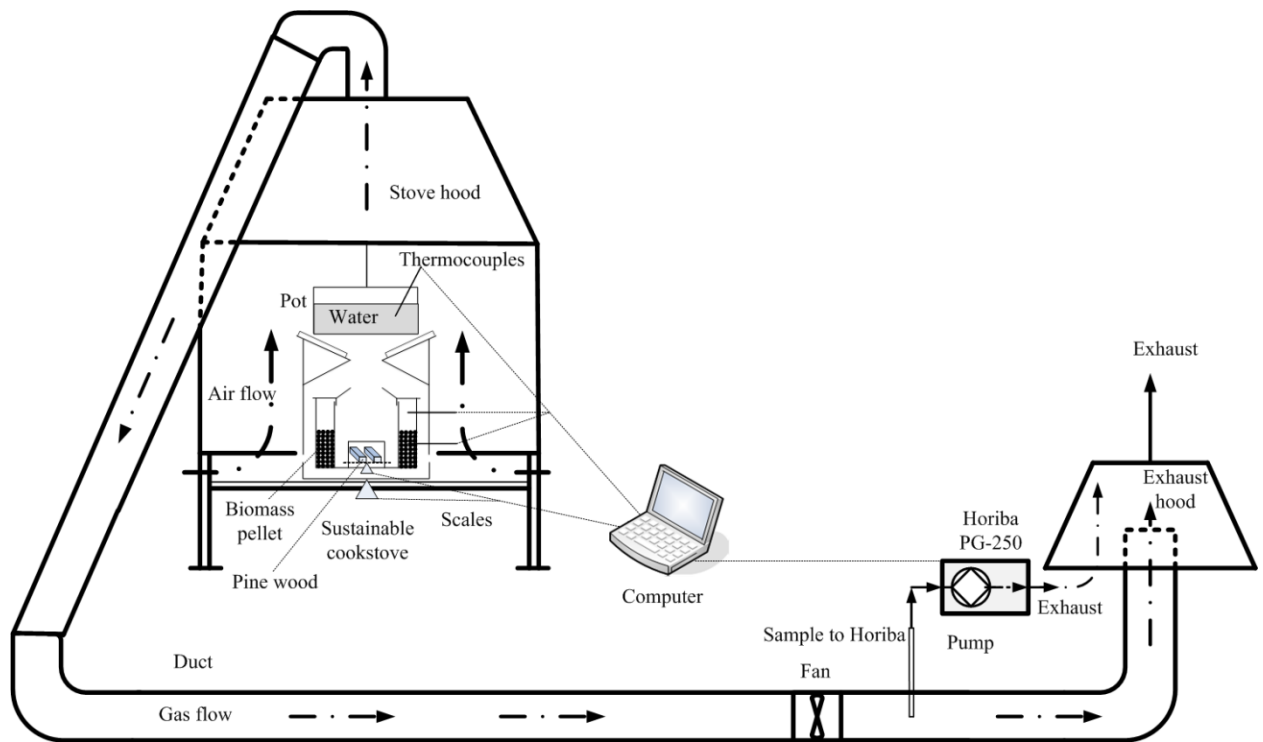


Figure 2. 1: Schematic of cookstove setup and gaseous sampling system

2.3. Test protocol

Various testing protocols have been developed to evaluate and compare cookstove performance under controlled conditions. Among them, the water boiling test (WBT) (Partnership for Clean Indoor Air., 2013) has been the most widely accepted as the standard. The WBT is a simplified version of the cooking process. The purpose of the test is to measure the efficiency with which a cookstove can deliver heat to a pot of water and measure the gaseous and particulate emissions produced during the test. The WBT consists of three phases that aim to simulate the various stages of cooking. Each stage affects the production of emission and heat differently. The WBT and other tests such as the Stove Manufacturers Emissions and Performance Test Protocol (EPTP) (DeFoort et al., 2010) are well suited to test cookstoves used for continuous combustion conditions (Taylor, 2009; Roth, 2013; Jetter, 2013). However,

difficulties arise when using the WBT or EPTP for batch and mixed feed stoves, including pyrolysis stoves (Marufu et al., 2000). Therefore, for this study, the WBT was modified based on the observed burn cycle for pyrolysis cookstoves, to capture all emissions during stove operation. The complete details of the cookstove test protocol and the modifications to the WBT are described by Deng et al., (2018).

2.4. Calculations and data analysis

2.4.1. Time-resolved stove outputs and models describing them

Table 2.1 lists quantities measured at one-second intervals during the modified water boiling test. The raw data for combustion and pyrolysis fuel masses (Appendix Figure A.3) and other measured variables (Table 2.1) was processed, as described below and in Appendix A Section 2.2.1 to obtain short-term averages of stove outputs, operating parameters (Table 2.2), and to develop multivariate linear models for the key stove outputs.

Table 2.1: Quantities measured directly, at 1-second intervals during the burn cycle

<i>Variable measured</i>	<i>Description</i>	<i>Units</i>
m_c	combined mass of the combustion wood, its char, and grate that they rest on	g s^{-1}
m_s	mass of the stove and its contents, including m_w , but not including the pot suspended above	kg s^{-1}
T_w	temperature of water in pot	$^{\circ}\text{C}$
T_1	temperature of the pyrolysis fuel bed	$^{\circ}\text{C}$
X_{CO}	mole fraction CO measured in a well-mixed portion of the exhaust duct	dimensionless
X_{CO_2}	mole fraction CO ₂ measured in a well-mixed portion of the exhaust duct	dimensionless
X_{NO}	mole fraction NO measured in a well-mixed portion of the exhaust duct.	dimensionless

Table 2.2: Independent variables (representing stove operating conditions) and dependent variables (representing key stove outputs) in the stepwise regression models

<i>Variable</i>	<i>Description</i>	<i>Units</i>
<i>Dependent variables</i>		
\dot{m}_{CO}	Carbon monoxide emissions rate	mg s^{-1}
\dot{m}_{NO}	Nitric oxide emissions rate	mg s^{-1}
\dot{Q}_w	Rate of heat input to the water	kJ s^{-1}
<i>Independent variables considered</i>		
\dot{m}_c	Combustion fuel consumption rate	g s^{-1}
\dot{m}_{py}	Pyrolysis fuel consumption rate	g s^{-1}
\dot{m}_{py}^2	Rate of pyrolysis fuel consumption squared	$\text{g}^2 (\text{s}^2)^{-1}$
f_{py}^{\S}	Fraction of pyrolysis completed	dimensionless
T_1	Temperature of the pyrolysis fuel	$^{\circ}\text{C}$
T_w	Temperature of the water in the pot	$^{\circ}\text{C}$
X_n	Mass fraction N in the pyrolysis fuel	dimensionless
$\dot{m}_{py} * X_n$	Rate of nitrogen release from pyrolysis fuel	g s^{-1}

[§] equation defined in section 2.5 of the Appendix A

Three key stove outputs were selected as dependent variables: emission rates for CO and NO (undesired stove outputs), and the rate of heat flow to the water, \dot{Q}_w (desired stove output) (Table 2.2). CO and NO emission rates represent the source terms for gaseous household air pollution or for greenhouse gas emissions. \dot{Q}_w is the rate of heat flow to the water (kW), also known as the useful firepower of the stove (DeFoort et al., 2010) and calculated as:

$$\dot{Q}_w = C_{p_w} * m_{H_2O} * \dot{T}_w$$

where C_{p_w} is the specific heat of water ($\text{kJ kg}^{-1} \text{K}^{-1}$), m_{H_2O} is the mass of the water (kg) and \dot{T}_w is the rate of water temperature increase (K s^{-1}). This calculation neglects heat loss from the water and water evaporation, thus assuming that all heat entering the water goes into raising its temperature.

These key stove outputs are influenced by stove operating conditions, which can be described using the independent variables given in Table 2.2, such as rate of pyrolysis fuel consumption, rate of combustion fuel consumption, pyrolysis temperature, the temperature of the water in the pot, and mass fraction of N in fuel. Plots (Appendix Figure A.5) showing the behavior of each of the independent variables considered are presented in the Appendix A Section 2.2.1.

2.4.2. Statistical analysis

A multivariate linear regression describing the relationships among each dependent variable and the relevant independent variables was developed as follows. Stepwise regression was performed using JMP version 12.0.1 (SAS Institute, 2015) to select the most significant of the independent variables for inclusion in multivariate linear models. P-value thresholds of 0.1 were used to allow an independent variable to enter the model, while 0.01 was used to remove an independent variable from the model. A mixed stopping rule was applied to allow the alternation

of forward and backward steps. This process allows the most significant terms to enter the model and the least significant terms to leave. The variance inflation factor (VIF), is used to detect any collinearity between the predictor variables. If the VIF was less than 10, the variables are considered to be uncorrelated.

3. Results and discussion

3.1. Qualitative description of stove operating conditions

The stove behavior develops over the course of three phases (Figure 2.2), each corresponding to the heating of one pot of water from room temperature to 100°C. In Phase I of the test (pre- and early pyrolysis), a cold pot of water is placed on the cookstove, and the wood fire is initiated in the combustion chamber. During this phase, the stove heats up (Appendix Figure A.5). Significant mass loss of pyrolysis fuel occurs in the second half of the phase. Emissions are relatively low, and they increase at the onset of devolatilization (Figure 2.2). During Phase II (main pyrolysis), the cookstove is already hot. Devolatilization of pyrolysis fuel is the dominant process at this stage, accompanied by high exhaust mole fractions for all measured species (Figure 2.2). In Phase III (post-pyrolysis), devolatilization of pyrolysis fuel is almost complete (Appendix Figure A.5). Thus, the combustion fuel is the primary source of heat and emissions. Emissions drop considerably compared to the previous stage but are still somewhat higher than at the beginning of the test. The rate of heat input to the water differs in the different phases of pyrolysis. The rate of change in the water temperature is highest during the peak fuel devolatilization periods (Appendix Figure A.5). The water heating rate is lowest during phase three, as pyrolysis reactions cease or decrease and wood combustion becomes the main heating source.

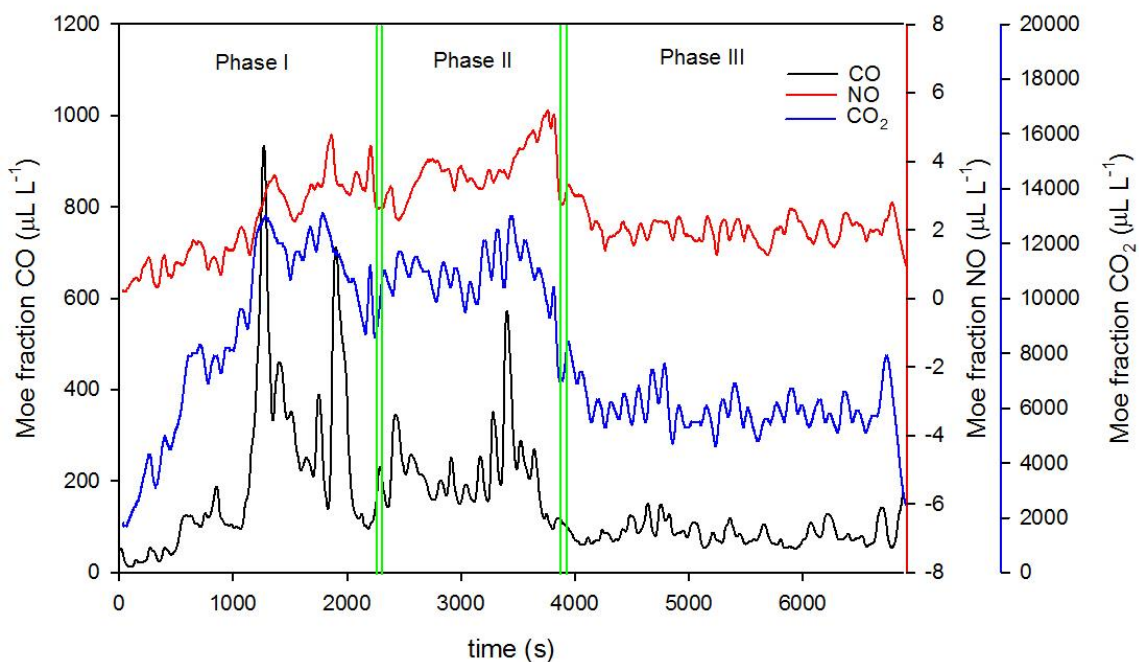


Figure 2.2: Gas pollutant emissions concentration of CO, NO and CO₂ for wood pellets pyrolyzed in an indirect pyrolysis cookstove. Green horizontal lines represent the varying phases of pyrolysis happening during the cooking test. Phase (I) is pre and early pyrolysis, Phase (II) main pyrolysis and Phase (III) is post-pyrolysis. The lines also indicate the time at which a new pot of cooking water was placed over the cookstove.

3.2. Models of key stove outputs as functions of operating parameters

Some qualitative trends of variables such as pyrolysis fuel consumption are shown by the plots of stove outputs (Figure 2.3) and operating parameters vs. time (Appendix Figure A.4). Multivariate linear models relating short-term average stove outputs to operating parameters averaged over the same time periods provide a more quantitative description of the relationship between stove outputs and operating conditions. If stove operating conditions were not relevant, we would expect each of the three key stove outputs to be simply proportional to the rate of consumption of fuel (Tables 2.3 and 2.4). In other words, a certain amount CO and

NO will be produced, and a certain amount of heat would be transferred into the water, whenever a given mass of fuel is consumed. In this case, the multivariate linear model would identify only \dot{m}_c and \dot{m}_{py} as significant variables. Instead, different or additional operating parameters are identified as important in predicting each of the key stove outputs. These findings are discussed in the sections below.

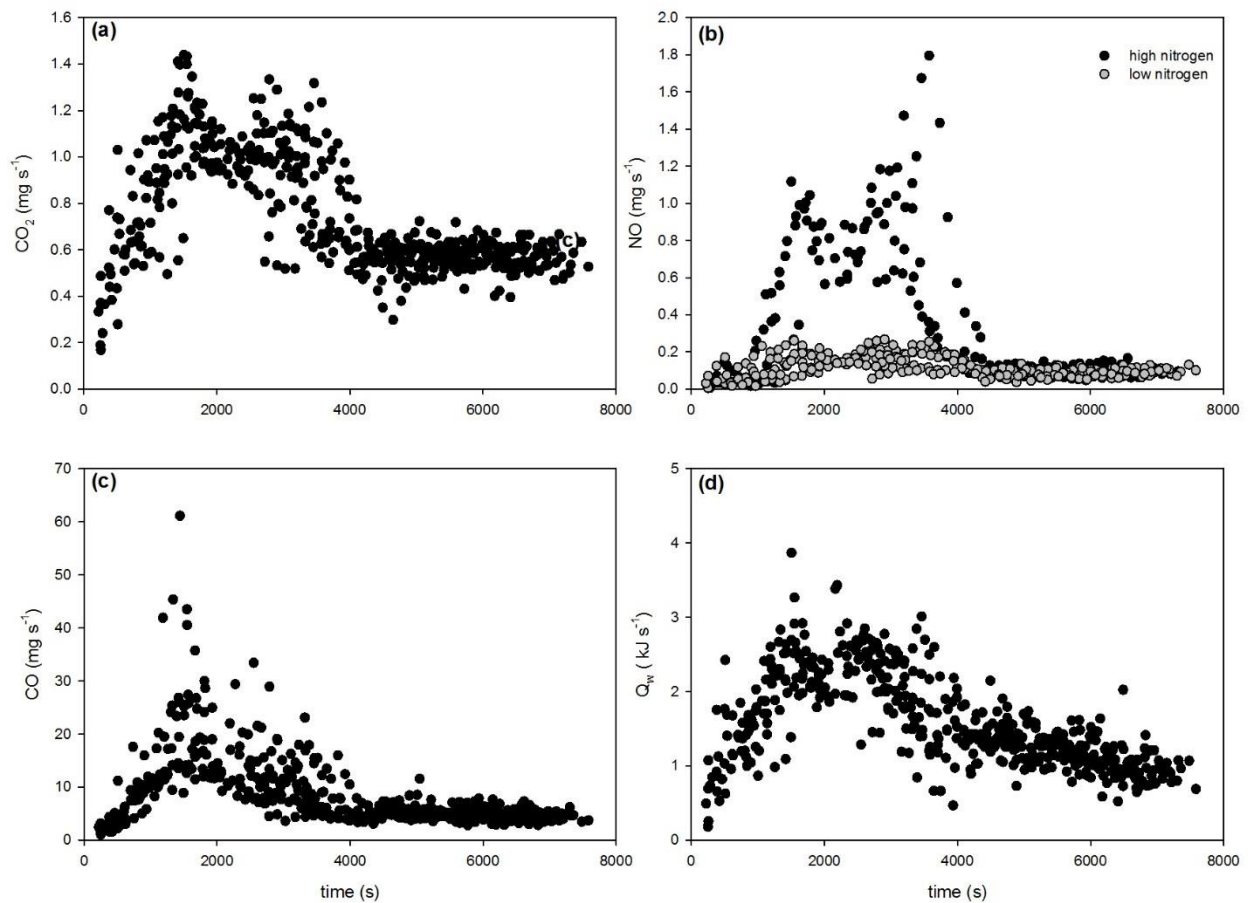


Figure 2.3: Short-term average for gaseous emission rates and heat input to water. The quantity of each gaseous emissions as a function of time for (a) CO₂, (b) NO and (c) CO and (d) the heat input to cooking water (\dot{Q}_w). Each point ($n=485$) represents a short-term average determined from data from eleven water boiling tests. Grey circles and black circles in (b) represent low N content woody biomass and high-N-content of herbaceous biomass (corn and switchgrass)

3.2.1 Effects of operating parameters on CO emissions rate

The measured CO emission rates between 1.0 and 61 mg s⁻¹ (Figure 2.3c) with an average of 8.9 mg s⁻¹ were consistent with CO emission rates obtained for various char producing cookstoves (1-300 mg s⁻¹) (Tryner et al., 2014). Stove operating conditions are expected to affect CO emissions in two ways. Flame quenching in low-temperature zones and insufficient oxygen due to inadequate airflow or poor mixing can hamper the conversion of CO to CO₂, and thus lead to CO emissions to the environment (Flagan, Richard C and Seinfeld, John H., 1988). Thus variables associated with flame quenching or insufficient oxygen are expected to appear as significant independent variables in the multivariate model. If, on the other hand, operating parameters were not relevant, then the CO emissions rate (\dot{m}_{CO}) would be linearly proportional to the rate of combustion fuel consumption and rate of pyrolysis fuel consumption (\dot{m}_c and \dot{m}_{py}) with no other significant independent variables.

The model indicates that the CO emissions rate (\dot{m}_{CO}) is most closely related to the squared rate of pyrolysis fuel consumption, \dot{m}_{py}^2 (Table 2.3). This variable explains 70% of the variance in the model for the CO production rate. The sequential inclusion of the rate of combustion fuel consumption (\dot{m}_c) and the rate of N released from the pyrolysis fuel ($\dot{m}_{py} * X_n$) accounted for only an additional 3.0% and 0.5% of the model variance, respectively.

The dependence on the rate of pyrolysis fuel consumption squared, \dot{m}_{py}^2 rather than on the rate of pyrolysis fuel consumption, indicates that the CO production is disproportionately high during high pyrolysis-fuel mass loss periods. This finding is consistent with the oxygen-starvation mechanism for CO emissions. At times of greatest pyrolysis fuel mass loss rate, it appears that the natural draft airflow is insufficient to complete combustion converting CO to CO₂. Thus a large fraction of C remains as CO rather than being converted to CO₂ during those

times. Interestingly, the second possible influence of operating conditions on CO production was not borne out by the variables selected in the model. We hypothesized that CO emission production rates would be influenced by thermal quenching of combustion before the CO is converted to CO₂. If this process were important for the pyrolysis cookstove, the model would show the water temperature T_w as an important variable, because quenching would be stronger when the water temperature was low (immediately after the pot had been changed). As T_w was not selected as an influential variable, this possible mechanism of CO production appears to be relatively unimportant for the pyrolysis cookstove.

Table 2.3: Stepwise regression input variables, resulting predictor variables and coefficient of determination. The predictor variables are listed in decreasing order of importance.

\dot{m}_{CO}			\dot{m}_{NO}			\dot{Q}_w		
Input variables	Predictor* variables	R ²	Input variables	Predictor variables	R ²	Input variables	Predictor variables	R ²
\dot{m}_c	\dot{m}_{py}^2	73.48	\dot{m}_c	$\dot{m}_{py} * X_N$	78.69	\dot{m}_c	\dot{m}_{py}	76.68
\dot{m}_{py}	\dot{m}_c		\dot{m}_{py}	T_1		\dot{m}_{py}	T_w	
\dot{m}_{py}^2	$\dot{m}_{py} * X_N$		\dot{m}_{py}^2	\dot{m}_{py}		\dot{m}_{py}^2	T_1	
f_{py}			f_{py}			f_{py}	\dot{m}_c	
T_1			T_1			T_1		
T_w			T_w			T_w		
X_N			X_N			X_N		
$\dot{m}_{py} * X_N$			$\dot{m}_{py} * X_N$			$\dot{m}_{py} * X_N$		

*In order of decreasing importance in the model

3.2.2. Effect of operating parameters and fuel characteristics on NO emissions rate

The NO emission rates were lower for fuels with low N content ($0.006\text{-}0.32\text{ mg s}^{-1}$) than for fuels high N content ($0.008\text{-}2.16\text{ mg s}^{-1}$), i.e., corn and switchgrass (Figure 2.3b). This difference is consistent with the finding of previous cookstove studies considering NO (Ndiema et al., 1998; Marufu et al., 2000; Kituyi et al., 2001; Zhang et al., 2008; Roy and Corscadden, 2012; Deng et al., 2018).

NO is known to be formed by several combustion-related processes, mainly (1) conversion of fuel-bound N compounds, and (2) reactions involving N_2 and O_2 from the air, occurring most rapidly at very high temperatures and fuel-lean conditions. The fuel-bound N mechanism is dominant for most solid fuels but is influenced by temperature and fuel and air mixing (Glarborg et al., 2003). Thus it was anticipated that variables related to fuel N content and fuel-to-air ratio and flame temperature would be identified as significant.

By far the largest portion of the variance of \dot{m}_{NO} (73.96 %) is explained by the rate of N release from the pyrolysis fuel ($\dot{m}_{py} * X_n$). Pyrolysis temperature, T_1 accounts for (4.3 %) of the variance, and \dot{m}_{py} by itself makes only a small contribution (0.43%) to the model (Table 2.4) beyond the contribution to ($\dot{m}_{py} * X_n$). The positive dependence of \dot{m}_{NO} on pyrolysis temperature (T_1) also suggests that the N release from the pyrolysis fuel is not uniform, and that it is favored by higher-temperature conditions.

Table 2. 4: Stepwise regression coefficients and collinearity statistics of regression models

Dependent variables	Predictors	Coefficient Estimate	Standard error	t statistic	Standardized coefficients	VIF
\dot{m}_{CO}	Intercept	-6.10E-04	8.24E-04	-0.74	0.00	
	\dot{m}_{py}^2	5.69E-02	1.82E-03	31.30	0.94	1.63
	\dot{m}_c	18.65	2.64	7.13	0.17	1.09
	$\dot{m}_{py} * X_n$	-2.58	0.85	-3.03	-0.09	1.59
\dot{m}_{NO}	Intercept	-1.22E-04	2.13E-05	-5.74	0.00	
	$\dot{m}_{py} * X_n$	1.02	0.03	31.97	0.88	1.71
	T_1	5.44E-07	5.29E-08	10.28	0.23	1.16
	\dot{m}_{py}	0.12	0.04	3.15	0.09	1.74
\dot{Q}_w	Intercept	0.01	2.36E-03	6.21	0.00	
	\dot{m}_{py}	66.59	1.83	36.34	0.98	1.47
	T_w	-1.56E-04	1.51E-05	-10.32	-0.26	1.23
	T_1	3.13E-05	3.27E-06	9.57	0.27	1.57
	\dot{m}_c	29.72	5.51	5.39	0.14	1.27

Interestingly the degree to which the pyrolysis is completed (f_{py}) was not important in predicting NO production. Completion of pyrolysis was expected to be important in NO production because different N-containing species are released during different parts of the pyrolysis process (Winter et al., 1999; Glarborg et al., 2003). If this effect occurs, it appears that pyrolysis temperature (T_1) is a better predictor of it than the degree of completion of pyrolysis is.

3.2.3. Effects of operating parameters on the rate of heat input to the water

The heat input rate to the water (useful firepower) ranged from 0.18 to 3.86 kW, with an average of 1.58 kW. Other studies (Jetter et al., 2012), have reported similar findings for char producing cookstoves. However, there is a quite a significant variation in the rate of heat input to the water during the entire WBT (Figure 2.3d). The highest heat input rate occurs during the end of Phase I (early pyrolysis) and Phase II of the stove operation (main pyrolysis).

The sources of the heat input to the water are the combustion of wood and pyrolysis gases. Thus, if operating conditions were not relevant, we would find that rate of heating the water (\dot{Q}_w) would be proportional to the rates of consumption of combustion fuel and pyrolysis fuel (\dot{m}_c and \dot{m}_{py}) with no other significant independent variables. This simple relationship is reflected in the definition of cookstove efficiency. Variation in operating conditions might affect the rate of heat transfer into the pot through competing processes (e.g., heating up of the stove) or through changes in gas flows and temperatures that would affect the heat transfer coefficient. In other studies, gas temperature, fuel mass flow rate and firepower are variables found to influence the heat input to the water (Zube, 2010).

In our model, the rate of pyrolysis fuel consumption (\dot{m}_{py}) has a strong positive correlation and greatest effect on the heat input rate to the water (Table 2.4). It accounts for 69% of the variance in the model. The water temperature, T_w has a relatively strong negative relationship (-0.26) with \dot{Q}_w and explains an additional 3% of the variance. Pyrolysis temperature, T_1 and \dot{m}_c also have a positive correlation with the heat input rate to water, however, T_1 has a stronger influence over \dot{Q}_w than \dot{m}_c . The stepwise regression model developed in our study explains 77% of the variation in \dot{Q}_w (Tables 2.3 and 2.4). The degree to which the pyrolysis was completed (f_{py}), was also expected to appear in the model for water heating rate, because heat transfer into the pyrolysis chamber competes with heating of water. The presence of the closely related variable T_1 may explain the fact that f_{py} was not selected.

The rate of pyrolysis fuel consumption is the most influential parameter in our model; as the rate of pyrolysis, fuel consumption increases the heat input to the water increases. As mentioned above, this finding makes sense because pyrolysis fuel consumption is the main source of the heat output. On the other hand, the contribution of heat input to the water from the

mass flow rate of combustion fuel is relatively small in comparison to that of the pyrolysis fuel, because combustion fuel is fed at regular time intervals and thus little variation in this variable is present in the dataset.

Pyrolysis fuel temperature and water temperature played a major role in determining the rate of heat output from the stove. The pyrolysis fuel temperature may appear in this model because it is strongly related to the thermal energy stored in the stove. At the start of the test, a significant fraction of the fuel's heat release is used to heat the stove, i.e., to increase the thermal energy stored in the stove. Once the stove is hot, this undesired use of the heat release is no longer active and does not compete with heat transfer to the pot. The positive relationship between \dot{Q}_w and T_1 may represent this transition. In addition, the water temperature (T_w) also affected the heat input rate to the water. As the water temperature increased, the rate of heat input decreased. The heat transfer rate (for pure convection) is expected to be linearly proportional to the difference between gas temperature and pot temperature. Thus, as the water temperature increases the heat transfer rate should get smaller, which is reflected in our observations.

4. Conclusions

Indirect pyrolysis cookstoves represent an alternative to traditional solid fuel open fires. Not only do they offer the versatility of being able to use a wide variety of fuels but also can be used in various modes of operation. It is important to understand the mechanisms that are responsible for desirable and undesirable stove outputs in order to make useful improvements to stove design and use. In this study, we found empirical associations between thermal, chemical and physical operating parameters of an indirect pyrolysis cookstove and the production of selected gaseous emissions and useful heat. Keeping only the most important single variable in

each model, we obtain a low-order description of the stove's operation, one that accounts for over seventy percent of the variation of each output variable.

According to this description, the water heating rate is proportional to the pyrolysis fuel consumption rate, implying that we must use a certain amount of pyrolysis fuel to perform a given heating task with this stove. The amounts of NO and CO produced depend on how the heating is accomplished when a given amount of pyrolysis fuel is used. NO production is proportional to the product of the mass fraction N in the pyrolysis fuel and the rate of pyrolysis fuel consumption, indicating that the amount of NO produced in a given cooking task depends on the choice of fuel. For CO, the rate of pyrolysis fuel consumption appears in the model multiplied by itself, indicating that the amount of CO produced in a given cooking task depends on the rate of pyrolysis, (i.e., on the speed of cooking).

These models imply two important tradeoffs. First, the NO emissions model indicates clearly that high nitrogen content in fuels, typical of waste biomass, is associated with high NO emissions for a given cooking task. Though indirect pyrolysis cookstoves have the versatility of being able to operate with waste fuels in the pyrolysis chamber, they produce more NO when waste fuels are used. Second, the model for CO emissions indicates that rapid cooking is associated with high CO emissions for a given cooking task. There is a tradeoff between avoiding CO emissions and accomplishing a cooking task quickly. Using waste biomass, or cooking rapidly, does not have a strong impact on the quantity of fuel used for a given cooking task; the tradeoffs are essentially associated with emissions.

The emissions models have implications for the design and operation of future stoves. Stove design changes that reduce the rate of pyrolysis fuel consumption or increase the airflow rate are likely to reduce CO emission rates. For example, increasing the height of the stove or the

internal gas temperature by insulating the stove or its chimney if applicable, can improve airflow by increasing the driving force of natural convection. Reducing the rate of pyrolysis fuel consumption may be achievable through changes in the geometry of the pyrolysis chamber. Fuel choice, rather than stove design, seems to be the main determinant of NO emissions.

As for the stove's heat output, it is essentially proportional to pyrolysis fuel usage for the particular stove tested. A different stove design could achieve a different constant of proportionality between these two quantities by improving heat transfer from the hot gases to the cooking pot. For example, surrounding the pot with a sleeve will increase heat transfer by directing hot gases along the sides of the cooking pot. Also, optimizing the choice of spacing between the stove and pot can increase the heat transfer to the water by changing the gas flow characteristics and temperatures. Such design changes would improve efficiency.

Most users desire cookstoves that cook quickly and efficiently, with as little fuel expense as possible. On the other hand, the primary goal of the research community is to reduce emissions, improving household indoor air and reducing environmental pollution. Our investigation indicates tradeoffs among the various desired cookstove characteristics. However, it also points to the possibility of addressing some of those tradeoffs through design improvements.

Acknowledgments

This work has been financially supported by the EPA-P3 People, Prosperity and the Planet (P3) Student Grant (83554801), NSF-BREAD (IOS-0965336), the National Natural Science Foundation of China (51406147), and the State Scholarship Fund of China Scholarship Council. The authors thank Mr. Philip Wong, Mr. Sungwon Yun, and Mr. Akio Enders.

References

- Anenberg SC, Balakrishnan K, Jetter J, Masera O, Mehta S, Moss J and Ramanathan V. (2013) Cleaner cooking solutions to achieve health, climate, and economic cobenefits. *Environ. Sci. Technol.* **47**, 3944–3952. doi:10.1021/es304942e.
- ASTM. (2004) ASTM E711 - 87 Standard test method for gross calorific value of refuse-derived fuel by the bomb calorimeter., ASTM International, West Conshohocken, PA.
- ASTM. (2013) ASTM Standard Method D5865-13 Standard test method for gross calorific value of coal and coke. ASTM International, West Conshohocken, PA.
- Ballard-Tremere G. and Jawurek H. H. (1996) Comparison of five rural, wood-burning cooking devices: Efficiencies and emissions. *Biomass Bioenergy* **11**, 419–430.
- Ballard-Tremere G. and Jawurek H. H. (1999) The “hood method” of measuring emissions of rural cooking devices. *Biomass Bioenergy* **16**, 341–345.
- Bhattacharya S. C., Albina D. O. and Khaing A. M. (2002) Effects of selected parameters on performance and emission of biomass-fired cookstoves. *Biomass Bioenergy* **23**, 387–395.
- Bonjour S., Adair-Rohani H., Wolf J., Bruce N. G., Mehta S., Prüss-Ustün A., Lahiff M., Rehfuess E. A., Mishra V. and Smith K. R. (2013) Solid fuel use for household cooking: country and regional estimates for 1980-2010. *Environ. Health Perspect.* **121**, 784–790.
- Clark ML, Peel JL, Balakrishnan K, Breyse PN, Chillrud SN, Naeher LP, Rodes CE, Vette AF and Balbus JM. (2013) Health and household air pollution from solid fuel use: The need for improved exposure assessment. *Environ Health Perspect.* **121**, 1120. doi:<http://dx.doi.org.proxy.library.cornell.edu/10.1289/ehp.1206429>.
- Crutzen P. J. and Andreae M. O. (1990) Biomass burning in the tropics: impact on atmospheric chemistry and biogeochemical cycles. *Science* **250**, 1669–1678.
- DeFoort M., L'Orange C., Lorenz N., Kamping W. and Alders J. (2010) Stove manufacturer's emissions and performance test protocol (EPTP)., Engines and Energy Conversion Laboratory; Fort Collins. Available at: <http://cleancookstoves.org/technology-and-fuels/testing/protocols.html> [Accessed June 19, 2016].
- Deng L., Torres-Rojas D., Burford M., Whitlow T. H., Lehmann J. and Fisher E. M. (2018) Fuel sensitivity of biomass cookstove performance. *Appl. Energy* **215**, 13–20.
- Flagan, Richard C and Seinfeld, John H. (1988) Pollution formation and control in combustion. In *Fundamentals of air pollution engineering* Prentice-Hall, Inc., Englewood Cliffs, NJ. pp. 167–255.
- Glarborg P., Jensen A. D. and Johnsson J. E. (2003) Fuel nitrogen conversion in solid fuel fired systems. *Prog. Energy Combust. Sci.* **29**, 89–113.

- Granier C, Müller J-F and Brasseur G. (2000) The impact of biomass burning on the global budget of ozone and ozone precursors. *Biomass Burn. Its Inter-Relatsh. Clim. Syst.*, Springer, Dordrecht; p. 69–85. doi:10.1007/0-306-47959-1_5.
- Holloway T., Levy H. and Kasibhatla P. (2000) Global distribution of carbon monoxide. *J. Geophys. Res. Atmospheres* **105**, 12123–12147.
- Jetter J. (2013) Update on EPA Stove Testing, Focus on Batch-Fueled Stoves. Available at: https://cfpub.epa.gov/si/si_public_record_report.cfm?dirEntryId=307494 [Accessed June 19, 2016].
- Jetter J, Zhao Y, Smith KR, Khan B, Yelverton T, DeCarlo P and Hays MD. (2012) Pollutant emissions and energy efficiency under controlled conditions for household biomass cookstoves and implications for metrics useful in setting international test standards. *Environ. Sci. Technol.* **46**, 10827–10834. doi:10.1021/es301693f.
- Kituyi E., Marufu L., Wandiga S. O., Jumba I. O., Andreae M. O. and Helas G. (2001) Carbon monoxide and nitric oxide from biofuel fires in Kenya. *Energy Convers. Manag.* **42**, 1517–1542.
- Koppmann R., von Czapiewski K. and Reid J. S. (2005) A review of biomass burning emissions, part I: gaseous emissions of carbon monoxide, methane, volatile organic compounds, and nitrogen containing compounds. *Atmos. Chem. Phys. Discuss.* **5**, 10455–10516.
- Lamberg H, Sippula O, Tissari J, Virén A, Kaivosoja T, Aarinen A, Salminen V and Jokiniemi J. (2017) Operation and emissions of a hybrid stove fueled by pellets and log wood. *Energy Fuels.* **31**, 1961–1968. doi:10.1021/acs.energyfuels.6b02717.
- Lehmann J. (2007) Bio-energy in the black. *Front. Ecol. Environ.* **5**, 381–387.
- Lim S. S., Vos T., Flaxman A. D., Danaei G., Shibuya K., Adair-Rohani H., AlMazroa M. A., Amann M., Anderson H. R., Andrews K. G., Aryee M., Atkinson C., Bacchus L. J., Bahalim A. N., Balakrishnan K., Balmes J., Barker-Collo S., Baxter A., Bell M. L., Blore J. D., Blyth F., Bonner C., Borges G., Bourne R., Boussinesq M., Brauer M., Brooks P., Bruce N. G., Brunekreef B., Bryan-Hancock C., Bucello C., Buchbinder R., Bull F., Burnett R. T., Byers T. E., Calabria B., Carapetis J., Carnahan E., Chafe Z., Charlson F., Chen H., Chen J. S., Cheng A. T.-A., Child J. C., Cohen A., Colson K. E., Cowie B. C., Darby S., Darling S., Davis A., Degenhardt L., Dentener F., Des Jarlais D. C., Devries K., Dherani M., Ding E. L., Dorsey E. R., Driscoll T., Edmond K., Ali S. E., Engell R. E., Erwin P. J., Fahimi S., Falder G., Farzadfar F., Ferrari A., Finucane M. M., Flaxman S., Fowkes F. G. R., Freedman G., Freeman M. K., Gakidou E., Ghosh S., Giovannucci E., Gmel G., Graham K., Grainger R., Grant B., Gunnell D., Gutierrez H. R., Hall W., Hoek H. W., Hogan A., Hosgood H. D., Hoy D., Hu H., Hubbell B. J., Hutchings S. J., Ibeanusi S. E., Jacklyn G. L., Jasrasaria R., Jonas J. B., Kan H., Kanis J. A., Kassebaum N., Kawakami N., Khang Y.-H., Khatibzadeh S., Khoo J.-P., Kok C., Laden F., Lalloo R., Lan Q., Lathlean T., Leasher J. L., Leigh J., Li Y., Lin J. K., Lipshultz S. E., London S., Lozano R., Lu Y., Mak J., Malekzadeh R., Mallinger L., Marcenes W., March L., Marks R., Martin R., McGale P., McGrath J., Mehta S., Memish Z. A., Mensah G. A., Merriman

- T. R., Micha R., Michaud C., Mishra V., Hanafiah K. M., Mokdad A. A., Morawska L., Mozaffarian D., Murphy T., Naghavi M., Neal B., Nelson P. K., Nolla J. M., Norman R., Olives C., Omer S. B., Orchard J., Osborne R., Ostro B., Page A., Pandey K. D., Parry C. D., Passmore E., Patra J., Pearce N., Pelizzari P. M., Petzold M., Phillips M. R., Pope D., Pope C. A., Powles J., Rao M., Razavi H., Rehfuess E. A., Rehm J. T., Ritz B., Rivara F. P., Roberts T., Robinson C., Rodriguez-Portales J. A., Romieu I., Room R., Rosenfeld L. C., Roy A., Rushton L., Salomon J. A., Sampson U., Sanchez-Riera L., Sanman E., Sapkota A., Seedat S., Shi P., Shield K., Shivakoti R., Singh G. M., Sleet D. A., Smith E., Smith K. R., Stapelberg N. J., Steenland K., Stöckl H., Stovner L. J., Straif K., Straney L., Thurston G. D., Tran J. H., Van Dingenen R., van Donkelaar A., Veerman J. L., Vijayakumar L., Weintraub R., Weissman M. M., White R. A., Whiteford H., Wiersma S. T., Wilkinson J. D., Williams H. C., Williams W., Wilson N., Woolf A. D., Yip P., Zielinski J. M., Lopez A. D., Murray C. J. and Ezzati M. (2012) A comparative risk assessment of burden of disease and injury attributable to 67 risk factors and risk factor clusters in 21 regions, 1990–2010: a systematic analysis for the Global Burden of Disease Study 2010. *Lancet* **380**, 2224–2260.
- Ludwig J, Marufu LT, Huber B, Andreae MO and Helas G. (2003) Domestic combustion of biomass fuels in developing countries: A major source of atmospheric pollutants. *J Atmos. Chem.* **44**, 23–37. doi:10.1023/A:1022159910667.
- MacCarty N., Ogle D., Still D., Bond T. and Roden C. (2008) A laboratory comparison of the global warming impact of five major types of biomass cooking stoves. *Energy Sustain. Dev.* **12**, 56–65.
- Marufu L., Dentener F., Lelieveld J., Andreae M. O. and Helas G. (2000) Photochemistry of the African troposphere: Influence of biomass-burning emissions. *J. Geophys. Res. Atmospheres* **105**, 14513–14530.
- Ndiema C. K. W., Mpendazoe F. M. and Williams A. (1998) Emission of pollutants from a biomass stove. *Energy Convers. Manag.* **39**, 1357–1367.
- Nielsen I. E., Eriksson A. C., Lindgren R., Martinsson J., Nyström R., Nordin E. Z., Sadiktsis I., Boman C., Nøjgaard J. K. and Pagels J. (2017) Time-resolved analysis of particle emissions from residential biomass combustion – Emissions of refractory black carbon, PAHs and organic tracers. *Atmos. Environ.* **165**, 179–190.
- Partnership for Clean Indoor Air. (2013) Water Boiling Test (WBT) Version 4.2.2.
- Putti VR, Tsan M, Mehta S, Kammila S. The state of the global clean and improved cooking sector. Washington, D.C.: World Bank; 2015.
- Roden C. A., Bond T. C., Conway S., Osorto Pinel A. B., MacCarty N. and Still D. (2009) Laboratory and field investigations of particulate and carbon monoxide emissions from traditional and improved cookstoves. *Atmos. Environ.* **43**, 1170–1181.
- Roth C. (2013) Micro-gasification: cooking with gas from dry biomass; An introduction to concepts and applications of wood-gas burning technologies for cooking. Deutsche

Gesellschaft für Internationale Zusammenarbeit (GIZ) GmbH Programme, Poverty-oriented Basic Energy Services (HERA).

Roy M. M. and Corscadden K. W. (2012) An experimental study of combustion and emissions of biomass briquettes in a domestic wood stove. *Appl. Energy* **99**, 206–212.

SAS Institute (2015) *JMP Pro.*, SAS Institute Inc, Cary, N.C.

Smith K. R., Bruce N., Balakrishnan K., Adair-Rohani H., Balmes J., Chafe Z., Dherani M., Hosgood H. D., Mehta S., Pope D., Rehfuess E. and HAP CRA Risk Expert Group (2014) Millions dead: how do we know and what does it mean? Methods used in the comparative risk assessment of household air pollution. *Annu. Rev. Public Health* **35**, 185–206.

Taylor R. (2009) The uses of laboratory testing of biomass cookstoves and the shortcomings of the dominant U.S. protocol. *Grad. Theses Diss.* Available at: <http://lib.dr.iastate.edu/etd/10550>.

Torres-Rojas D., Lehmann J., Hobbs P., Joseph S. and Neufeldt H. (2011) Biomass availability, energy consumption and biochar production in rural households of Western Kenya. *Biomass Bioenergy* **35**, 3537–3546.

Tryner J, Tillotson JW, Baumgardner ME, Mohr JT, DeFoort MW and Marchese AJ. (2016) The effects of air flow rates, secondary air inlet geometry, fuel type, and operating mode on the performance of gasifier cookstoves. *Environ. Sci. Technol.* **50**, 9754–9763. doi:10.1021/acs.est.6b00440.

Tryner J., Willson B. D. and Marchese A. J. (2014) The effects of fuel type and stove design on emissions and efficiency of natural-draft semi-gasifier biomass cookstoves. *Energy Sustain. Dev.* **23**, 99–109.

Venkataraman C., Joshi P., Sethi V., Kohli S. and Ravi M. (2004) Aerosol and carbon monoxide emissions from low-temperature combustion in a sawdust packed-bed stove. Available at: <http://dspace.library.iitb.ac.in/xmlui/handle/10054/12388> [Accessed December 29, 2017].

Venkataraman G and Rao GUM. (2001) Emission factors of carbon monoxide and size-resolved aerosols from biofuel combustion. *Environ. Sci. Technol.* **35**, 2100–2107. doi:10.1021/es001603d.

Winter F., Wartha C. and Hofbauer H. (1999) NO and N₂O formation during the combustion of wood, straw, malt waste and peat. *Bioresour. Technol.* **70**, 39–49.

Yuntenwi E. A. T., MacCarty N., Still D. and Ertel J. (2008) Laboratory study of the effects of moisture content on heat transfer and combustion efficiency of three biomass cook stoves. *Energy Sustain. Dev.* **12**, 66–77.

- Zhang H., Ye X., Cheng T., Chen J., Yang X., Wang L. and Zhang R. (2008) A laboratory study of agricultural crop residue combustion in China: Emission factors and emission inventory. *Atmos. Environ.* **42**, 8432–8441.
- Zhang J., Smith K. R., Uma R., Ma Y., Kishore V. V. N., Lata K., Khalil M. A. K., Rasmussen R. A. and Thorneloe S. T. (1999) Carbon monoxide from cookstoves in developing countries: 1. Emission factors. *Chemosphere - Glob. Change Sci.* **1**, 353–366.
- Zube D. J. (2010) Heat transfer efficiency of biomass cookstoves. Thesis, Colorado State University. Libraries. Available at: <https://dspace.library.colostate.edu:443/handle/10217/39344> [Accessed June 19, 2016].

CHAPTER 3: THERMOCHEMICAL AND BIOLOGICAL TRANSFORMATION OF ORGANIC NITROGEN IN PLANT RESIDUES

Abstract

The molecular structure of PyOM is generally considered to exert a dominant control on PyOM-C mineralization, yet similar information is lacking for PyOM-N. In this study, we evaluated how the thermal conversion of organic matter (OM), into pyrogenic organic matter (PyOM), altered the N molecular structure and affected subsequent C and N mineralization. Nitrogen near edge X-ray absorption fine structure (NEXAFS) of uncharred OM, PyOM, PyOM toluene extract, and PyOM after extraction were used to predict PyOM-C and -N mineralization. PyOM was produced from five different feedstocks each with varying initial N content at three pyrolysis temperatures. Uncharred OM and PyOM were incubated in a sand matrix for 256 days at 30°C. As pyrolysis temperature increased from 350 to 700°C, aromatic C=N in six-membered rings increased threefold, aromatic C=N in six-membered rings with a keto group increased sevenfold, and quaternary N doubled. Initial OM-N content was positively correlated with the proportion of heterocyclic aromatic N in PyOM ($R^2=0.44$; $p < 0.0001$; $n=42$). A 55% increase of aromatic N heterocycles at high N content when compared to low OM-N content suggests that higher concentration of N favor the insertion of N atoms into aromatic structures by overcoming the energy barrier to break C bonds. A ten-fold increase of aromatic C=N in 6-membered ring (putative) in PyOM decreased C mineralization by 87%, whereas total N contents and C:N ratios had no effects on C mineralization ($R^2=0.14$; $p<0.11$; $n=20$). Oxidized aromatic N in PyOM extracts favored C mineralization, while aromatic N in 6-membered heterocycles reduced mineralization ($R^2=0.56$; $p=0.001$; $n=100$). Similarly, aromatic N in 6-membered heterocycles

in the remaining PyOM after extraction reduced PyOM-C mineralization ($R^2=0.49$; $p=0.0006$; $n=100$). PyOM-C mineralization increases when N atoms are located at the edge of the C network or when more N is found in the PyOM extract and are more accessible to microbial oxidation. These results confirm the hypothesis that the molecular structure of N in different fractions of PyOM play a major role in PyOM-C persistence.

Keywords: Pyrogenic organic matter, N content, XANES, aromatic N heterocycles, PyOM-C stability

1. Introduction

Carbon (C) and nitrogen (N) constitute a significant and important fraction of pyrogenic organic matter (PyOM) that form part of the global C and N cycles (Schmidt and Noack, 2000; Preston and Schmidt, 2006; Hilscher and Knicker, 2011). PyOM in terrestrial ecosystems originates from the burning of vegetation during natural or deliberate fires and is by now recognized as an important pool of terrestrial pyrogenic C (PyC) with global distribution (Bird et al., 2015; Santín et al., 2016). Natural PyOM forms a continuum from slightly charred to highly transformed OM, described as clusters of polyaromatic rings with a high degree of N, O and S substitution (Knicker, 2010). The composition and structure of PyOM are one of the main drivers for the persistence of PyOM-C in the environment (Bird et al., 2015). Considerable research has been conducted to understand the thermochemical changes of OM-C during thermal degradation (Czimczik et al., 2002; Keiluweit et al., 2010; Heymann et al., 2011; Wiedemeier et al., 2015) and its relationship to PyOM-C mineralization (Baldock and Smernik, 2002; Nguyen et al., 2010). N in PyOM and how it is related to the persistence of PyOM-C has received much less attention.

During thermal degradation, the degree of aromaticity and condensation of PyOM-C increases (McBeath et al., 2011; McBeath et al., 2015; Wiedemeier et al., 2015). Likewise, N in organic matter (OM-N) is structurally altered and incorporated into the aromatic structure of PyOM as thermal degradation proceeds to form aromatic N heterocycles in PyOM-N (Knicker et al., 1996; Almendros et al., 2003; Knicker, 2007; Hilscher et al., 2009; Chen et al., 2014). It is unclear how the initial N content of OM influences the formation of the N-aromatic structures in PyOM. Several authors have identified mechanisms by which aromatic N heterocycles form. (Stańczyk et al., 1995) and (Almendros et al., 2003) observed increasing N content when the N

precursor was an aromatic ring structure. They suggest that aromatic N structures are thermally stable when compared to non-aromatic N structures. The authors also propose the formation of new aromatic N structures during thermal degradation, but do not report on the effects of N amounts on any pathways of N incorporation into PyOM. Additionally a few studies (dos Santos and Alvarez, 1998; Chen et al., 2010) have reported that the formation of aromatic N structures in N doped carbon nanotubes are affected by the initial N content of the precursor. They suggest that there is a relationship between the N content of the precursor and the energy barrier for the formation of different N moieties. Based on these findings, we suggest that with low OM-N contents, non-aromatic N structures will be preferentially formed, however, as N content increases, a greater proportion of aromatic N structures form. Whether lower N contents in original OM generate PyOM with higher non-aromatic N structures has therefore not been directly shown.

In the last decade, several studies have shown evidence for the persistence of PyOM in soils (Lehmann et al., 2015; Wang et al., 2016). The extent of its mineralization depends on the thermal degradation temperature and the resulting composition and structure of PyOM-C, particularly the degree of aromatic condensation (McBeath et al., 2011; Singh et al., 2012; Wiedemeier et al., 2015). However, PyOM is a heterogeneous material which includes various forms of aromatic C structures. While the connection between persistence and C composition of PyOM-C has been extensively studied, there is less understanding about PyOM-N and its effect on mineralization of PyOM-C. Similar to PyOM-C, the aromatic N structures in PyOM vary widely with degree of thermal degradation (Knicker, 2007) and may therefore affect the mineralization of PyOM-C. For uncharred OM, N contents and C:N ratios are known to exert considerable control over C mineralization (Melillo et al., 1982). While the quantitative

relationship between N forms in plant residues (e.g., lignin:N ratios) and C decomposition is well studied (Fox et al., 1990), it is not known how changes in N molecular forms in PyOM as a function of different N contents in uncharred OM under different intensity of charring may affect the mineralization of PyOM-C structures.

PyOM also contains a weakly aromatic or non-aromatic C fraction that is much more susceptible to microbial degradation (Whitman et al., 2014). Similarly, several studies (Hilscher et al., 2009; Hilscher and Knicker, 2011; de la Rosa and Knicker, 2011; Wang et al., 2012) have shown evidence for biological degradation of PyOM-N. According to these studies, a considerable fraction of the mineralizable N is amide N, which resisted thermal degradation in vegetation fires. These authors show how a proportion of heterocyclic N is decomposed to amide N or mineral N. These results suggest that a fraction of the PyOM-N is not poly-aromatic and therefore easily mineralizable. This fraction may also have a direct impact on the mineralization of the associated PyOM-C. However, it is not clear which fraction of PyOM-N is biologically available, what proportion it constitutes as a result of different N contents in the uncharred OM, and whether and in what way these non-aromatic PyOM-N amounts and forms affect the mineralization of PyOM-C.

Therefore, this study focuses on the structural changes of N in OM during thermal degradation as a function of the initial N concentration and its subsequent effect on the biological degradation of PyOM-C. The objectives were (1) to determine the effects of varying N contents of OM and increasing charring temperature on the functional group composition of PyOM-N; and (2) to evaluate how the content and molecular structure of N in PyOM affects the mineralization of PyOM-C. We hypothesized that (i) higher N concentrations in OM decreases

the formation of aromatic N heterocycles in PyOM; and (ii) higher N concentrations in easily mineralizable PyOM increases C mineralization.

2. Materials and Methods

2.1. Plant residues and PyOM production

For this study we used organic matter from plant residues (OM) of corn- *Zea mays* L.; ryegrass- *Lolium perenne* L.; and willow- *Salix viminalis* L. with varying N content (see Appendix Section B1.1). Leaves, stalks and woody residues were separated, to obtain plant tissue with different N concentration. Plant residues were dried at 60°C to a constant mass and ground to ≤ 2 mm. Approximately 15 g of plant residue were placed in a custom-built batch reactor and purged under Ar gas. The plant residue was heated at a rate of 2.5°C min⁻¹ and allowed to remain for 30 min at the highest heat temperatures (HHT) of 350, 500 and 700°C. The reactor cooled down to 25°C at a rate of 5°C min⁻¹. The resulting PyOM was ground and sieved to obtain two particle sizes <74µm, used for all analyses and 74-150 µm, used for experiments.

We measured total C and N for OM and PyOM (<74µm) (Appendix Table 1) on an NC2500 (Carlo Erba, Italy) elemental analyzer coupled to a Delta V Isotope Ratio Mass Spectrometer (Thermo Scientific, Germany). The inorganic N contents for OM and PyOM were measured by mixing 0.5 g sample with 30 mL of 1M KCl and shaking for one hour. The KCl extract was filtered through a Whatman No. 42 filter paper. The concentrations of ammonium (NH₄⁺) and nitrate (NO₃⁻) in solution were determined by continuous flow analysis (Bran and Luebbe Autoanalyzer, SPX, Charlotte, NC, USA). PyOM pH was measured in DI water at a ratio of 1:20 g mL⁻¹ using a glass electrode (Orion 3-Star pH Benchtop; Thermo Electron Corporation, Beverly, MA, USA) (Appendix Table B.2).

2.2. PyOM fractionation and extraction

PyOM was extracted using toluene to generate a residual PyOM after extraction and a PyOM extract. PyOM after extraction represents the toluene-insoluble solid material remaining after the extraction, while the PyOM extract represents compounds that are likely re-condensed on PyOM surfaces and pores after pyrolysis. PyOM was extracted with toluene, (HPLC grade; Sigma-Aldrich, USA) in a Soxhlet apparatus (Jonker and Koelmans, 2002). This fraction of PyOM is considered the toluene-extractable fraction produced during pyrolysis. A subsample of 100 mg of PyOM (74-150 μm), was weighed into a glass extraction thimble with fritted disc (Wilma Lab Glass, Vineland, NJ, USA), treated with 70 mL of toluene, which recirculated through the apparatus for 2 hours. The PyOM toluene extract was cooled down and filtered with Whatman no. 42 paper (Whatman International Ltd, England). The extract was further concentrated using a rotary evaporator (Rotavapor R-134, Büchi Labortechnik AG, Switzerland). PyOM after extraction was dried at 70°C to constant weight. Both materials were stored for further analysis.

2.3. NEXAFS

The chemical speciation of OM, PyOM, PyOM after extraction (74-150 μm) and the PyOM toluene extract was obtained using N (1s) K near edge X-ray adsorption fine structure (NEXAFS) spectroscopy. Samples (see Appendix B Section 1.2 for sample preparation) were mounted on Au coated Si wafer and spectra were acquired using the slew scanning mode on the 11ID-1 spherical grating monochromator (SGM) beamline at the Canadian Light Source (CLS, Saskatoon, Saskatchewan, Canada). The beamline is capable of providing 10^{11} photons s^{-1} at the N K-edge with a resolving power ($E/\Delta E$) better than 10000 (Regier et al., 2007a; Regier et al., 2007b). Solid samples were scanned 10 times at different locations on the sample. Due to the

lower N concentration of the PyOM toluene extract than the other materials, 20 scans were taken at separate locations in the sample. Each scan took 20s and beam spot size was 1000 μm by 100 μm (Regier et al., 2007a; Regier et al., 2007b). The exit slit gap was set at 25 μm and the photon energy was scanned from 390 to 420 eV. Total electron (TEY) and fluorescence yield (FLY) data were collected simultaneously at 250 mA and beam intensity of 2.9 GeV using a two-stage microchannel plate detector. Beam line flux (I_0) was measured with an in-line silicon photodiode (Gillespie et al., 2014b). The photon energy was calibrated to the $\text{N } 1s \rightarrow \pi^*$ transition for N_2 gas at 400.8 eV using ammonium sulfate (Gillespie et al., 2008).

Nitrogen spectra were processed using IGOR Pro (Wavemetrics, Oregon, USA) and Athena (Ravel and Newville, 2005), software packages. The incident beam intensity (I_0) and sample measurements were scaled and offset using customized macros in IGOR Pro (Gillespie et al., 2014a; Gillespie et al., 2014b). Normalized spectra were obtained by dividing the sample intensity by the I_0 . Data were averaged for a minimum of five scans and background corrected by a linear regression fit through the pre-edge and post-edge regions and normalized to an edge jump of 1.

The N K-edge of all sample spectra were deconvoluted using a non-linear least square fitting method. Deconvolution was performed using an arctangent function to model the edge step and fixed at 404 eV. Spectral features were resolved using a series of Gaussian peaks representing the main $\text{N } 1s \rightarrow \pi^*/1s \rightarrow \sigma^*$ transitions (Fityk 0.9.8, Wojdyr, 2010) (see Appendix Figure B.1-2 and Appendix Table B.3 for N standard spectra and peak position and Appendix Table B.4 for peak assignments used in deconvolution). The proportion of the $1s \rightarrow \pi^*$ area for N bonds was calculated for each sample (Appendix Tables B.5-9).

2.4. OM and PyOM incubations

Incubation experiments were used to determine the C and N mineralization of OM and PyOM. For C mineralization, a mixture of 200 mg of OM or PyOM (74-150 μm) and 15 g of quartz sand (Sigma Aldrich no. 274739, 50 + 70 mesh) were mixed and added to 60-ml jars. For each OM or PyOM-sand mixture the water holding capacity (WHC) was determined gravimetrically (Haney and Haney, 2010). CO_2 -free water and microbial inoculum (Appendix B Section 1.3) were added to each sample jar to achieve 55% WHC. Individual sample jars were placed inside a 473-mL Mason jar with a vial containing 15 mL of 0.09 KOH. CO_2 -free deionized water (5 mL) was added to the bottom of the jar to keep the environment moist (Whitman et al., 2014). Four replicates were established for each treatment, and four blanks with no OM or PyOM additions were also established and incubated at 30°C. CO_2 trapped in the KOH solution during the incubation was quantified by measuring the electrical conductivity (EC) of the solution. Due to differences in CO_2 respiration rates between OM and PyOM, EC measurements were staggered during the incubation. New KOH traps were placed in the Mason jars and 5 mL of fresh CO_2 -free DIW were added to the bottom of the jar and returned to the incubation chamber. The total duration of the incubation was 252 days. Total C mineralized was determined by correlating the measured EC to a known volume of CO_2 , using a calibration curve (Woo et al., 2016).

Nitrogen mineralization was determined by measuring the amount of available mineral N at the beginning and end of the incubation period. For each treatment, a sample of 200 mg of OM or PyOM (74-150 μm) was mixed with 15 g of quartz sand (550°C for 2 hrs) and placed in 60-mL sample jars. The blank treatment was sand without OM or PyOM. Nutrient solution and

microbial inoculum (2.16 mL) were added to each jar. Additional DIW was also added to bring each jar to 55% WHC. Sample jars were incubated at 30°C for a period of 50 days. Inorganic N ($\text{NH}_4\text{-N} + \text{NO}_3\text{-N}$) was determined by adding 2M KCl in a 1:2 w/v ratio at the end of the incubation period. Inorganic N at time 0 was determined by adding the 2M KCl to the sample jars, immediately after additions of nutrient solution and microbial inoculum. All sample-KCl mixtures were shaken for 1 h after which the supernatant was filtered (Whatman no. 42) and the filtrate analyzed for $\text{NH}_4\text{-N}$ and $\text{NO}_3\text{-N}$ on an autoanalyzer (Bran and Luebbe Autoanalyzer, SPX, Charlotte, NC, USA). Net N mineralized was determined as follows: $(\text{net N mineralized})_t = (\text{mineral N in sample} - \text{mineral N in control})_t$.

2.5. Statistical analysis

All statistical analyses were performed using JMP version 12.0.1 (SAS Institute, 2015). We used linear regressions models ($p \leq 0.05$) to fit the proportion of aromatic and non-aromatic N in PyOM with the N content of PyOM. We also fitted cumulative C mineralization for OM and PyOM to the C:N ratio using linear regression.

Multivariate regression analysis was used to determine the relationship between cumulative PyOM-C mineralized and ratios of N functional groups from the different fractions of PyOM as quantified by N K-edge XANES. Stepwise regression was performed to select the most significant of the independent variables for inclusion in multivariate linear models for the dependent variables. P value thresholds of 0.1 were used to allow an independent variable to enter the model, while 0.05 was used to allow an independent variable to be removed from the model. A mixed stopping rule was applied to allow the alternation of forward and backwards steps.

3. Results

3.1. Nitrogen and C content changes with temperature and initial N content

Total PyOM-N contents changed with both pyrolysis temperature and initial OM-N contents (Figure 3.1). At low OM-N contents, N concentrations of the OM increased by 29-98% when pyrolyzed at 350°C. For high OM-N the increase was 1-43%, much lower than at lower N contents. The N increase greatly depended on the type of OM and was up to four times as high in ligneous OM such as willow branches than its leaves, depending on the initial OM-N content. The increase in PyOM-N was evident up to a pyrolysis temperature of 350°C, above which PyOM-N decreased as pyrolysis temperature progresses to 700°C. The decrease in N content was similar for both low N –PyOM (26-77%) and high N-PyOM (25-63%) and was not affected by the type of original biomass residue. Despite this N enrichment of PyOM, its N contents was not significantly different from that of the original OM-N (Appendix Figure B.3).

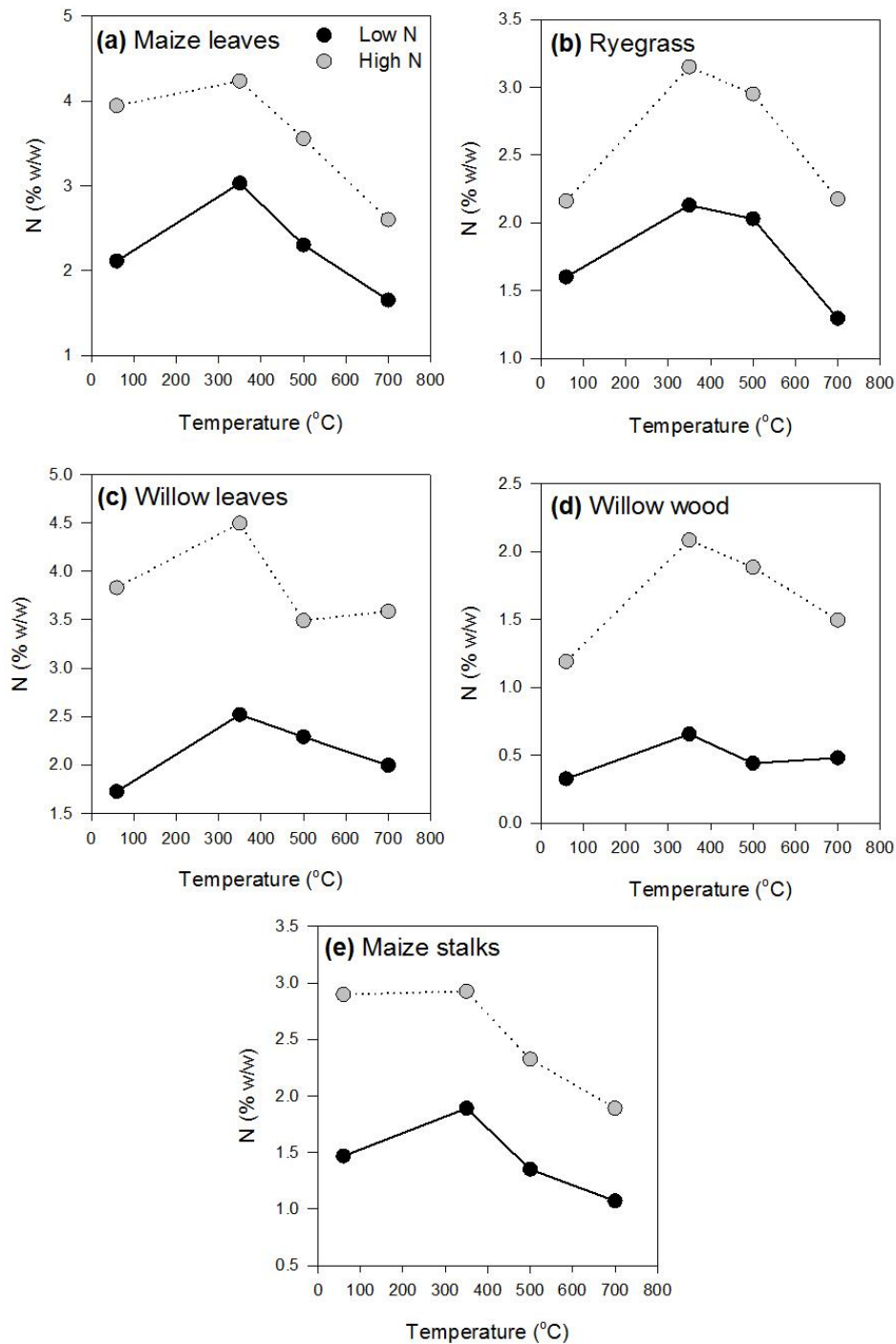


Figure 3. 1: Nitrogen contents of uncharred OM and PyOM as a function of pyrolysis temperature. Nitrogen contents as a function of temperature for uncharred OM and PyOM of (a) maize leaves, (b) ryegrass, (c) willow leaves, (d) willow wood and (e) maize stalks at three different pyrolysis temperatures. Grey circles and black circles represent high- and low-N content OM and PyOM, respectively.

3.2. NEXAFS characterization of OM, PyOM, PyOM after extraction and PyOM toluene extract

Nitrogen K-edge NEXAFS spectra of OM, PyOM, PyOM after extraction and the PyOM toluene extracts suggest that the initial OM-N content and thermal decomposition resulted in complex mixtures of N bonding environments for all the studied materials. Spectra of uncharred OM were characterized by two distinct features irrespective of the type of plant residue (Figure 3.2 and Appendix Figures B.4-7). A single narrow adsorption feature was present between 400.2 and 402.2 eV, with the peak center at 401.3 eV. Deconvolution of the spectra indicated this region corresponds to the delocalized pair of electrons from aromatic C-N of five-membered rings. Deconvolution values for this group were similar for all OM, accounting for 54-64% of the $1s \rightarrow \pi^*$ region (Appendix Tables B.5-9), while a broader adsorption band was present near 405.76 eV representing N-H bonds in the $1s \rightarrow \sigma^*$ transition.

Spectra of PyOM, however, showed a more complex N bonding environment, characterized by aromatic C=N in six-membered rings, between 398.1-399.4 eV for all PyOM. The main peak for maize leaves pyrolyzed at 350°C (py-350°C) was centered at 398.8 eV (Figure 3.2). As pyrolysis temperatures increased to 500°C, the aromatic C=N peak was resolved at 398.5 eV, while the same peak for PyOM heated to 700°C was centered at 398.3 eV. While the center of the main aromatic C=N peak for PyOM did not vary between the different types of OM (Appendix Figures B.4-7), this peak generally shifted by -0.2 eV to lower energy levels with increasing pyrolysis temperature. One noticeable exception were the ryegrass spectra; the main aromatic C=N peak center did not shift in energy position between 500°C and 700°C. For py-700°C, an additional peak was observed in the form of a shoulder at 397.9 eV. Spectral deconvolution revealed the aromatic C=N region included six-membered rings (containing either

one or two N atoms) and accounted for 9-35% of the $1s \rightarrow \pi^*$ region, depending on the type of OM (Appendix Tables B.5-9). Beyond the aromatic C=N region of six-membered rings, other absorption bands were resolved at 399.93 eV for aromatic C=N of five-membered rings. The spectra also show a broad shoulder at 400.5-403.95 eV. The main feature observed for uncharred OM at 401.4 eV disappeared for PyOM as thermal decomposition proceeded. The range of the shoulder suggests a mixture of bonding environments which were associated with quaternary-N, a delocalized pair of electrons from aromatic C-N from five-membered rings (containing either one or two N atoms) and exocyclic N bonded to aromatic C.

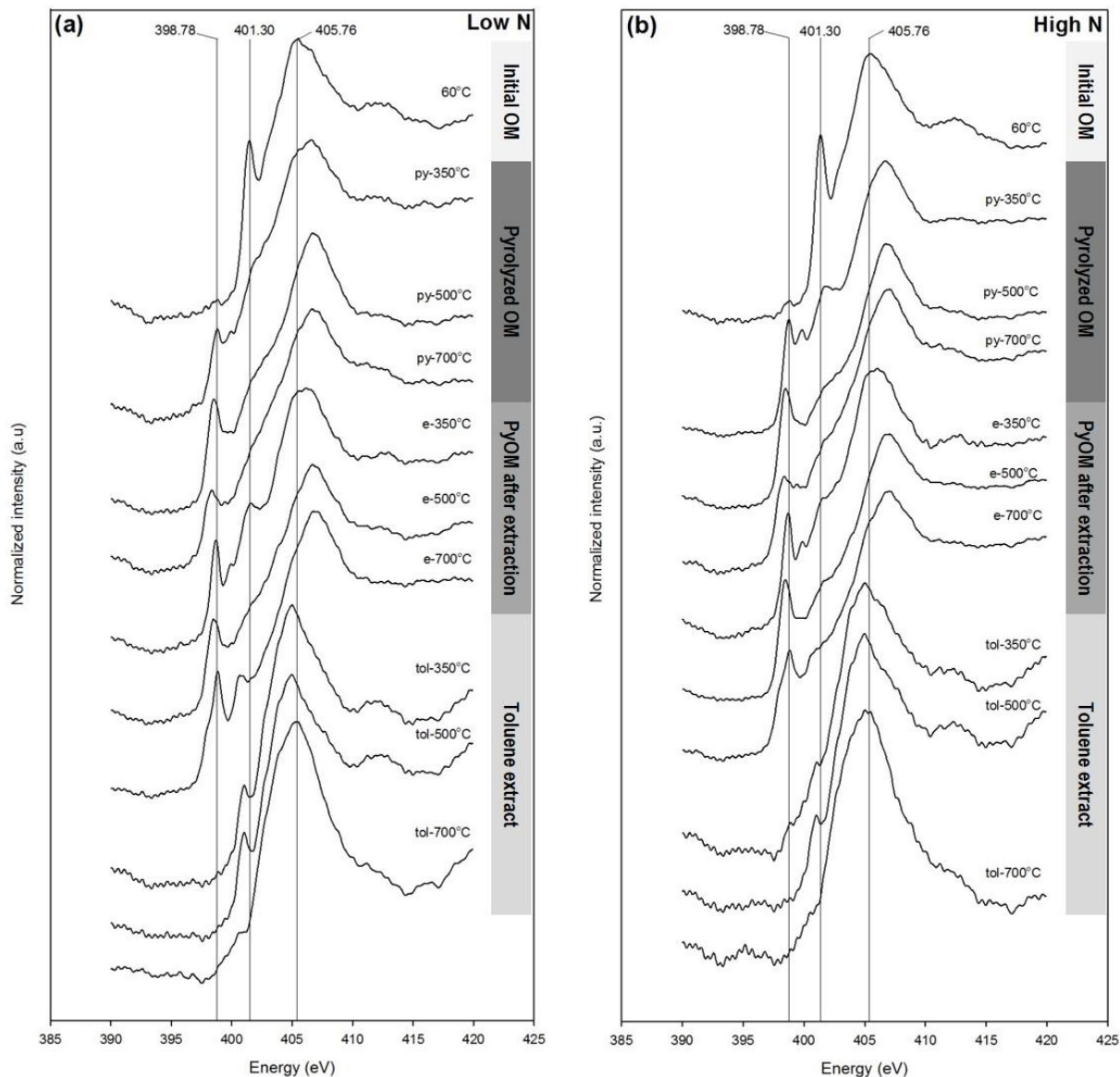


Figure 3.2: Nitrogen K-edge NEXAFS spectra of uncharred initial OM, entire PyOM (py-), extracted PyOM (e-), and the toluene extract of PyOM (tol-) as a function of pyrolysis temperature for maize leaves. (a) Low N-containing maize leaves, and (b) high N-containing maize leaves. Black lines represent the peak centers associated with selected key spectral features: 398.78 eV for C=N bonds in aromatic six-membered rings, 401.3 eV for C-N bonds in aromatic five-membered rings, and 405.76 eV for N-H bonds. Spectra of additional OM shown in Appendix Figures B.3-6.

The structure of PyOM after extraction revealed three resolved peaks near 398.78, 399.93 and 401.3 eV, corresponding to multiple $1s \rightarrow \pi^*$ bonding environments (Figure 3.2 and Appendix Figures B.4-7). These peaks represent bonding environments with aromatic C=N in six-membered rings (containing either one or two N atoms) and aromatic C-N in five-membered rings (containing two N atoms). For 3 out of the 5 types of OM residues an additional peak was resolved at approximately 400.5 eV with increasing absorption intensity at higher pyrolysis temperature, representing a bonding environment known for quaternary-N.

Spectra of PyOM toluene extracts suggest that this fraction had a different bonding environment than both PyOM and PyOM after extraction. The spectra were dominated by $1s \rightarrow \sigma^*$ features with peak centers between 405-406.1 eV (Figure 3.2 and Appendix Figures B.4-7). A second but much smaller feature in the $1s \rightarrow \pi^*$ region is resolved in the spectra between 400.74-401.3 eV. This second region represents a bonding environment which includes aromatic C-N in 6-membered oxygenated rings (containing two N atoms), non-aromatic C-N in 6-membered oxygenated rings and a delocalized pair of electrons from aromatic C-N in five-membered rings (containing two N atoms). Spectral deconvolution also showed a significant proportion of aliphatic C-NH₂ bonded to aromatic six-membered ring and C-NO₂ bonded to aromatic six-membered ring present in PyOM toluene extract (Appendix Tables B.5-9). The average spectral deconvolution values for aromatic C-N in six-membered oxygenated rings (containing two N atoms) (7%) and exocyclic N bonded to aromatic six-membered rings (28%) were significantly different (LSMeans contrast, $p < 0.0001$) for the PyOM toluene extract when compared to PyOM and PyOM after extraction (Appendix Tables B.5-9).

3.3. Temperature and N effects on PyOM-N

Pyrolysis temperature had a significant effect (LSMeans contrast, $p < 0.0001$) on the proportion of different N functional groups present in PyOM (Figure 3.3). As pyrolysis temperature increased from 350-700°C, aromatic C=N in six-membered rings putative (398.1 eV) increased threefold. Aromatic C=N in six-membered rings with a keto group increased sevenfold, while quaternary N (400.9 eV) doubled. In contrast, aromatic C=N in five and six-membered rings (containing one and two N atoms), aromatic C-N six-membered oxygenated rings, and aromatic C-N in five-membered rings (containing either one or two N atoms) decreased with increasing pyrolysis temperature by 50, 42 and 15%, respectively. Exocyclic N bonded to aromatic six-membered rings also increased by 18% with increasing pyrolysis temperature.

The initial OM-N contents had a significant and positive relationship with the proportion of total aromatic N heterocycles in PyOM (Figure 3.4a). On the other hand, N contents negatively correlated with quaternary N (Figure 3.4b) and exocyclic N bonded to aromatic six-membered rings (Figure 3.4c) in PyOM.

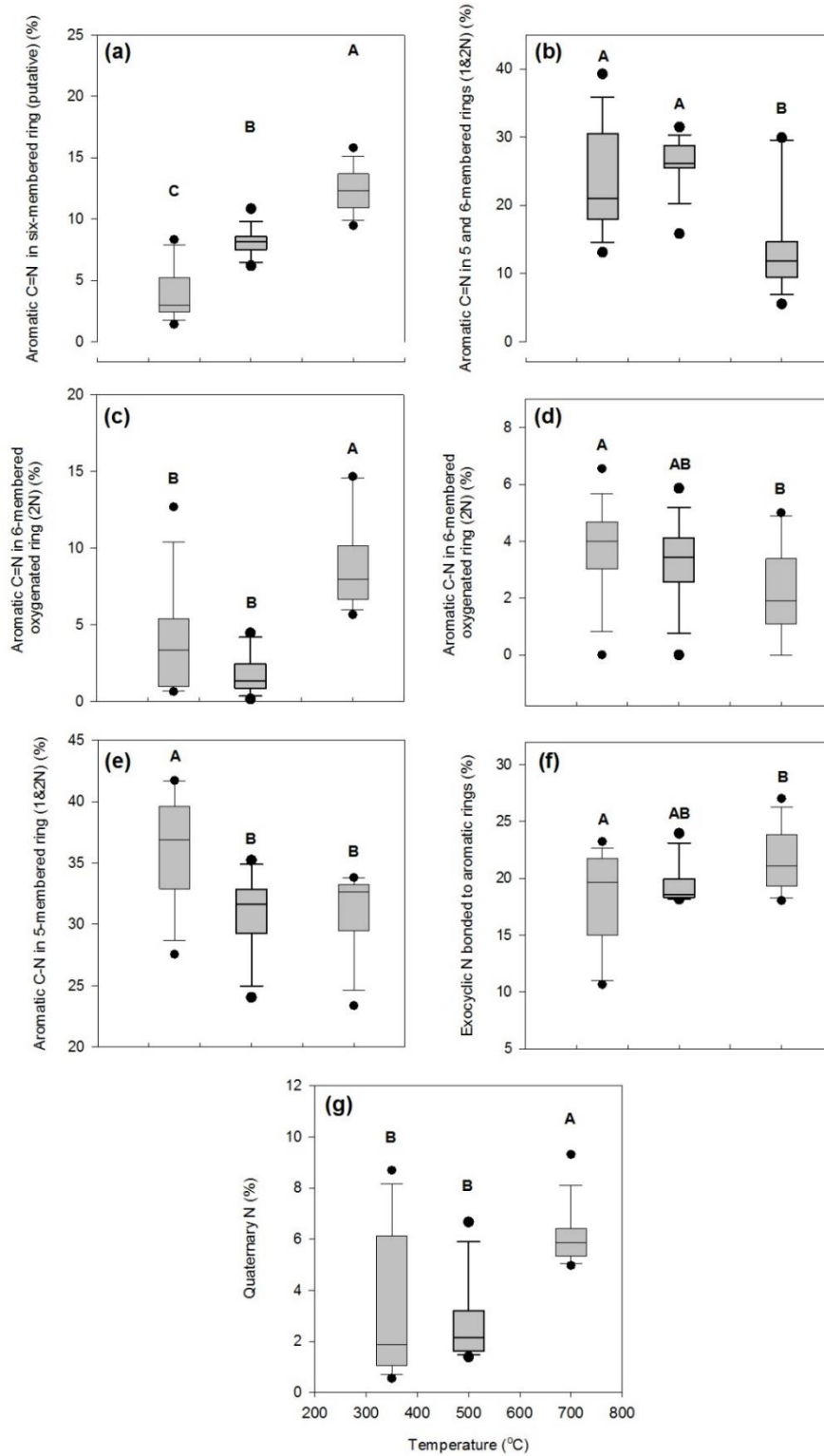


Figure 3.3: Proportion of aromatic nitrogen functional groups for PyOM at different pyrolysis temperatures and all types of biomass. (a) Aromatic C=N in 6-membered rings putative represents

the proportion of the total spectral absorption intensity corresponding to spectral features at 398.1 eV, (b) aromatic C=N in 5 and 6-membered rings containing 1 and 2N atoms, represents the proportion of the total absorption intensity of the sum of spectral features at 398.73 and 399.93 eV, (c) aromatic C=N in 6-membered oxygenated rings with represent the proportion of the total absorption intensity spectral feature at 399.4 eV (d) aromatic C-N in 6-membered oxygenated rings with represent the proportion of the total absorption intensity spectral feature at 400.74 eV, (e) aromatic C-N in 5-membered rings with delocalized pairs of electrons from aromatic N from 5-membered rings (containing one or two N atoms), represent the proportion of the total absorption intensity of the sum of spectral features at 401.3 and 402.13 eV, and (f) exocyclic N bonded to aromatic 6 membered rings represent the proportion of the total absorption intensity of the sum of spectral features at 403 and 403.61 eV and (g) quaternary N represent the proportion of the total absorption intensity spectral feature at 400.9 eV

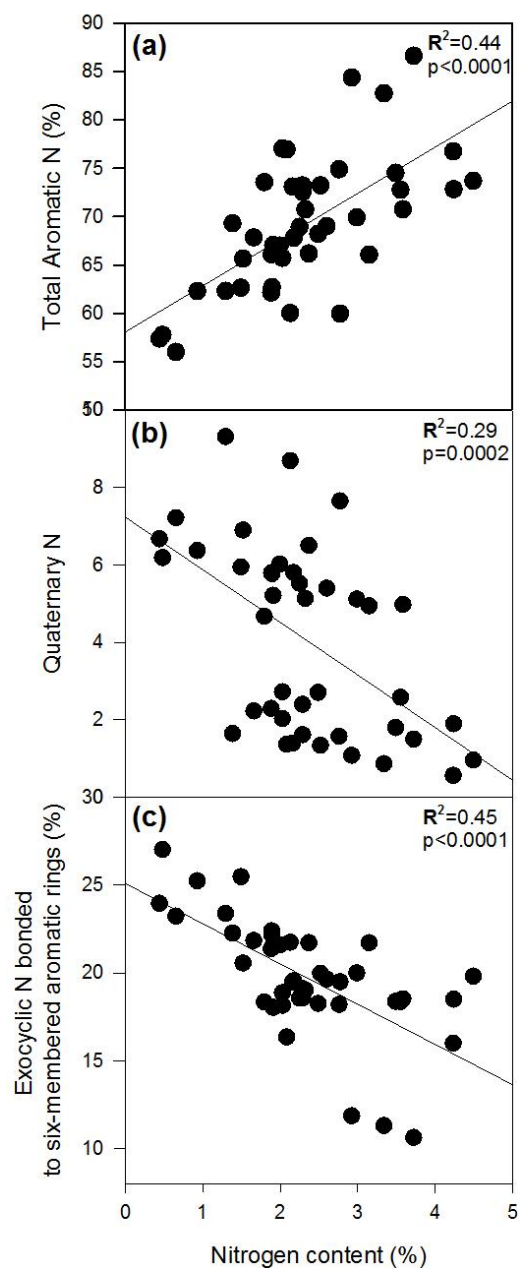


Figure 3.4: Effects of nitrogen contents on the formation of N functional groups. (a) Sum of all aromatic N heterocycles as a function of N contents in PyOM, (b) proportion of quaternary N in PyOM as a function of N contents, and (c) sum of all N exocyclic N attached to a 6-membered aromatic ring as a function of N contents in PyOM expressed as a proportion of the total absorption intensity (left y-axis). Plots are fitted with significant regression lines: *Total aromatic N* = $58.1 + 4.78x$, $R^2 = 0.44$, $p < 0.0001$; *Quaternary N* = $7.2 - 1.36x$, $R^2 = 0.29$, $p = 0.0002$; *Exocyclic N bonded to 6-membered aromatic rings* = $25.1 - 2.29x$, $R^2 = 0.43$, $p < 0.0001$.

3.4. C and N mineralization of OM and PyOM

Cumulative mineralization of OM-C was higher than that of PyOM-C (Figure 3.5a and Appendix Figures B.8a-11a). Cumulative PyOM-C mineralization throughout the 252 days of incubation was greater for py-350°C than for py-700°C (Figure 3.5b and Appendix Figures B.8b-11b). Total cumulative mineralization was highest for OM-C (999-1709 mg CO₂-C g⁻¹C) and lowest for py-700°C (5-125 mg CO₂-C g⁻¹C). Total cumulative C mineralization for OM-C was 10-43 times greater (LSMeans contrast, $p < 0.0001$) compared to PyOM-C. Total mineralization of PyOM-C decreased by 75% with an increase in pyrolysis temperatures from 350 to 700°C ($p=0.0003$).

The C:N ratios were significantly and negatively correlated to the OM-C mineralization (Figure 3.6). In contrast, PyOM-C mineralization was not correlated to the C:N ratio for both pyrolysis temperatures.

Mineral N contents were 13-78 times higher for all uncharred OM when compared to PyOM. For most of the types of OM net N mineralization occurred during the incubation. However, all PyOM samples showed net N immobilization during the incubation (Appendix Figure B.12).

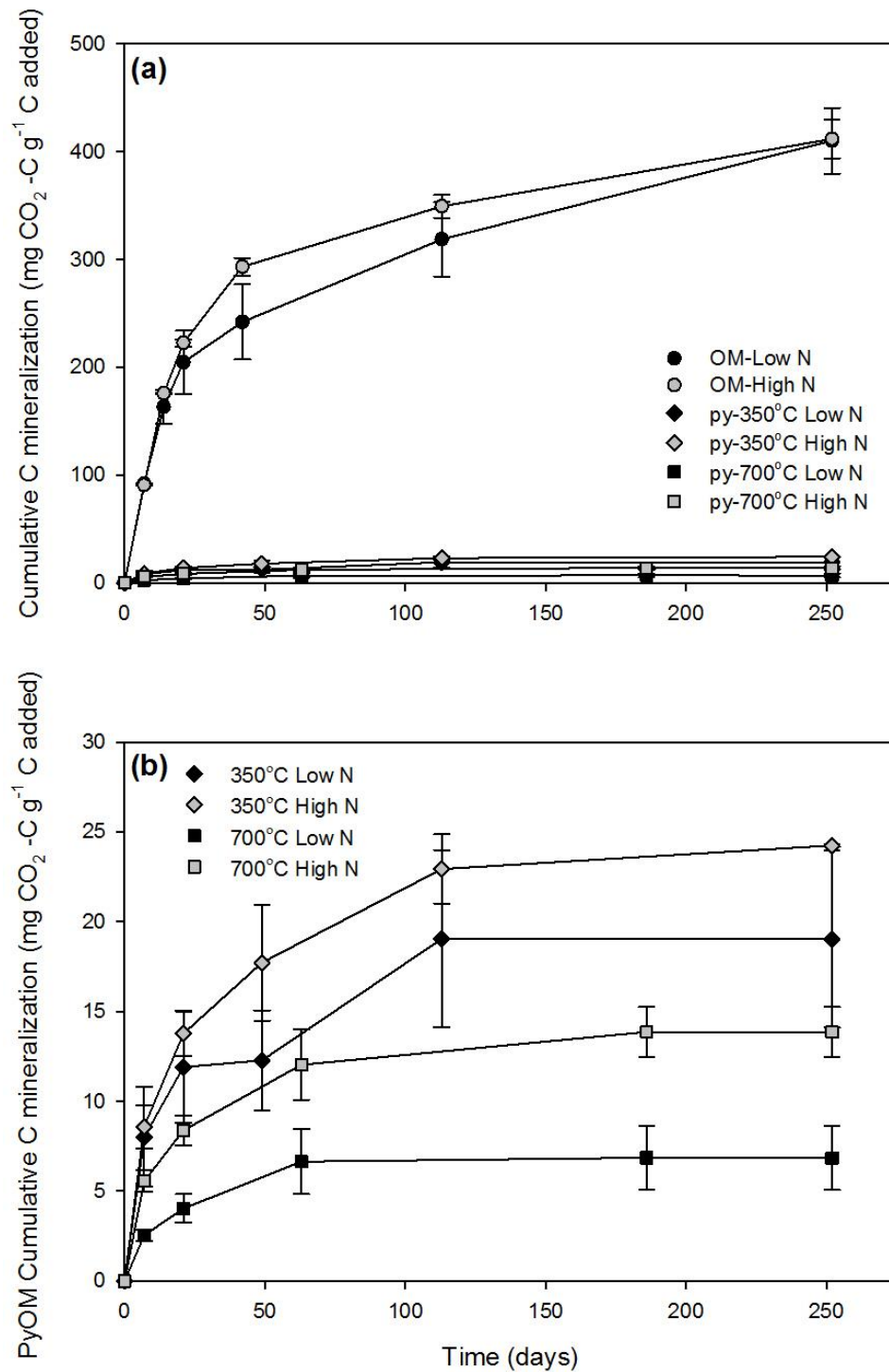


Figure 3.5: Cumulative C mineralized as a proportion of added C. (a) Cumulative C mineralization over time for maize leaves dried at 60°C and PyOM pyrolyzed at 350°C and 700°C, and (b) cumulative C mineralization for PyOM pyrolyzed at 350°C and 700°C. Black circles, diamonds and squares represent high N-containing maize leaves while grey circles, diamonds and squares represent low N-containing maize leaves.

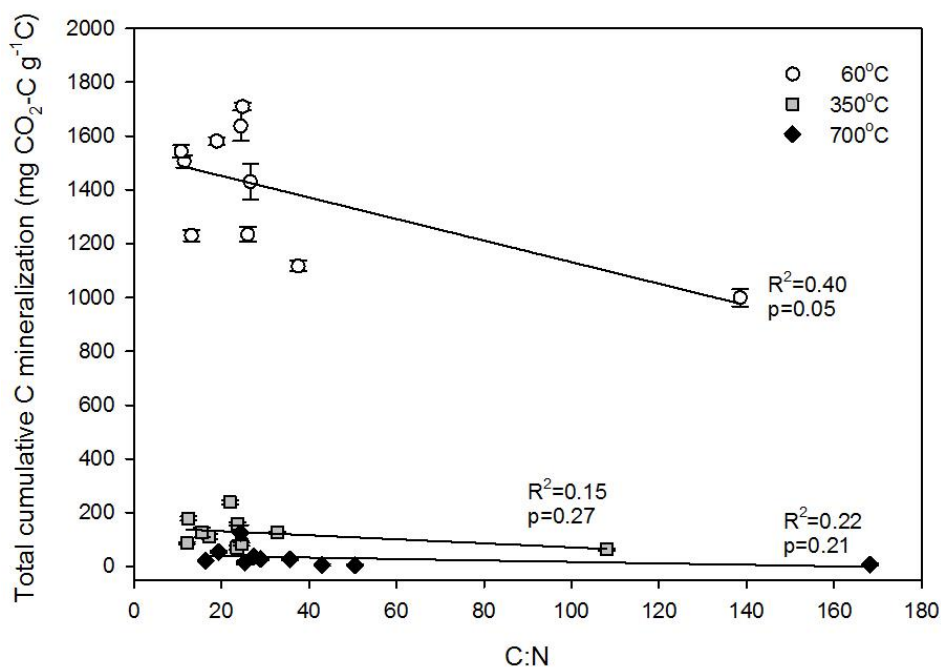


Figure 3.6: Relationship between the carbon-to-nitrogen ratio and the mineralization of OM or PyOM-C. White circles, grey squares and black squares represent OM, PyOM at 350°C and 700°C, respectively. Lines indicate linear regression: OM: $y = 1.53 - 0.004x$, $p = 0.05$, $R^2 = 0.40$; PyOM-C at 350° C: $y = 0.15 - 0.0008x$, $p = 0.27$, $R^2 = 0.15$; PyOM-C at 700° C: $y = 0.03 - 0.0002x$, $p = 0.21$, $R^2 = 0.22$.

3.5. PyOM-C mineralization and PyOM-N correlation

The abundance of C=N six-membered rings present in total PyOM had a negative and strong correlation with PyOM-C mineralization (Appendix Figure B.13). The N forms in the different fractions of PyOM (extracted PyOM and toluene extract) were also correlated to PyOM-C mineralization. Results obtained by multivariate data analysis strongly suggest that aromatic C=N in six-membered rings (putative) and aromatic C-N in oxygenated six-membered rings found in PyOM toluene extracts were highly correlated to the total cumulative mineralization of PyOM-C (Figure 3.7). PyOM-C mineralization was positively correlated to the presence of aromatic C-N in oxygenated six-membered rings, which explained 37% of the

variance in the model. The sequential inclusion of aromatic C=N in six-membered rings (putative) accounted for the remaining 18% of the variance in the model and was negatively correlated with PyOM-C mineralization.

For the remaining PyOM after extraction, C=N in six-membered rings (putative) was significantly ($p=0.0006$) and negatively correlated to PyOM-C mineralization (Appendix Figure B.14). C=N in six-membered rings alone accounted for 49% of the variance in the model.

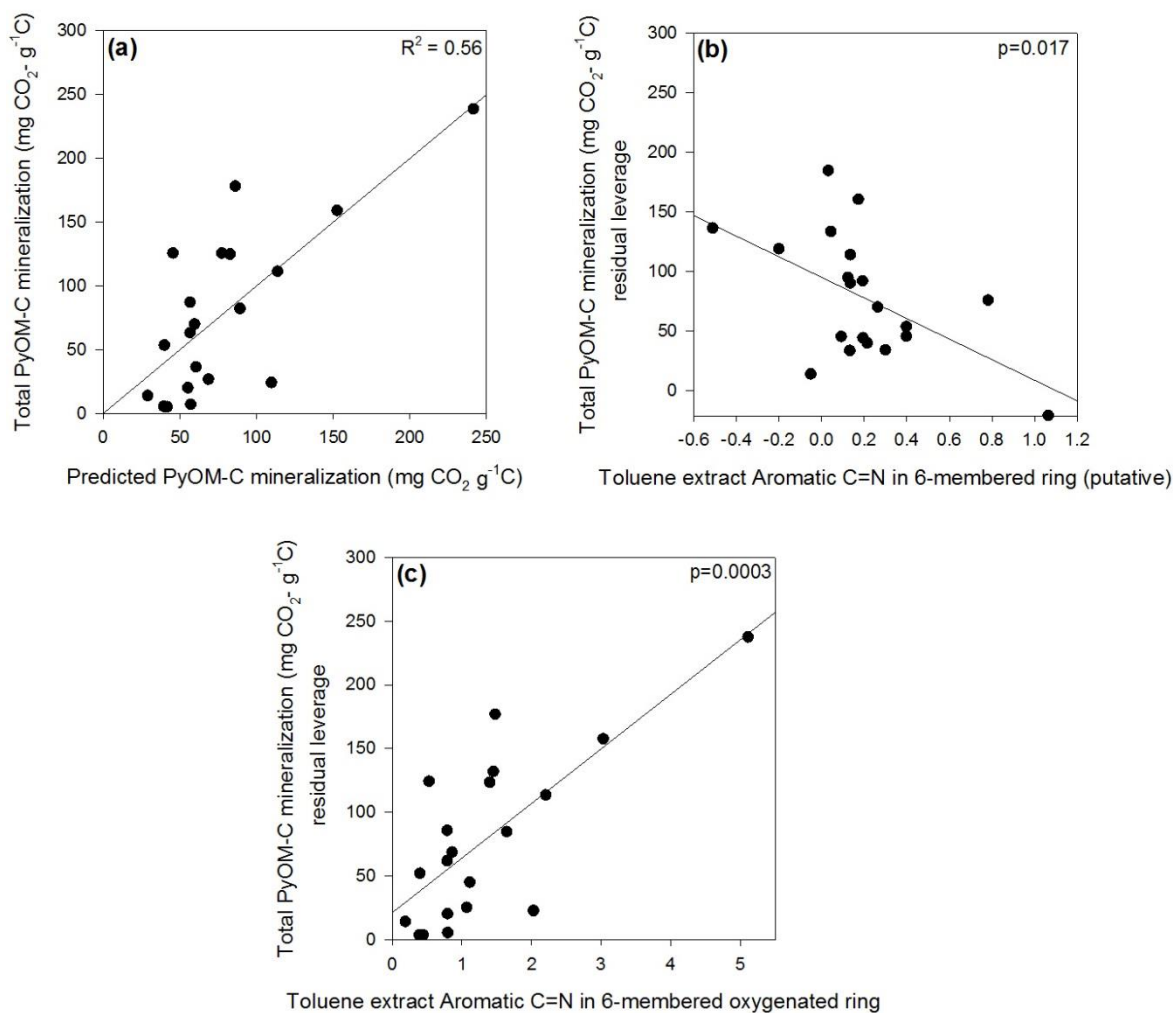


Figure 3.7: Relationship between cumulative PyOM-C mineralized and ratios of N functional groups from the PyOM toluene extract as observed by N K-edge NEXAFS. (a) Actual vs. multiple regression model predicted response values for cumulative PyOM-C mineralized, (b) relationship between cumulative PyOM-C mineralized and aromatic C=N in 6-membered rings, and (c) aromatic C=N in oxygenated 6-membered rings.

4. Discussion

4.1. Organic matter nitrogen content and pyrolysis temperature affect the molecular structure of PyOM-N

Ample evidence support the effects of pyrolysis temperature on the final molecular structure and N content of PyOM (Knicker et al., 1996; Almendros et al., 2003; Chen et al., 2014). Nitrogen in uncharred OM is mostly found in amino acids and proteins (Moens et al., 2004) that experience significant changes during thermal conversion. NEXAFS spectra in our study showed the transformation of OM-N mostly into aromatic N heterocycles and quaternary N. Our findings agree with various studies (Knicker et al., 1996; Almendros et al., 2003; Knicker, 2010; Chen et al., 2014) that report a high degree of aromatic N in PyOM. Quaternary N as observed in our study, is not commonly reported as a constituent of PyOM-N but mostly found in coal (Pels et al., 1995; Schmiers et al., 1999; Xiao et al., 2005). Quaternary N in our PyOM was a likely result of two reactions pathways. At lower pyrolysis temperatures, the presence of quaternary N is best explained by the neo-formation of the moiety. As pyrolysis temperature increases, condensation reactions lead to a rearrangement of N within the C network (Pels et al., 1995). Our data confirmed this possible reaction pathway as we can see that aromatic N heterocycles transform with increasing pyrolysis temperature (Figure 3.3). The increase in quaternary N followed a loss of aromatic N heterocycles, while quaternary N was preserved due to its thermal stability (Xiao et al., 2005).

While thermal conversion of OM-N was responsible for the high aromaticity of N and enrichment in the final PyOM-N, temperature alone in our study did not account for the formation of aromatic N heterocycles. Our results suggest that the initial OM-N content was correlated with the quantity of aromatic N heterocycles present in PyOM. Studies on N-doped C

(Bhattacharyya et al., 2002; Chen et al., 2010; Jian et al., 2013; Bulusheva et al., 2015) have reported a greater abundance of aromatic N heterocycles with higher N contents of the product. However, the incorporation of such exogenous N to a C matrix may proceed through potentially different reaction pathways than those of endogenous N in OM. To our knowledge there is no prior confirmation on how the initial N content in OM is correlated to the quantity of aromatic heterocyclic N structures during pyrolysis.

Several mechanisms may be responsible for an increase in the proportion of aromatic N with increasing N contents. Pyrolysis of both aliphatic and cyclic amino acids (AA) demonstrated the complex chemistry behind the formation of pyrolysis products (Sharma et al., 2003; Sharma et al., 2004). While most cyclic AA form or remain as aromatic N heterocycles, some aliphatic AA are also transformed into aromatic N heterocycles. AA with reactive polar side chains can form 5-, 6- or 7-membered aromatic heterocyclic compounds (Chiavari and Galletti, 1992; Sharma et al., 2004; Choi and Ko, 2011). However, the formation of aromatic N heterocycles in PyOM is much more complex than that of AA monomer pyrolysis.

An alternative theory to the formation of aromatic N heterocycles in PyOM follows the chemistry of Maillard reactions, where sugars and AA react during pyrolysis to form N-substituted polyaromatic rings (Darvell et al., 2012). OM is a mixture of mostly proteinaceous and aliphatic N along with cellulose, hemicellulose and lignin (Ren et al., 2011; Ren and Zhao, 2012), which reacts during pyrolysis to produce aromatic N heterocycles. Multiple studies on the pyrolysis of mixtures of sugars and AA model compounds (Britt et al., 2004; Moens et al., 2004; Sharma et al., 2009; Darvell et al., 2012) have reported the formation of N-substituted polyaromatic rings and explained this observation with Maillard reactions. It has been shown that the decomposition of the intermediate Amadori compound during pyrolysis was responsible for

aromatic N heterocycles, mostly found as aromatic C=N in 5-membered rings (pyrroles in the literature) (Shigematsu et al., 1977; Britt et al., 2004; Moens et al., 2004; Sharma et al., 2009) and to a lesser degree as aromatic C=N in 6-membered rings. These findings are primarily valid for gas phase N transformations and might not explain solid state reactions. In our study, we examined the molecular structure of the solid state products during pyrolysis. If Maillard reactions were a primary pathway for the formation of N heterocycles in PyOM, we would have expected to see a resolved peak at approximately 401.3 ± 0.12 eV. This peak represents the aromatic C=N 5-membered heterocycles that are a function of the degradation of Amadori compounds during pyrolysis (Yaylayan, 1990; Yaylayan et al., 1994) . However, our PyOM spectra (Figure 3.2) showed a broad unresolved shoulder at 401.3 eV, which suggests that the main Amadori decomposition products were not present in PyOM. Hence, Maillard reactions may not be the dominant pathway for the formation of aromatic N heterocycles in our study. In contrast, PyOM toluene extract spectra had a well-resolved peak in this region suggesting that the re-condensed pyrolysis gases in our study could be a product of gas-phase Millard reactions, similar to those reported in previous studies cited above. However, to confirm this explanation, further solid state and gas phase pyrolysis studies of OM-N are needed.

Several other studies (Jian et al., 2013; Bulusheva et al., 2015; Chen et al., 2017) have concluded that the molecular structure of the N precursor plays a significant role in the formation of aromatic N heterocycles. This conclusion would imply that if precursor N is present in an aromatic ring, then the final pyrolysis product will contain aromatic N heterocycles. However, no correlation exists between the proportion of aromatic N heterocycles in OM-N and PyOM. While our data did not show any correlation between precursor N structure and the final PyOM

structure, this does not conclusively exclude this reaction pathway. However, it may not be the dominant pathway to the increased proportion of aromatic N heterocycles in PyOM.

We propose an alternate explanation for the positive correlation between OM-N and aromatic N heterocycle contents based on the energetics of the bond formation. As N contents in OM decreased, N was preferentially incorporated into exocyclic N (i.e., amino groups) and quaternary N. On the other hand, as N contents increased, N atoms were more easily substituted or incorporated into aromatic sites. This phenomenon is associated with the energy needed to add N atoms into the C network. As the degree of condensation increased in PyOM, the incorporation of N into the C network becomes more energy intensive. The energy barrier associated with breaking C bonds to incorporate N atoms is high at lower N concentrations, while at higher N concentrations, the heat of formation of aromatic N heterocycles is lower (dos Santos and Alvarez, 1998; Chen et al., 2010) and therefore incorporation of N into the C network is energetically favorable.

4.2. Nitrogen effects on PyOM-N and PyOM-C mineralization

The molecular and structure change of OM-N during thermal degradation affected the availability of N and subsequent microbial oxidation. While OM-N exhibited net mineralization (Appendix Fig B.12a.), PyOM-N experienced net immobilization of N for PyOM at both 350°C and 700°C (Appendix Figure B.12b-c), despite the fact that the N content of the bulk PyOM did on average not decline compared to that of the original uncharred OM. The change from N mineralization to immobilization with increasing pyrolysis temperature can be best explained by the molecular and structural change experienced by N during thermal degradation, yet not by C:N stoichiometry or total N content. PyOM-N exhibited a highly aromatic structure that appeared to make N unavailable for microbial degradation. Similar PyOM-N immobilization has

been reported by others (Novak et al., 2010; Wang et al., 2012; Chen et al., 2014), however, the effect is considered short-lived (Bruun et al., 2012) and mineralization of aromatic N heterocycles in PyOM is possible in the long term (Hilscher and Knicker, 2011; de la Rosa and Knicker, 2011). Our N mineralization study lasted 50 days and therefore, the net N immobilization observed has to be seen in this context and a switch from immobilization to mineralization may be observed over longer periods of time.

Nonetheless, we observed PyOM-C mineralization during our study which indicates that a fraction of PyOM-C and PyOM-N is accessible to microbes. Several studies (Keiluweit et al., 2010; Deenik et al., 2010; Smith et al., 2010) have identified re-condensed volatiles found on the surface and in the pores of PyOM to contain easily mineralizable PyOM-C (Keiluweit et al., 2010; Smith et al., 2010) and PyOM-N (Deenik et al., 2010; Wang et al., 2012). Our multivariate regression model suggests that PyOM-C mineralization in our study is mostly controlled by aromatic N in six-membered heterocycles as well as aromatic six-membered N heterocycles containing a keto group found in the PyOM extract. While aromatic N in six-membered heterocycles in PyOM extracts inhibited the decomposition of PyOM-C, aromatic N in six-membered heterocycles containing a keto group stimulated PyOM-C mineralization.

We propose that aromatic N heterocycles in PyOM controlled PyOM-C mineralization via the location of N atoms. First, the molecular structure of the fraction of PyOM where N heterocycles are present had an effect on PyOM-C mineralization. The aromatic nature of N in PyOM extract may at first glance suggest that this type of N is not available for microbial use. However, microbial metabolization of aromatic N heterocycles is indeed possible via hydroxylation of the aromatic ring catalyzed by mono- or dehydrogenase in the presence of oxygen, followed by ring opening (Fetzner, 2000). The microbial degradation of aromatic N

heterocycles can yield aliphatic N compounds (Sims et al., 1989; Fetzner, 2000) readily available for microbial use. The transformation of both C and N through this process in turn allows the release of CO₂-C.

Secondly, the location of N atoms within the C network can also regulate the mineralization of PyOM-C. This is supported by the apparent contradiction that aromatic C=N in 6-membered rings inhibited PyOM-C mineralization, yet aromatic C=N in six-membered rings containing a keto group stimulated C mineralization. The different role of these two moieties in the control of PyOM-C mineralization can be best explained by the position of the N atom within the C structure of PyOM. Aromatic C=N in 6-membered rings can be found in the C backbone of PyOM (PyOM after extraction in our study) and was in fact the principal moiety controlling the mineralization of PyOM-C (Appendix Figure B.14). N atoms in this PyOM fraction are likely substitutes in the structure of amorphous C (Keiluweit et al., 2010; Knicker, 2010). Therefore, N atoms may be physically protected by highly condensed C domains and less likely to be oxidized. The aromatic C=N in 6-membered rings containing a keto group were present in the PyOM extract. Such aromatic N groups bearing a keto group are most likely found in the surface structure of PyOM. Several studies (Arrigo et al., 2010; Wang et al., 2012) have shown that oxygenated functional groups are preferentially located at the edge of the C network and may therefore be more easily metabolized by microorganisms.

5. Conclusion

The enrichment of N in PyOM is best explained by the incorporation of N atoms into heterocyclic aromatic moieties during pyrolysis rather than remnants of aromatic N structures in plant residues. While pyrolysis temperature has previously been considered the dominant control in the formation of aromatic N heterocycles, our study demonstrates that the initial N content of

the organic matter is equally as important in the formation of these moieties. In addition, the structural transformation of N in PyOM contributes to the persistence of PyOM in the environment through stabilization of PyOM-C. PyOM-C mineralization in the present study is affected by the molecular structure of N in different fractions of PyOM. Oxidized forms of N heterocycles found in the chemically extractable fraction of PyOM may explain the short-term increase in PyOM-C mineralization seen in most studies. In contrast, aromatic N heterocycles embedded in the C network of PyOM lead to lower mineralization of PyOM-C. These findings support the hypothesis that N forms in PyOM-C rather than N contents or C:N ratios play a major role in PyOM-C persistence. These findings need to be verified by future research where the combination of respiration experiments and analytical tools for molecular characterization are conducted under natural conditions over the short and long term.

Acknowledgements

This study was supported in part by the Cornell University Program in Biogeochemistry and Environmental Biocomplexity, National Science Foundation's Basic Research for Enabling Agricultural Development (NSF-BREAD Grant number IOS-0965336) and the Fondation des Fondateurs. DT acknowledges support from the NSF IGERT Program (DGE-0903371).

Research described in this paper was performed at the Canadian Light Source Inc., which is supported by the Natural Sciences and Engineering Research Council of Canada.

The authors would like acknowledge the helpful support of James Dynes, Adam Gillespie, and Tom Regier at the Canadian Light Source Inc. We would also like to thank Akio Enders and Kelly Hanley for all the help with logistical and experimental work.

References

- Almendros G., Knicker H. and González-Vila F. J. (2003) Rearrangement of carbon and nitrogen forms in peat after progressive thermal oxidation as determined by solid-state ^{13}C - and ^{15}N -NMR spectroscopy. *Org. Geochem.* **34**, 1559–1568.
- Arrigo R., Hävecker M., Wrabetz S., Blume R., Lerch M., McGregor J., Parrott E. P. J., Zeitler J. A., Gladden L. F., Knop-Gericke A., Schlögl R. and Su D. S. (2010) Tuning the acid/base properties of nanocarbons by functionalization via amination. *J. Am. Chem. Soc.* **132**, 9616–9630.
- Bhattacharyya S., Lübbe M., Bressler P. R., Zahn D. R. T. and Richter F. (2002) Structure of nitrogenated amorphous carbon films from NEXAFS. *Diam. Relat. Mater.* **11**, 8–15.
- Bird M. I., Wynn J. G., Saiz G., Wurster C. M. and McBeath A. (2015) The pyrogenic carbon cycle. *Annu. Rev. Earth Planet. Sci.* **43**, 273–298.
- Britt P. F., Buchanan A. C., Owens C. V. and Todd Skeen J. (2004) Does glucose enhance the formation of nitrogen containing polycyclic aromatic compounds and polycyclic aromatic hydrocarbons in the pyrolysis of proline? *Fuel* **83**, 1417–1432.
- Bruun E. W., Ambus P., Egsgaard H. and Hauggaard-Nielsen H. (2012) Effects of slow and fast pyrolysis biochar on soil C and N turnover dynamics. *Soil Biol. Biochem.* **46**, 73–79.
- Bulusheva L. G., Okotrub A. V., Fedoseeva Y. V., Kurenaya A. G., Asanov I. P., Vilkov O. Y., Koós A. A. and Grobert N. (2015) Controlling pyridinic, pyrrolic, graphitic, and molecular nitrogen in multi-wall carbon nanotubes using precursors with different N/C ratios in aerosol assisted chemical vapor deposition. *Phys. Chem. Chem. Phys. PCCP* **17**, 23741–23747.
- Chen C.-P., Cheng C.-H., Huang Y.-H., Chen C.-T., Lai C.-M., Menyailo O. V., Fan L.-J. and Yang Y.-W. (2014) Converting leguminous green manure into biochar: changes in chemical composition and C and N mineralization. *Geoderma* **232–234**, 581–588.
- Chen W., Yang H., Chen Y., Xia M., Chen X. and Chen H. (2017) Transformation of Nitrogen and Evolution of N-Containing Species during Algae Pyrolysis. *Environ. Sci. Technol.* **51**, 6570–6579.
- Chen Zhu, Higgins D. and Chen Zhongwei (2010) Nitrogen doped carbon nanotubes and their impact on the oxygen reduction reaction in fuel cells. *Carbon* **48**, 3057–3065.
- Chiavari G. and Galletti G. C. (1992) Pyrolysis—gas chromatography/mass spectrometry of amino acids. *J. Anal. Appl. Pyrolysis* **24**, 123–137.
- Choi S.-S. and Ko J.-E. (2011) Analysis of cyclic pyrolysis products formed from amino acid monomer. *J. Chromatogr. A* **1218**, 8443–8455.

- Darvell L. I., Brindley C., Baxter X. C., Jones J. M. and Williams A. (2012) Nitrogen in biomass char and its fate during combustion: a model compound approach. *Energy Fuels* **26**, 6482–6491.
- Deenik J. L., McClellan T., Uehara G., Antal M. J. and Campbell S. (2010) Charcoal volatile matter content influences plant growth and soil nitrogen transformations. *Soil Sci. Soc. Am. J.* **74**, 1259–1270.
- Fetzner S. (2000) Enzymes involved in the aerobic bacterial degradation of N-heteroaromatic compounds: molybdenum hydroxylases and ring-opening 2,4-dioxygenases. *Naturwissenschaften* **87**, 59–69.
- Fox R. H., Myers R. J. K. and Vallis I. (1990) The nitrogen mineralization rate of legume residues in soil as influenced by their polyphenol, lignin, and nitrogen contents. *Plant Soil* **129**, 251–259.
- Haney R. L. and Haney E. B. (2010) Simple and rapid laboratory method for rewetting dry soil for incubations. *Commun. Soil Sci. Plant Anal.* **41**, 1493–1501.
- Heymann K., Lehmann J., Solomon D., Schmidt M. W. I. and Regier T. (2011) C 1s K-edge near edge X-ray absorption fine structure (NEXAFS) spectroscopy for characterizing functional group chemistry of black carbon. *Org. Geochem.* **42**, 1055–1064.
- Hilscher A., Heister K., Siewert C. and Knicker H. (2009) Mineralisation and structural changes during the initial phase of microbial degradation of pyrogenic plant residues in soil. *Org. Geochem.* **40**, 332–342.
- Hilscher A. and Knicker H. (2011) Carbon and nitrogen degradation on molecular scale of grass-derived pyrogenic organic material during 28 months of incubation in soil. *Soil Biol. Biochem.* **43**, 261–270.
- Jian G., Zhao Y., Wu Q., Yang L., Wang X. and Hu Z. (2013) Structural and compositional regulation of nitrogen-doped carbon nanotubes with nitrogen-containing aromatic precursors. *J. Phys. Chem. C* **117**, 7811–7817.
- Keiluweit M., Nico P. S., Johnson M. G. and Kleber M. (2010) Dynamic molecular structure of plant biomass-derived black carbon (biochar). *Environ. Sci. Technol.* **44**, 1247–1253.
- Knicker H. (2010) “Black nitrogen” – an important fraction in determining the recalcitrance of charcoal. *Org. Geochem.* **41**, 947–950.
- Knicker H., Almendros G., González-Vila F. J., Martin F. and Lüdemann H.-D. (1996) ¹³C- and ¹⁵N-NMR spectroscopic examination of the transformation of organic nitrogen in plant biomass during thermal treatment. *Soil Biol. Biochem.* **28**, 1053–1060.
- Lehmann J., Abiven S., Kleber M., Pan G., Singh B. P., Sohi S. P. and Zimmerman A. R. (2015) Persistence of biochar in soil. In *Biochar for Environmental Management: Science, Technology and Implementation* Routledge, London, United Kingdom. pp. 235–282.

- McBeath A. V., Smernik R. J., Schneider M. P., Schmidt M. W. and Plant E. L. (2011) Determination of the aromaticity and the degree of aromatic condensation of a thermosequence of wood charcoal using NMR. *Org. Geochem.* **42**, 1194–1202.
- McBeath A. V., Wurster C. M. and Bird M. I. (2015) Influence of feedstock properties and pyrolysis conditions on biochar carbon stability as determined by hydrogen pyrolysis. *Biomass Bioenergy* **73**, 155–173.
- Melillo J. M., Aber J. D. and Muratore J. F. (1982) Nitrogen and lignin control of hardwood leaf litter decomposition dynamics. *Ecology* **63**, 621–626.
- Moens L., Evans R. J., Looker M. J. and Nimlos M. R. (2004) A comparison of the Maillard reactivity of proline to other amino acids using pyrolysis-molecular beam mass spectrometry. *Fuel* **83**, 1433–1443.
- Novak J. M., Busscher W. J., Watts D. W., Laird D. A., Ahmedna M. A. and Niandou M. A. S. (2010) Short-term CO₂ mineralization after additions of biochar and switchgrass to a Typic Kandiudult. *Geoderma* **154**, 281–288.
- Pels J. R., Kapteijn F., Moulijn J. A., Zhu Q. and Thomas K. M. (1995) Evolution of nitrogen functionalities in carbonaceous materials during pyrolysis. *Carbon* **33**, 1641–1653.
- Preston C. M. and Schmidt M. W. I. (2006) Black (pyrogenic) carbon: a synthesis of current knowledge and uncertainties with special consideration of boreal regions. *Biogeosciences* **3**, 397–420.
- Ren Q. and Zhao C. (2012) NO_x and N₂O precursors from biomass pyrolysis: Nitrogen transformation from amino acid. *Environ. Sci. Technol.* **46**, 4236–4240.
- Ren Q., Zhao C., Chen X., Duan L., Li Y. and Ma C. (2011) NO_x and N₂O precursors (NH₃ and HCN) from biomass pyrolysis: Co-pyrolysis of amino acids and cellulose, hemicellulose and lignin. *Proc. Combust. Inst.* **33**, 1715–1722.
- de la Rosa J. M. and Knicker H. (2011) Bioavailability of N released from N-rich pyrogenic organic matter: An incubation study. *Soil Biol. Biochem.* **43**, 2368–2373.
- Santín C., Doerr S. H., Kane E. S., Masiello C. A., Ohlson M., de la Rosa J. M., Preston C. M. and Dittmar T. (2016) Towards a global assessment of pyrogenic carbon from vegetation fires. *Glob. Change Biol.* **22**, 76–91.
- dos Santos M. C. and Alvarez F. (1998) Nitrogen substitution of carbon in graphite: structure evolution toward molecular forms. *Phys. Rev. B* **58**, 13918–13924.
- SAS Institute (2015) *JMP Pro.*, SAS Institute Inc, Cary, N.C.
- Schmidt M. W. I. and Noack A. G. (2000) Black carbon in soils and sediments: analysis, distribution, implications, and current challenges. *Glob. Biogeochem. Cycles* **14**, 777–793.

- Schmiers H., Friebel J., Streubel P., Hesse R. and Köpsel R. (1999) Change of chemical bonding of nitrogen of polymeric N-heterocyclic compounds during pyrolysis. *Carbon* **37**, 1965–1978.
- Sharma R. K., Chan W. G. and Hajaligol M. R. (2009) Effect of reaction conditions on product distribution from the co-pyrolysis of α -amino acids with glucose. *J. Anal. Appl. Pyrolysis* **86**, 122–134.
- Sharma R. K., Chan W. G., Seeman J. I. and Hajaligol M. R. (2003) Formation of low molecular weight heterocycles and polycyclic aromatic compounds (PACs) in the pyrolysis of α -amino acids. *J. Anal. Appl. Pyrolysis* **66**, 97–121.
- Sharma R. K., Chan W. G., Wang J., Waymack B. E., Wooten J. B., Seeman J. I. and Hajaligol M. R. (2004) On the role of peptides in the pyrolysis of amino acids. *J. Anal. Appl. Pyrolysis* **72**, 153–163.
- Shigematsu H., Shibata S., Kurata T., Kato H. and Fujimaki M. (1977) Thermal degradation products of several Amadori compounds. *Agric. Biol. Chem.* **41**, 2377–2385.
- Sims G. K., O’Loughlin E. J. and Crawford R. L. (1989) Degradation of pyridines in the environment. *Crit. Rev. Environ. Control* **19**, 309–340.
- Smith J. L., Collins H. P. and Bailey V. L. (2010) The effect of young biochar on soil respiration. *Soil Biol. Biochem.* **42**, 2345–2347.
- Stańczyk K., Dziembaj R., Piwowarska Z. and Witkowski S. (1995) Transformation of nitrogen structures in carbonization of model compounds determined by XPS. *Carbon* **33**, 1383–1392.
- Wang J., Xiong Z. and Kuzyakov Y. (2016) Biochar stability in soil: meta-analysis of decomposition and priming effects. *Glob. Change Biol. Bioenergy* **8**, 512–523.
- Wang T., Camps Arbestain M., Hedley M. and Bishop P. (2012) Chemical and bioassay characterisation of nitrogen availability in biochar produced from dairy manure and biosolids. *Org. Geochem.* **51**, 45–54.
- Whitman T., Zhu Z. and Lehmann J. (2014) Carbon mineralizability determines interactive effects on mineralization of pyrogenic organic matter and soil organic carbon. *Environ. Sci. Technol.* **48**, 13727–13734.
- Wiedemeier D. B., Abiven S., Hockaday W. C., Keiluweit M., Kleber M., Masiello C. A., McBeath A. V., Nico P. S., Pyle L. A., Schneider M. P. W., Smernik R. J., Wiesenberger G. L. B. and Schmidt M. W. I. (2015) Aromaticity and degree of aromatic condensation of char. *Org. Geochem.* **78**, 135–143.
- Wojdyr M. (2010) Fityk: a general-purpose peak fitting program. *J. Appl. Crystallogr.* **43**, 1126–1128.

- Woo S. H., Enders A. and Lehmann J. (2016) Microbial mineralization of pyrogenic organic matter in different mineral systems. *Org. Geochem.* **98**, 18–26.
- Xiao B., Boudou J. P. and Thomas K. M. (2005) Reactions of nitrogen and oxygen surface groups in nanoporous carbons under inert and reducing atmospheres. *Langmuir ACS J. Surf. Colloids* **21**, 3400–3409.
- Yaylayan V. (1990) In search of alternative mechanisms for the Maillard reaction. *Trends Food Sci. Technol.* **1**, 20–22.
- Yaylayan V. A., Huyghues-Despointes A. and Feather D. M. S. (1994) Chemistry of Amadori rearrangement products: Analysis, synthesis, kinetics, reactions, and spectroscopic properties. *Crit. Rev. Food Sci. Nutr.* **34**, 321–369.

APPENDIX A

Appendix Material

Carbon and nitrogen emissions rates and heat transfer of an indirect pyrolysis biomass cookstove

1. Fuel properties of solid biomass fuels, biochar, and charcoal

The moisture content of solid biomass fuels and elemental composition and heating value of solid biomass fuels, biochar (the charred residue in the pyrolysis chamber) and wood charcoal (the charred residue in the combustion chamber) are listed in Table A.1 and Table A.2. Biochar samples from pellets of hardwood (Instant Heat and Dry Creek brand) and switchgrass are denoted as BIHWP, BDCWP, and BSGP. The analyses of elemental composition were performed on an NC2500 (Carlo Erba, Italy) elemental analyzer coupled to a Thermo Scientific Delta V IRMS (Germany), and the analyses of higher heating value are performed on a Parr Model 6200 (Parr Instrument Company, USA) calorimeter.

Table A. 1:Moisture content of pyrolysis and combustion biomass fuels at the time of individual stove tests. See Deng et al., (2018) for moisture data from additional tests.

Sample name	Note	Moisture (% , as received basis)
Instant Heat Wood Pellet		
IHWP1	Pyrolysis fuel	4.80
Pine Wood	Combustion fuel	9.57
IHWP2	Pyrolysis fuel	4.90
Pine Wood	Combustion fuel	9.62
IHWP3	Pyrolysis fuel	5.09
Pine Wood	Combustion fuel	9.85
Dry Creek Wood Pellet		
DCWP1	Pyrolysis fuel	6.24
Pine Wood	Combustion fuel	10.29
DCWP2	Pyrolysis fuel	6.24
Pine Wood	Combustion fuel	11.11
DCWP3	Pyrolysis fuel	6.22
Pine Wood	Combustion fuel	9.83
DCWP4	Pyrolysis fuel	6.27
Pine Wood	Combustion fuel	10.55
Switchgrass Pellet		
SGP1	Pyrolysis fuel	7.60
Pine Wood	Combustion fuel	9.29
SGP2	Pyrolysis fuel	7.47
Pine Wood	Combustion fuel	10.98
SPG3	Pyrolysis fuel	8.17
Pine Wood	Combustion fuel	10.94
SPG4	Pyrolysis fuel	8.21
Pine Wood	Combustion fuel	9.98
SGP5	Pyrolysis fuel	9.16
Pine Wood	Combustion fuel	9.98

Table A. 2: Elemental composition and higher and lower heating values (HHV, LHV) of triplicate samples of biomass fuel, biochar and wood charcoal (n=3) Each row of biochar properties represents a separate stove test. Each row of wood properties represents a different batch of wood, used in several stove tests. Fuel, wood charcoal and biochar properties for additional stove tests appear in Deng et al., (2018).

Sample name	Elemental composition (% , dry basis)				Heating values (kJ kg ⁻¹ , dry basis)	
	C (%)	N (%)	H (%)	O (%)	HHV	LHV
Pyrolysis fuel						
IHWP	54.57	0.11	6.48	44.61	18865	17491
st dev	0.93	0.00	0.16	1.30	N/A	
Combustion fuel						
Wood	57.64	0.07	6.19	42.13	19550	18237
st dev	1.13	0.00	0.19	1.30	241	
Wood1	56.15	0.04	6.19	45.27	19036	17722
st dev	0.74	0.00	0.06	0.47	174	
Wood2	56.57	0.04	6.09	44.44	19366	18074
st dev	0.59	0.00	0.07	0.64	368	
Wood3	55.60	0.04	6.09	44.44	19270	17979
st dev	0.53	0.00	0.11	0.84	224	
Biochar for Instant heat wood pellet						
IHWP1	77.93	0.27	3.86	20.18	28317	27498
st dev	1.23	0.00	0.40	0.79	22	
IHWP2	79.26	0.25	3.56	18.49	28416	27660
st dev	0.55	0.00	0.16	0.97	234	
IHWP3	79.21	0.24	3.61	19.51	28233	27468
st dev	0.37	0.00	0.12	2.19	71	
Biochar for Dry Creek wood pellet						
BDCWP1	82.57	0.34	3.31	15.94	29339	28636
st dev	1.66	0.00	0.08	1.03	99	
BDCWP2	83.16	0.32	3.38	16.19	29170	28453
st de	0.95	0.01	0.17	2.01	64	
BDCWP3	83.95	0.34	3.33	16.12	29460	28754
st dev	0.56	0.01	0.06	1.30	250	
BDCWP4	83.22	0.33	3.27	15.16	29506	28812
st dev	0.79	0.01	0.36	1.51	409	
Biochar for Switchgrass pellet						
BSGP4	73.01	2.04	3.35	17.43	26426	25716
st dev	0.85	0.03	0.19	0.51	6	

BSGP5	72.50	2.04	3.39	17.77	26191	25472
st dev	1.61	0.03	0.14	0.90	139	
Wood Charcoal	89.28	0.08	1.36	6.44	30556	30268
st dev	1.07	0.01	0.05	0.22	163	

¹Standard deviation.

2. Materials and methods

2.1. Stove description and pictures

The cookstove used in this study is an indirect pyrolysis cookstove. This stove differs from traditional cookstoves because it serves a dual purpose, cooking with biomass energy and producing biochar. It is composed of three main parts (Figure A.1); (A) pyrolysis chamber, (B) pyrolysis chamber lid and (C) outer shell (Appendix Figure A.1). The pyrolysis chamber (A) is composed of two concentric cylindrical walls traversed by a wood feed. The region between the walls is the pyrolysis zone, while the central region, inside the inner wall, is the combustion zone. Solid biomass fuel is placed in the pyrolysis zone and heated indirectly by conduction (Zaror and Pyle, 1982) of heat produced in the combustion zone. The pyrolysis chamber lid (B), is placed over the pyrolysis chamber, covering the pyrolysis zone and leaving the combustion zone exposed. The lid creates a low-oxygen environment in the pyrolysis zone. During the initial heating of the solid biomass fuel, dehydration and devolatilization of low-molecular-weight components occur (Shafizadeh, 1982; Zaror and Pyle, 1982; Demirbas, 2004). However, at heating temperatures above 250°C, the biomass begins to pyrolyze (Shafizadeh, 1982; Zaror and Pyle, 1982; Demirbas, 2004), leading to the production of larger quantities of combustible gasses. As biomass is devolatilized, hot gases flow into the combustion chamber through a gap between the pyrolysis lid and the combustion chamber. Hot gases are combusted when they come into contact with heated primary air in the combustion zone. The outer shell of the

cookstove serves multiple purposes. The shell creates an air gap between the outer pyrolysis chamber wall and the cookstove users. Secondary air enters the stove through inlets on the bottom of the outer shell (Appendix Figure A.2) and is preheated as it sweeps along the outer wall of the pyrolysis chamber. The preheated secondary air contributes to the complete combustion of the biomass volatiles. Also, the outer shell is used to support cooking pots over the combustion chamber.

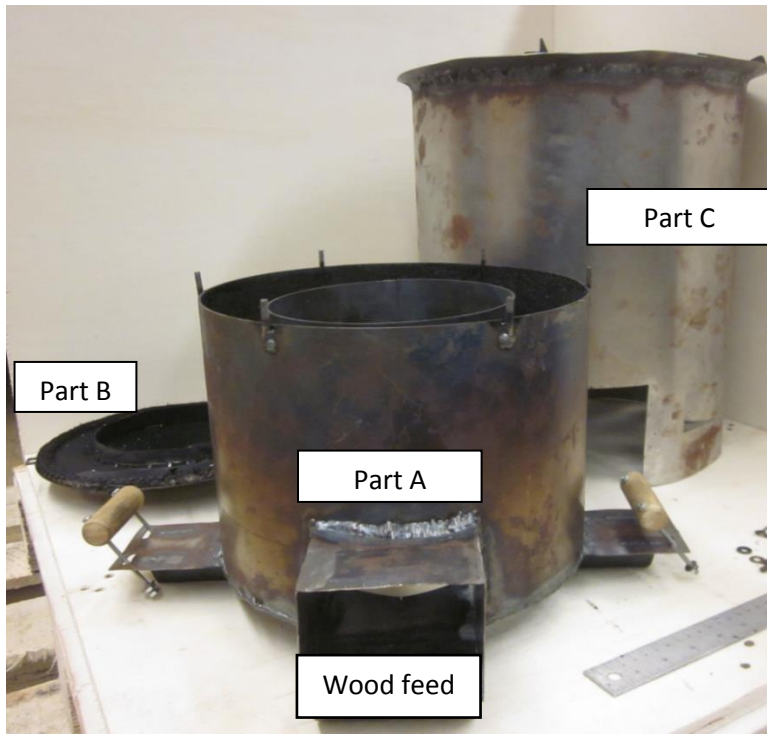


Figure A. 1: Main components of the pyrolysis cookstove

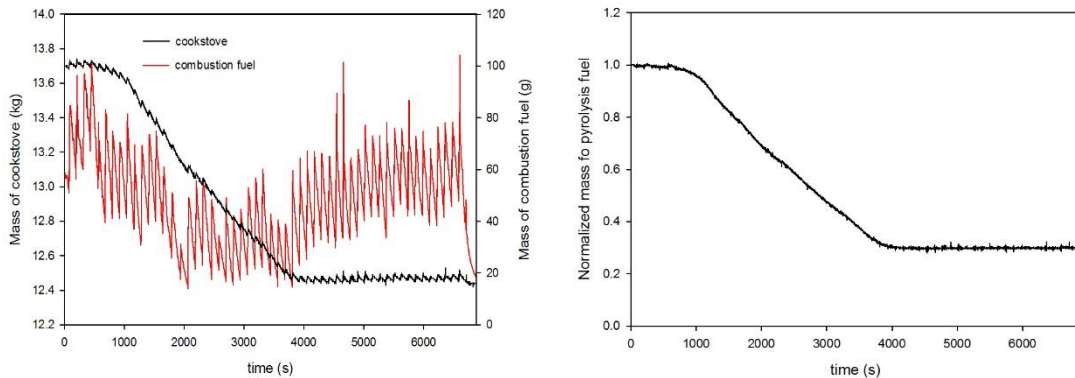


Figure A. 2: Secondary air inlets are bent in to induce swirl.

2.2. Calculations and data analysis

2.2.1. Data processing for instantaneous measurements and derived variables used in models

Raw measurements of masses vs. time appear in Figure A.4a. The mass of combustion wood, biochar, and grate (m_w) vs time shows a sawtooth pattern, with (1) a rapid rise in mass, corresponding to the insertion of a new batch of wood, followed by (2) a slower decline in mass, corresponding to the combustion of the current batch of wood. The sawtooth width is 2-3 minutes, which is the time between wood feedings. The mass of the stove (m_s) shows random fluctuations comparable in magnitude to the sawtooth pattern (Figure A.4a), due to the lower resolution on the scale used for that measurement. The mass of the contents of the pyrolysis chamber, m_{py} , was obtained from the combined mass of the wood, biochar and grate (m_w) and the mass of the stove (m_s) through the following steps. The limited resolution of the large scale used for mass of the wood, biochar and grate (m_w) dictated some aspects of the data processing. Specifically, as described below, it necessitated that time averaging be performed over the wood feed interval.



(a) Mass of combustion fuel and cookstove (b) Normalized mass of pyrolysis fuel

Figure A. 3: Mass histories

The mass of the wood, biochar, and grate (m_w) measurements were used to identify the time periods during which wood feedings occurred, i.e. time periods when m_w increased. These brief time periods were discarded from further analysis because mass changes during these periods represent the indistinguishable effects of mass loss from chemical reaction and mass gain due to wood feeding. The time periods between wood feedings, where the mass of the wood, biochar and, grate (m_w) has a negative slope with respect to time, were selected for further processing. For each of these periods, a linear fit of mass of the wood, biochar and grate (m_w) vs time was used to determine the rate of combustion fuel consumption (\dot{m}_w). For the same time periods, a linear fit of the total mass of the cookstove (m_s) vs time was performed. The rate of pyrolysis fuel consumption (\dot{m}_{py}) was determined for a given time period by subtracting the rate of combustion fuel consumption (\dot{m}_w) from the magnitude of the slope of the total mass of the cookstove (m_s) vs time. Temperatures and mass fractions were averaged, and a linear fit of the temperature of the water in the pot (T_w) with respect to time was performed, over the same time periods used in the processing of mass data. Each time period between wood feeds (approximately two minutes) thus made up a single data point, for which values of temperatures, fuel masses, and time derivatives of these quantities, were known.

Certain time periods were discarded from further analysis on the basis of quality measures. Specifically, R^2 for the linear fits was required to be no lower than 0.75. Any time periods in which the temperature of the water in the pot (T_w) had a negative slope were discarded, as these periods corresponded to the swapping of water pots. Any time periods in which the total mass of the cookstove (m_s) had a positive slope were discarded, as were time periods shorter than 50 seconds, as these periods generally corresponded to times when the stove had been bumped accidentally. After all these criteria were applied, 485 data points remained,

each representing the average behavior of the system during the time between two successive wood feedings. Eleven separate water boiling tests were represented. The results are considered robust because they were found to be insensitive to slight changes of criteria for selecting and rejecting time periods.

Figure A.5 shows the resulting measured quantities and derived variables for the cookstoves. These measurements were used in the models as independent variables to explain variability in selected performance indicators. The following plots include all the data points used to develop the models describing cookstove performance. The plots show the fuel consumption rate for the combustion fuel (a) and pyrolysis fuel (b). The rate of consumption of the combustion fuel shows very little variability when compared to the pyrolysis fuel; this is because the feeding rate of the combustion fuel was kept constant throughout the test. The non-linear variable for the pyrolysis fuel rate consumption is presented by plot (c). Plot (d) presents the rate of release of the N from the pyrolysis fuel. The higher values of $\dot{m}_{py} * X_n$, represent the fuel that had higher initial N content. Plot (e) represents the level of completeness of pyrolysis, f_{py} . This variable is defined as the fraction of the initial amount of pyrolysis fuel converted to biochar at a given time.

$$f_{py} = \frac{\text{mass of pyrolysis fuel at time } x - \text{initial mass of pyrolysis fuel}}{\text{final mass of pyrolysis fuel} - \text{initial mass of pyrolysis fuel}} \quad (8)$$

f_{py} approaches 1 when pyrolysis is complete. Plot (f) shows the water temperature for the three pots of water boiled.

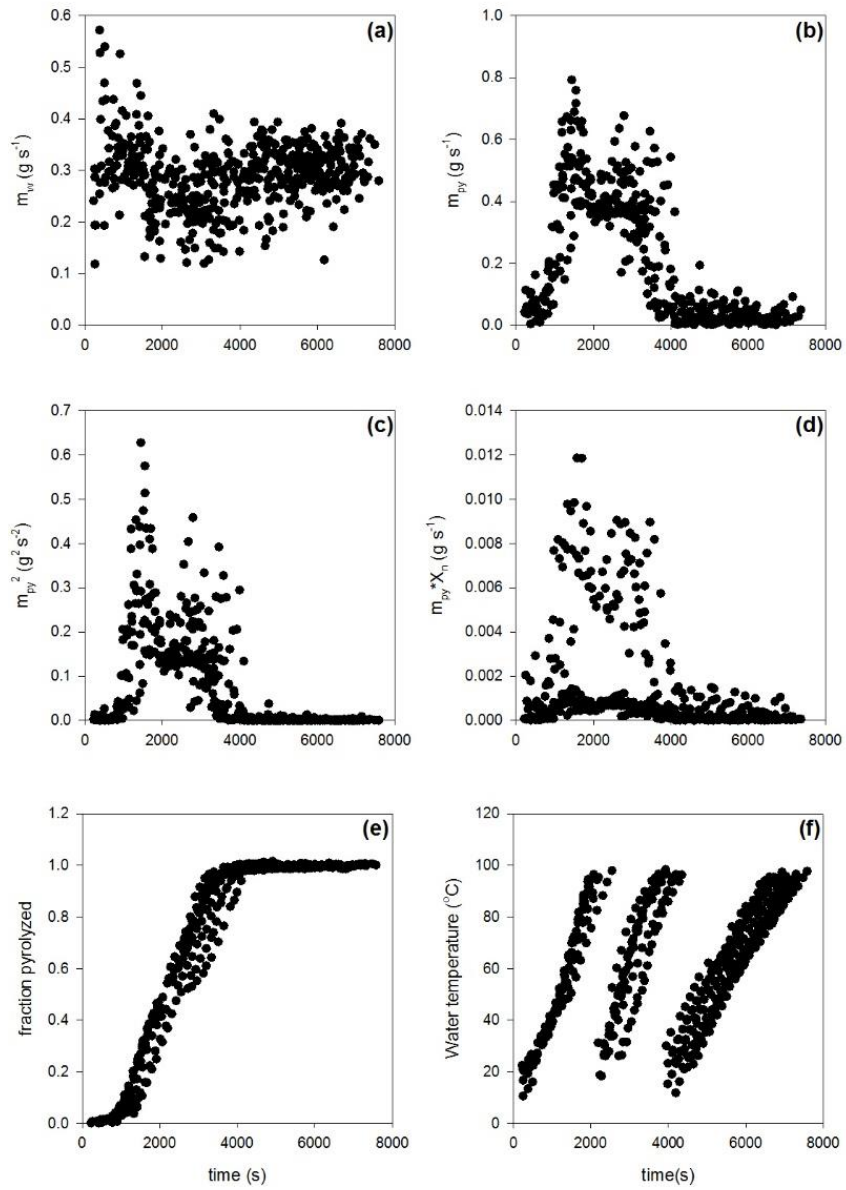


Figure A. 4: Instantaneous measurements of selected independent operating parameters

3. Results

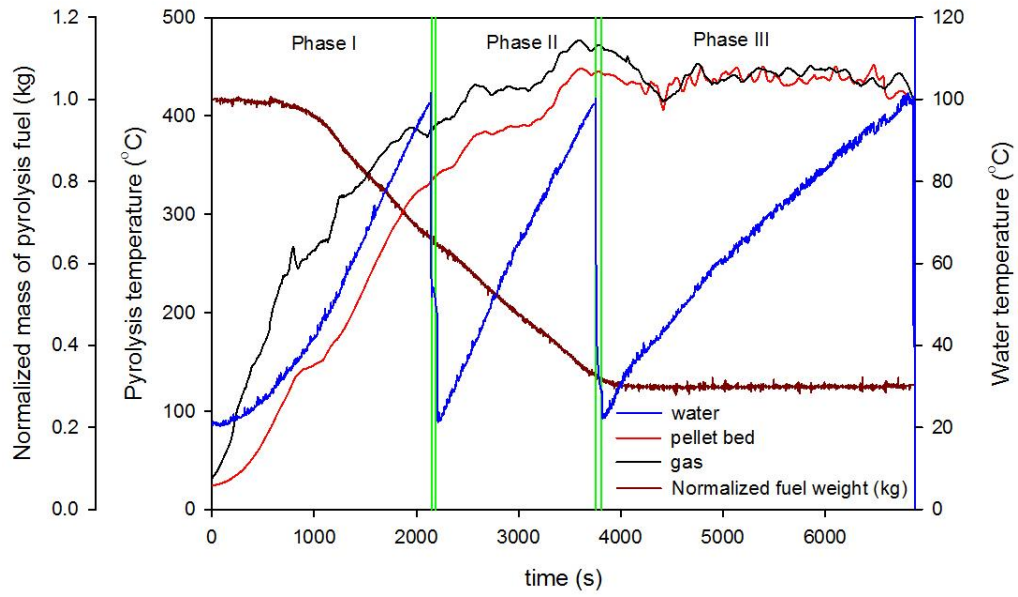


Figure A. 5: Pyrolysis and water temperatures for wood pellet

References

- Demirbas A. (2004) Combustion characteristics of different biomass fuels. *Prog. Energy Combust. Sci.* **30**, 219–230.
- Deng L., Torres-Rojas D., Burford M., Whitlow T. H., Lehmann J. and Fisher E. M. (2018) Fuel sensitivity of biomass cookstove performance. *Appl. Energy* **215**, 13–20.
- Shafizadeh F. (1982) Introduction to pyrolysis of biomass. *J. Anal. Appl. Pyrolysis* **3**, 283–305.
- Zaror C. A. and Pyle D. L. (1982) The pyrolysis of biomass: A general review. *Proc. Indian Acad. Sci. Sect. C Eng. Sci.* **5**, 269–285.

APPENDIX B

Appendix Material

Thermochemical and biological transformation of organic nitrogen in plant residues

1. Appendix Materials and Methods

1.1. Plant residues

Maize- *Zea mays* L., ryegrass- *Lolium perenne* L., and willow- *Salix viminalis* L. plants were grown under controlled conditions in a greenhouse. A mixture of peat moss, vermiculite and perlite (1:1:1 per volume) was used. Each plant species was fertilized with a customized Hoagland's solution with varying concentrations of N. Eight different N concentrations were used each adjusted to the specific plant species.

Due to different rates of dry matter accumulation between plant species, aboveground biomass was harvested on different dates. Ryegrass was grown for approximately 30 days and leaf blade clippings were harvested twice during the entire growth period. Maize was grown for 28 days and willow was allowed to grow and pruned every 30 days to allow for new growth.

1.2. NEXAFS sample preparation

Solid samples (i.e., PyOM and PyOM after extraction) were mixed with deionized water (0.5 mg mL⁻¹ water) in 1.5-mL Eppendorf vials to obtain a slurry. Samples were thoroughly mixed using a vortex mixer to achieve homogenous wetting. Using a pipette, an aliquot of 4 μ L was deposited onto Au coated Si wafers and air-dried at room temperature. Toluene extract solution was directly deposited and dispersed onto an Au coated Si wafer. The toluene was allowed to evaporate under atmospheric conditions under a hood resulting in a thin layer of extract. Wafers were affixed to the sample plate using double-sided carbon tape before insertion into the absorption chamber.

1.3. Microbial inoculum isolation and preparation

A microbial inoculum was isolated from historical charcoal furnace soil samples from Alabama (Cheng et al., 2008). A homogenous soil mixture was prepared by adding a nutrient solution. The homogenous mixture of surface and subsurface soil at 55% WHC was incubated at 30°C for 7 days to stimulate microbial activity. The soil-water mixture was filtered through a Whatman #1 filter paper to obtain the microbial inoculum. Thereafter a nutrient solution without N (Cheng et al., 2008) was added to the inoculum and incubated again at 30°C for 7 days.

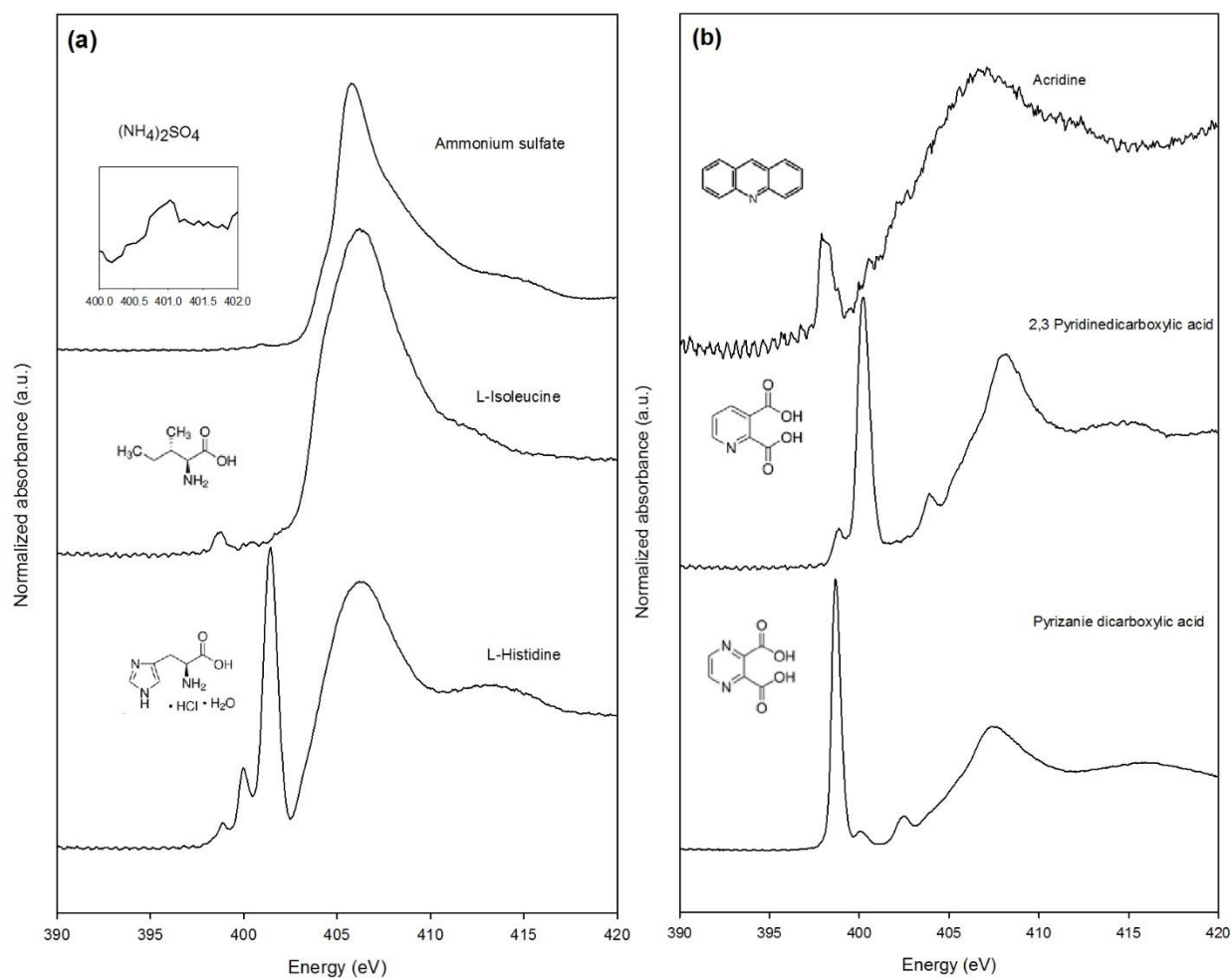


Figure B. 1: N K-edge TEY NEXAFS spectra of N standard compounds. (a) Mineral N and amino acid compounds. (b) Six-membered ring heterocycles with one or two N substitutions.

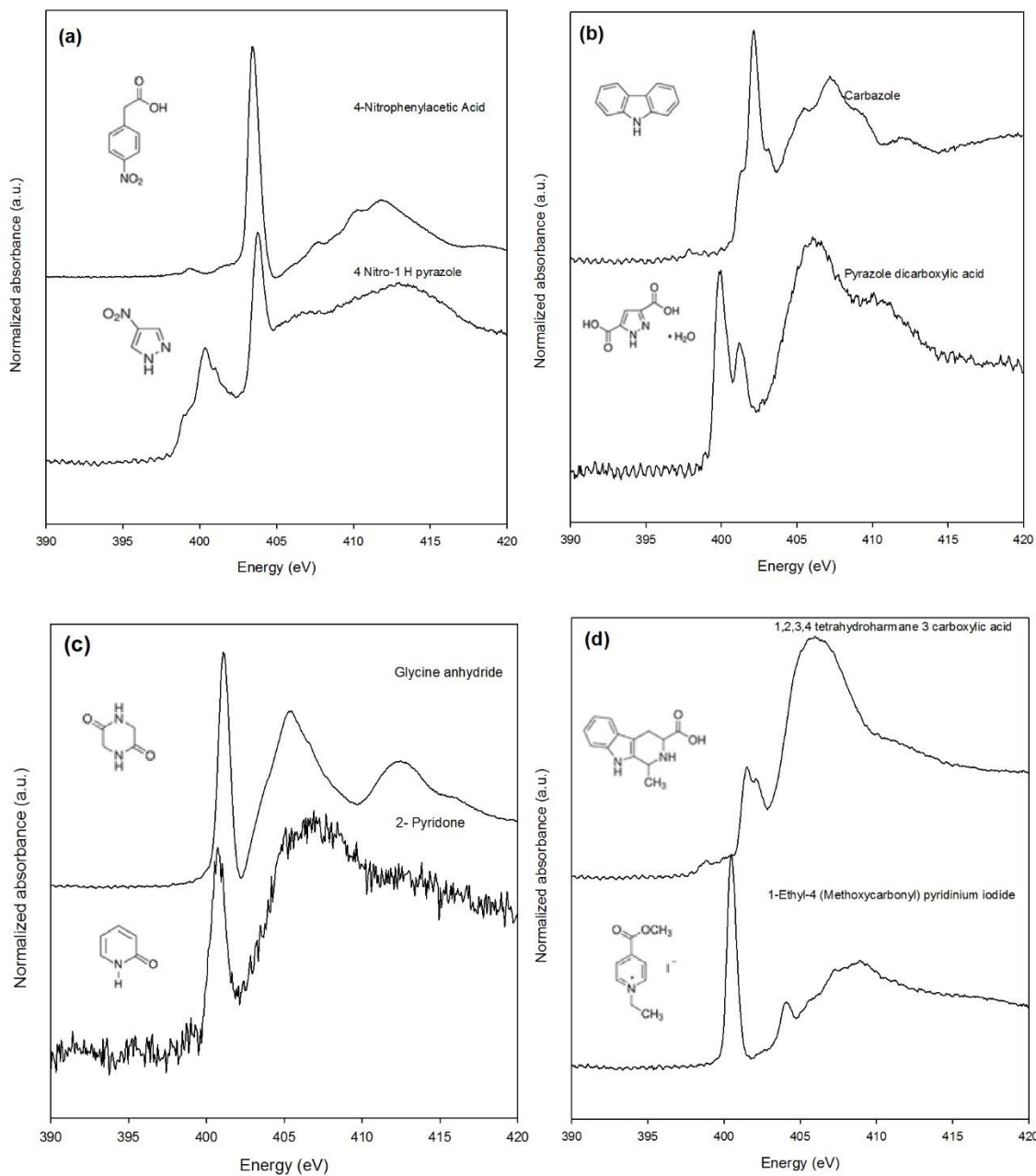


Figure B. 2: N K-edge TEY NEXAFS spectra of N standard compounds. (a) Nitro functional groups. (b) Five-membered ring heterocycles with one or two N substitutions. (c) Heterocycles with one or two keto groups attached. (d) Structure bearing five and six membered heterocyclic rings and quaternary N.

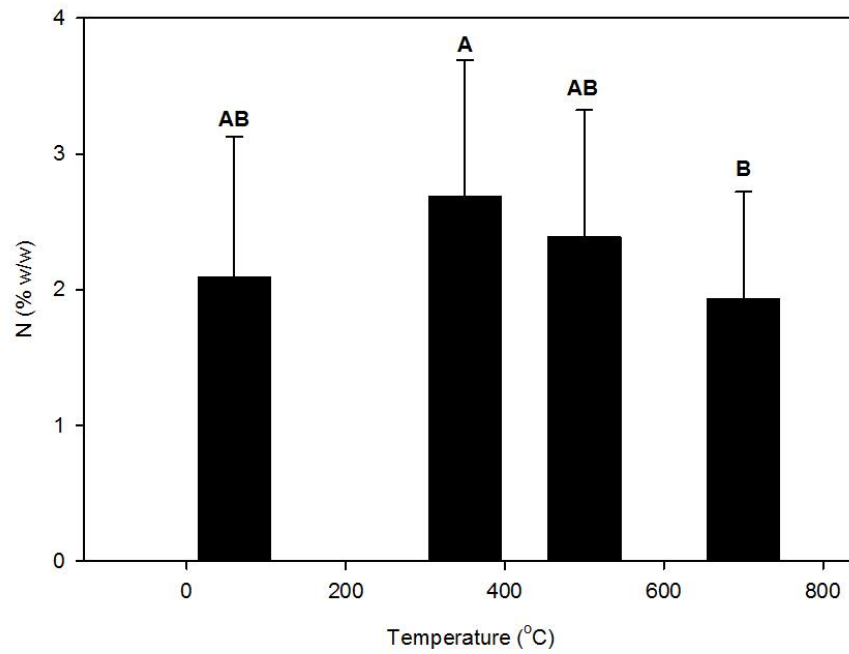


Figure B. 3: Nitrogen contents as a function of temperature for uncharred OM and PyOM for all types of studied biomass. Means and standard deviation (n=14 except for uncharred OM n=15). Different capital letters indicate significant differences ($p < 0.05$) between treatments.

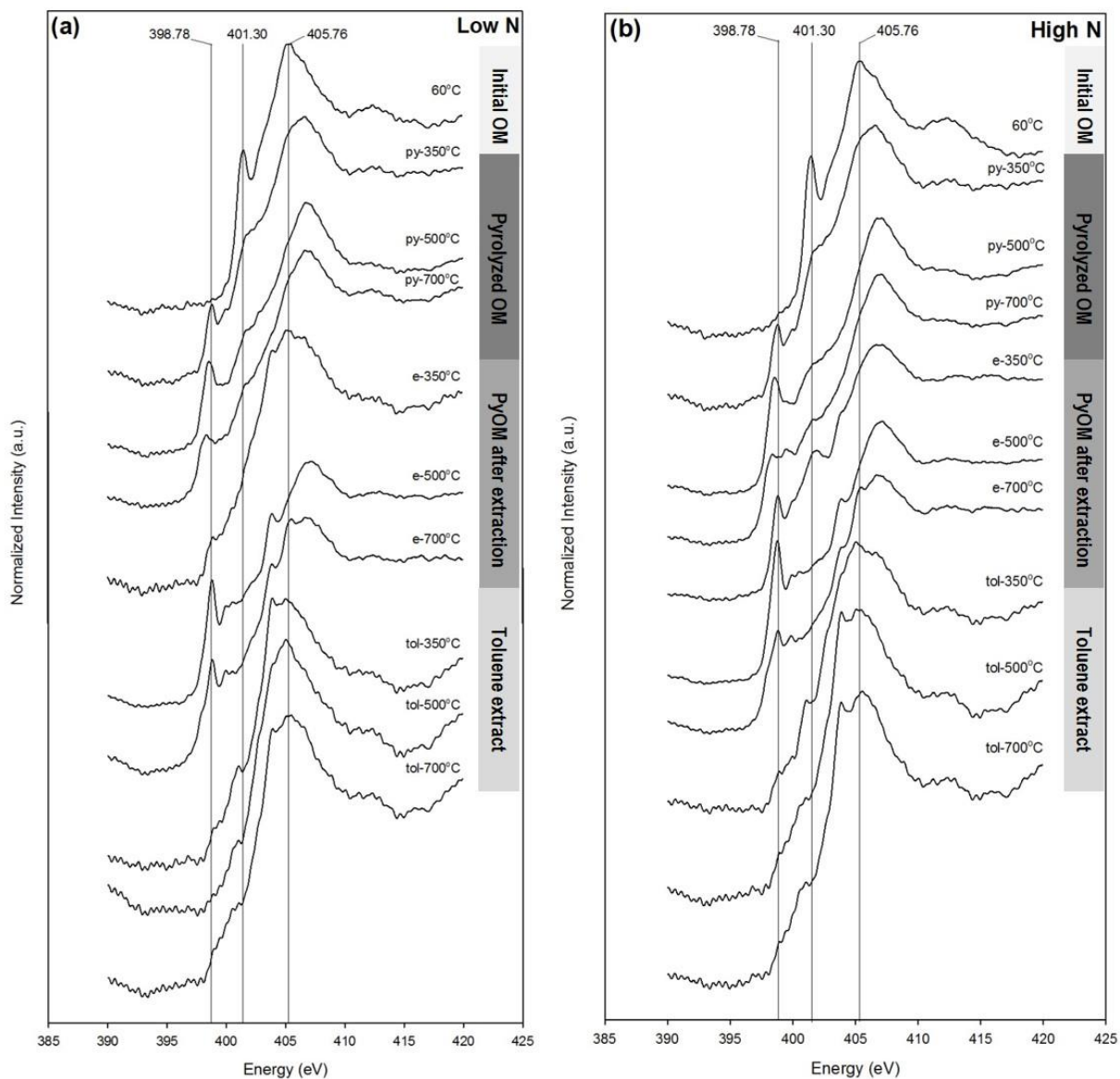


Figure B. 4: Nitrogen K-edge NEXAFS spectra of uncharred initial OM, entire PyOM (py-), extracted PyOM (e-), and the toluene extract of PyOM (tol-) as a function of pyrolysis temperature for willow leaves. (a) High N-containing willow leaves, and (b) low N-containing willow leaves. Black lines represent the peak centers associated with selected key spectral features: 398.78 eV for C=N bonds in aromatic 6-membered rings, 401.3 eV for C-N bonds in aromatic 5-membered rings, and 405.76 eV N-H bonds.

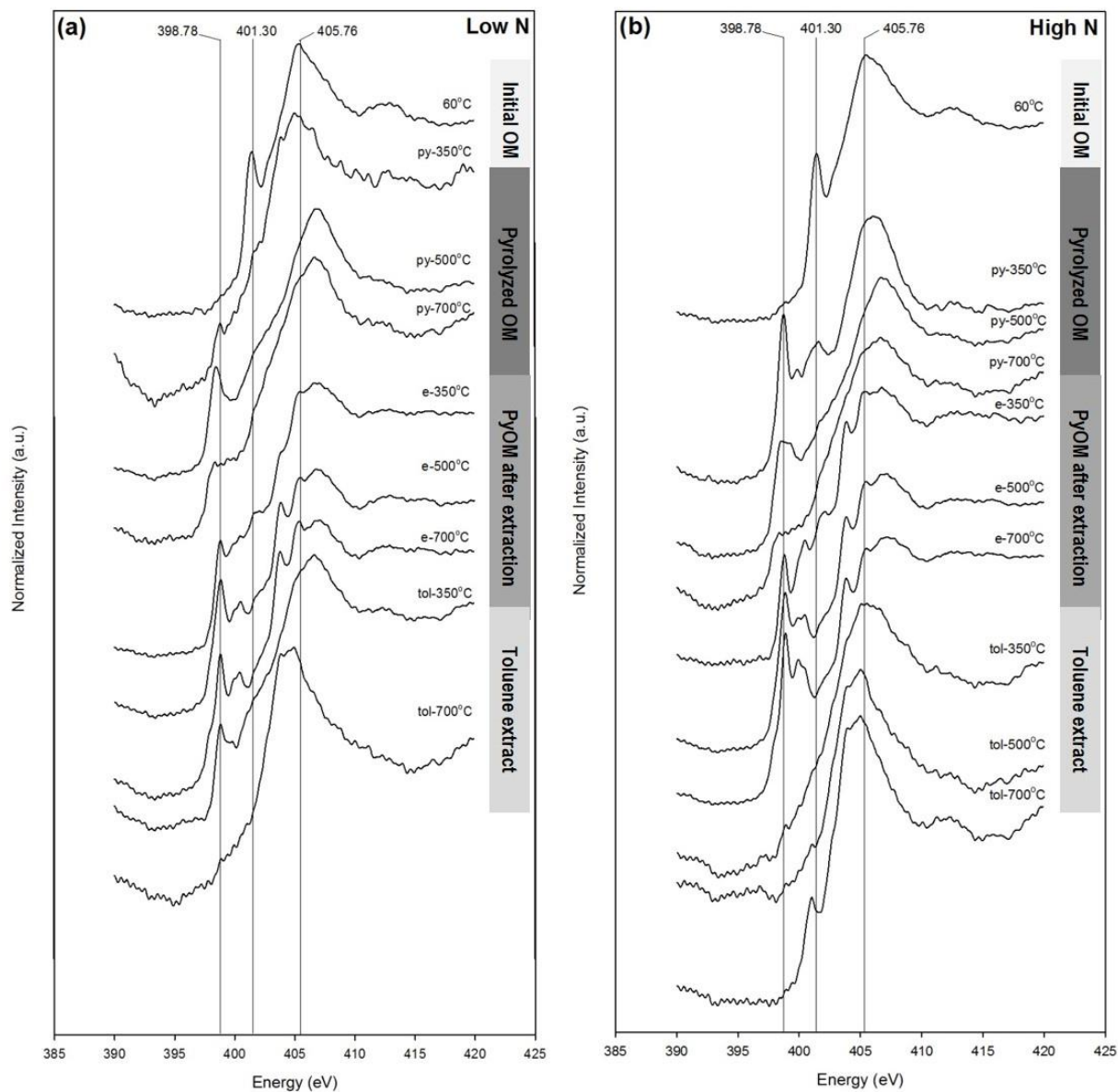


Figure B. 5: Nitrogen K-edge NEXAFS spectra of uncharred initial OM, entire PyOM (py-), extracted PyOM (e-), and the toluene extract of PyOM (tol-) as a function of pyrolysis temperature for maize stalks residues. (a) Low N-containing maize stalks residues, and (b) high N-containing maize stalks residues. Black lines represent the peak centers associated with selected key spectral features: 398.78 eV for C=N bonds in aromatic 6-membered rings, 401.3 eV for C-N bonds in aromatic 5-membered rings, and 405.76 eV N-H bonds.

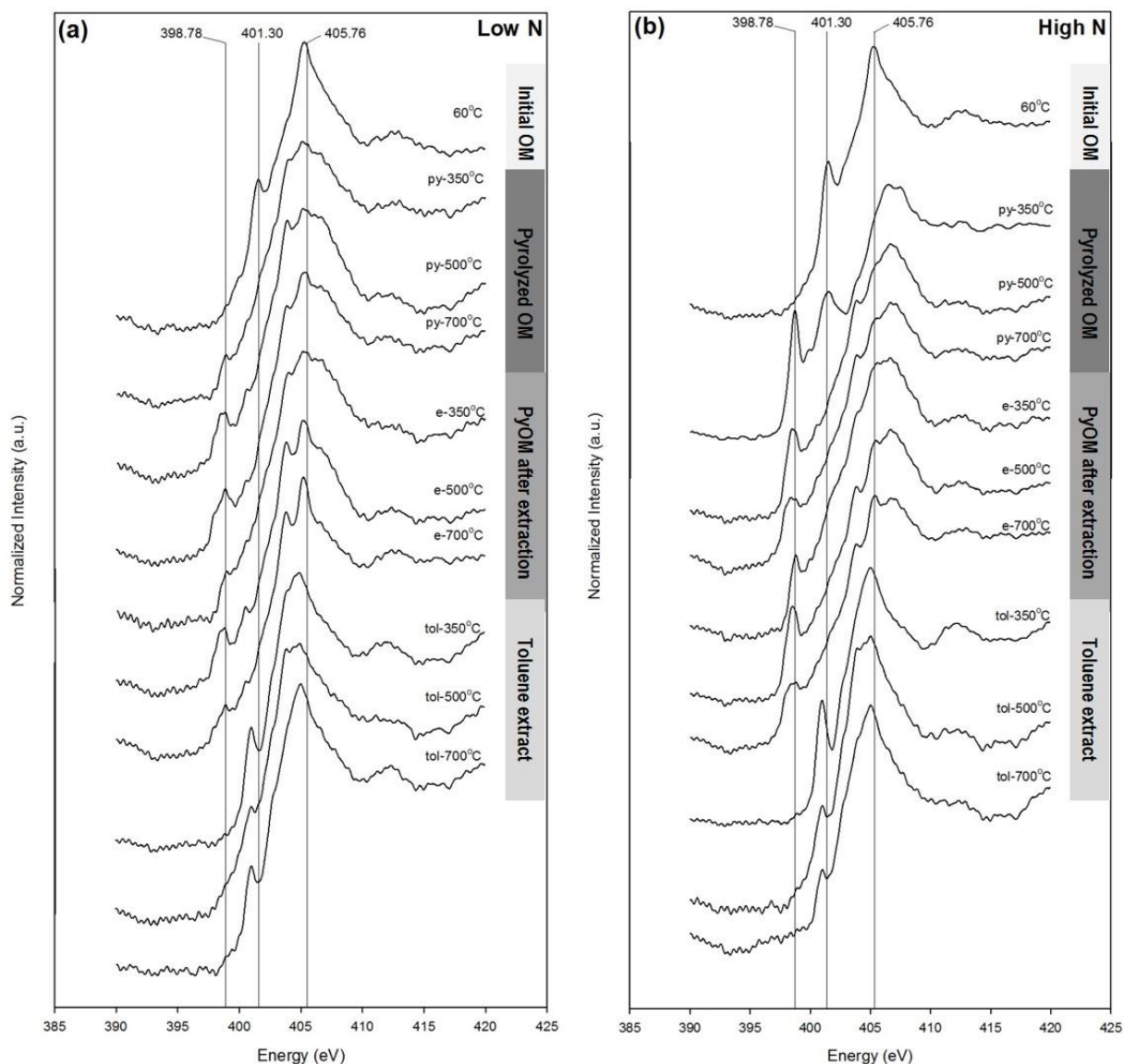


Figure B. 6: Nitrogen K-edge NEXAFS spectra of uncharred initial OM, entire PyOM (py-), extracted PyOM (e-), and the toluene extract of PyOM (tol-) as a function of pyrolysis temperature for willow wood residues. (a) Low N-containing willow wood residues, and (b) high N-containing willow wood residues. Black lines represent the peak centers associated with selected key spectral features: 398.78 eV for C=N bonds in aromatic 6-membered rings, 401.3 eV for C-N bonds in aromatic 5-membered rings, and 405.76 eV N-H bonds.

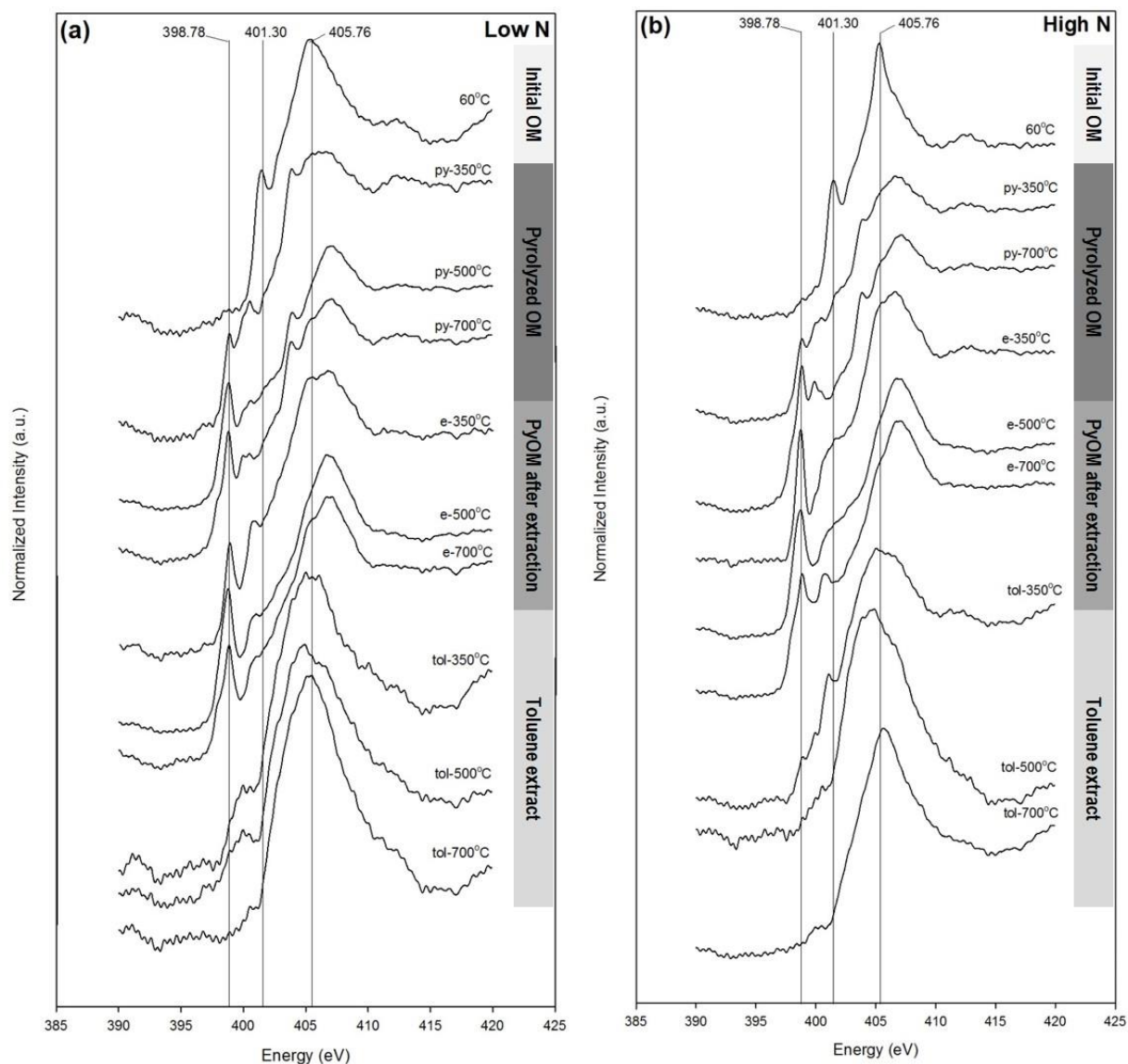


Figure B. 7: Nitrogen K-edge NEXAFS spectra of uncharred initial OM, entire PyOM (py-), extracted PyOM (e-), and the toluene extract of PyOM (tol-) as a function of pyrolysis temperature for ryegrass residues. (a) Low N-containing ryegrass residues, and (b) high N-containing ryegrass residues. Black lines represent the peak centers associated with selected key spectral features: 398.78 eV for C=N bonds in aromatic 6-membered rings, 401.3 eV for C-N bonds in aromatic 5-membered rings, and 405.76 eV N-H bonds

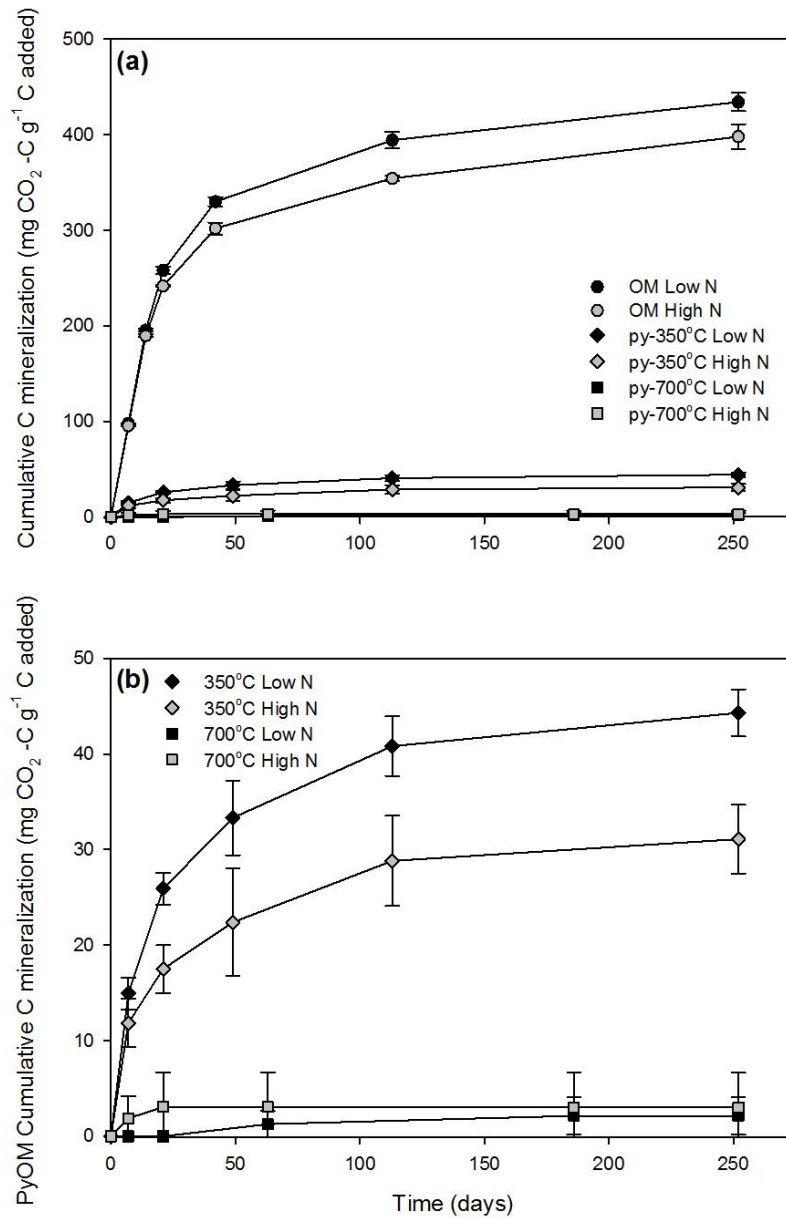


Figure B. 8: Cumulative C mineralized on the basis of per unit C added rye grass residues. (a) Cumulative C mineralization for rye grass residues dried at 60°C and PyOM pyrolyzed at 350°C and 700°C at low and high N contents, and (b) cumulative C mineralization for PyOM at 350°C and 700°C only. Black circles, diamonds and squares represent low N-containing rye grass residues, while grey circles, diamonds and squares represent high N-containing rye grass residues.

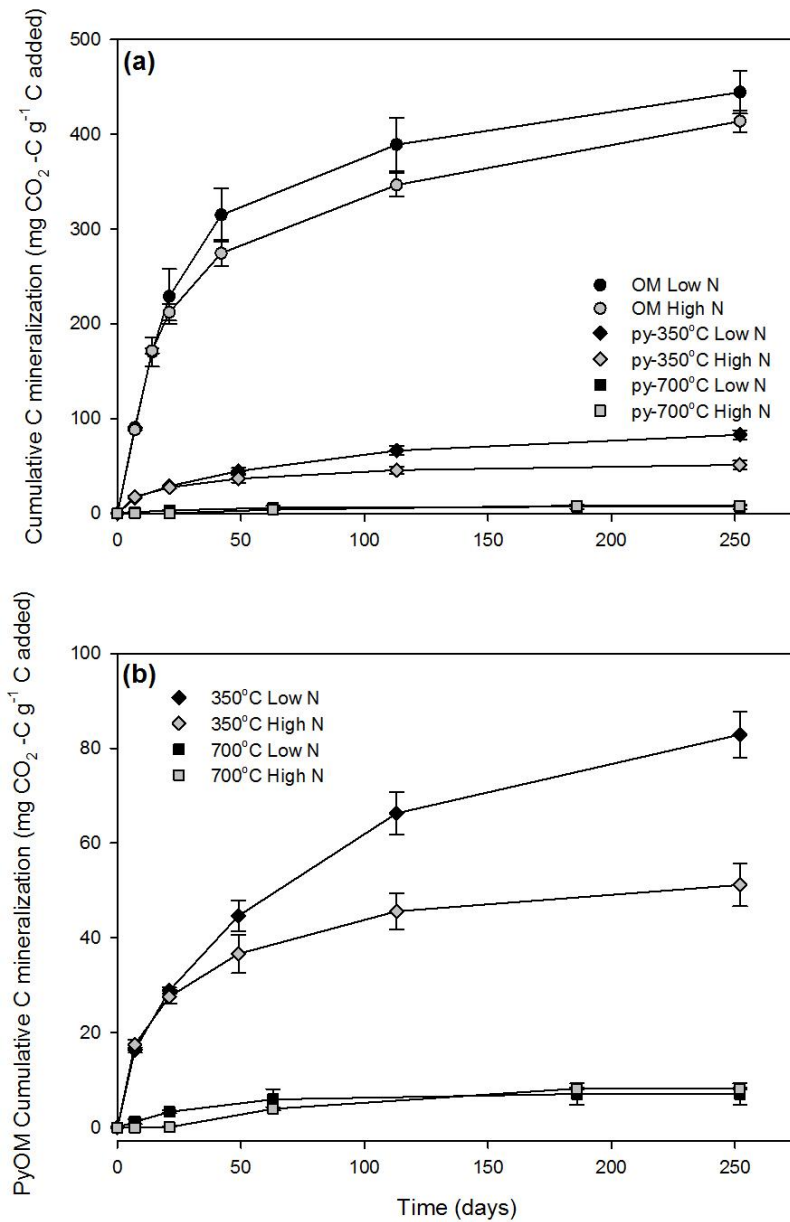


Figure B. 9: Cumulative C mineralized on the basis of per unit C added willow leaves. (a) Cumulative C mineralization over time for willow leaves dried at 60°C and PyOM pyrolyzed at 350°C and 700°C, and (b) cumulative C mineralization for PyOM at 350°C and 700°C. Black circles, diamonds and squares represent low N-content willow leaves, while grey circles, diamonds and squares represent high N-containing willow leaves.

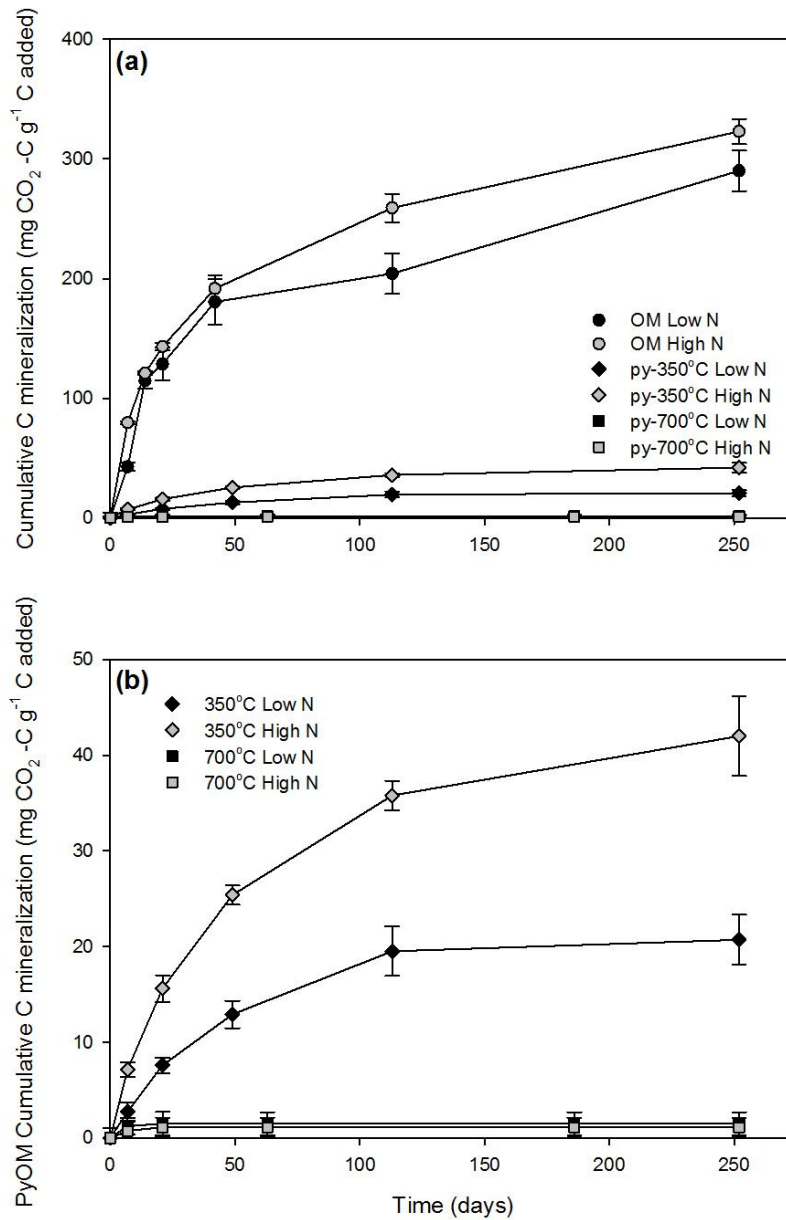


Figure B. 10: Cumulative C mineralized on the basis of per unit C added willow wood residues. (a) Cumulative C mineralization over time for willow wood residues dried at 60°C and PyOM pyrolyzed at 350°C and 700°C, and (b) cumulative C mineralization for PyOM at 350°C and 700°C. Black circles, diamonds and squares represent low N-containing willow wood residues, while grey circles, diamonds and squares represent high N-containing willow wood residues.

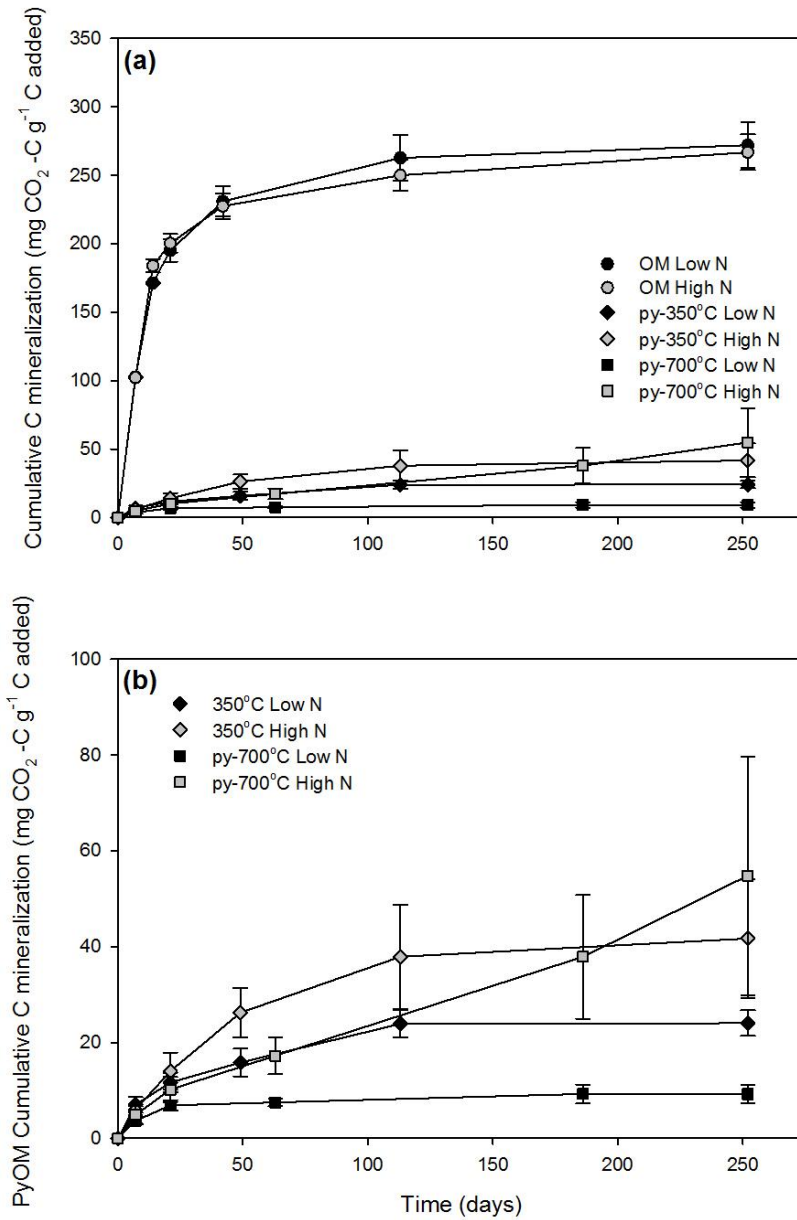


Figure B. 11: Cumulative C mineralized on the basis of per unit C added maize stover. (a) Cumulative C mineralization over time for maize stover dried at 60°C and PyOM pyrolyzed at 350°C and 700°C, and (b) cumulative C mineralization for PyOM at 350°C and 700°C. Black circles, diamonds and squares represent low N-containing maize stalks, while grey circles, diamonds and squares represent high N-containing maize stalks.

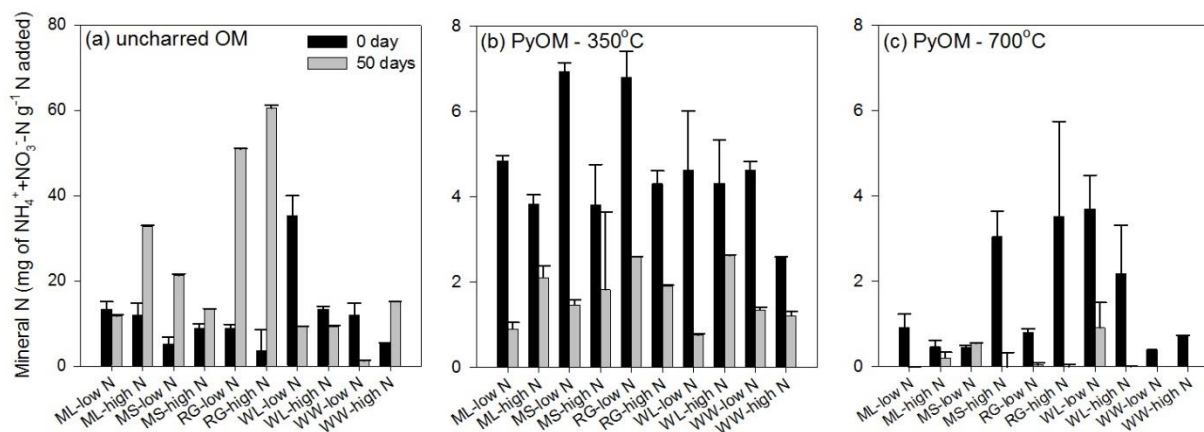


Figure B. 12: Extracted mineral N in the form of NH_4^+ and NO_3^- . (a) Nitrogen mineralization for OM with low and high N content, (b) nitrogen mineralization over time for PyOM produced at 350°C with low and high N content, and (c) nitrogen mineralization over time for PyOM produced at 700°C with low and high N content. Black vertical bars represent extractable mineral N (NH_4^+ and NO_3^-) before the incubation started, while grey vertical bars represent total extractable mineral N at day 50 of the incubation. The bars are an average of duplicates for day 0 and 4 replicates at day 50 (ML: maize leaves, MS: maize stover, RG: Ryegrass, WL: willow leaves, WW: willow wood).

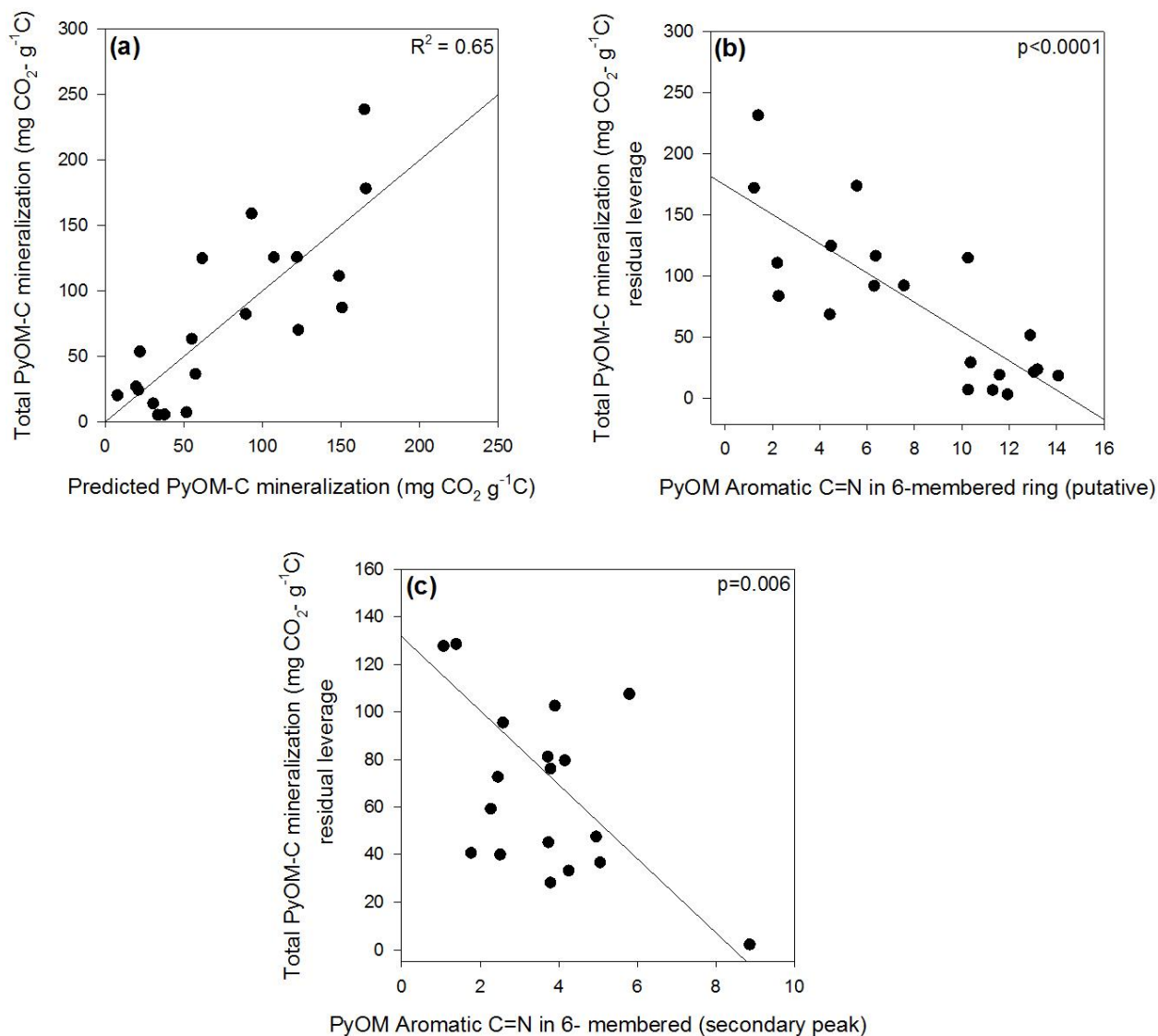


Figure B. 13: Relationship between cumulative PyOM-C mineralized and ratios of N functional groups from PyOM identified by N K-edge XANES. (a) Actual vs. predicted response values using a multiple regression model for cumulative PyOM-C mineralized, (b) relationship between cumulative PyOM-C mineralized and aromatic C=N in 6-membered rings (putative) from PyOM after extraction, and (c) relationship between cumulative PyOM-C mineralized and aromatic C=N in 6-membered rings (secondary peak).

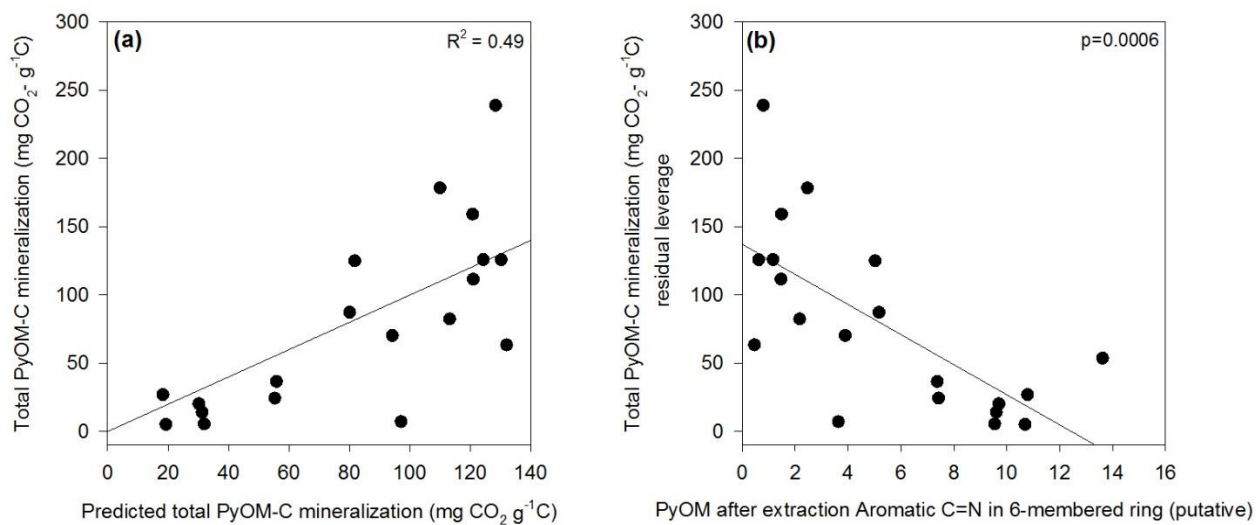


Figure B. 14: Relationship between cumulative PyOM-C mineralized and ratios of N functional groups from PyOM after extraction identified by N K-edge XANES. (a) Actual vs. predicted response values using a multiple regression model for cumulative PyOM-C mineralized, and (b) relationship between cumulative PyOM-C mineralized and aromatic C=N in 6-membered rings (putative) from PyOM after extraction.

Table B. 1: Elemental composition for OM and PyOM of all feedstocks.

Feedstock	T (°C)	Treatment					
		Low N			High N		
		Total C (mg g ⁻¹)	Total N (mg g ⁻¹)	C/N	Total C (mg g ⁻¹)	Total N (mg g ⁻¹)	C/N
Maize leaves	60	421.37	15.83	26.61	426.85	39.43	10.82
	350	539.65	22.90	23.57	510.80	42.35	12.06
	500	555.50	21.60	25.72	501.55	35.55	14.11
	700	540.20	15.20	35.54	501.40	25.95	19.32
Maize stalks	60	381.40	14.70	25.95	380.80	29.00	13.13
	350	465.40	18.95	24.56	454.45	29.25	15.54
	500	569.55	20.30	28.06	407.10	23.25	17.51
	700	480.70	23.70	20.28	460.15	18.90	24.35
Willow leaves	60	421.20	17.30	24.35	440.20	38.30	11.49
	350	553.10	25.20	21.95	561.30	44.95	12.49
	500	541.60	22.90	23.65	437.90	34.90	12.55
	700	577.40	19.95	28.94	587.60	35.85	16.39
Willow wood	60	450.80	3.30	136.61	446.30	11.90	37.50
	350	707.20	6.55	107.97	682.80	20.85	32.75
	500	765.05	4.40	173.88	749.85	18.85	39.78
	700	808.00	4.80	168.33	755.05	14.95	50.51
Ryegrass	60	397.50	16.00	24.84	409.50	21.60	18.96
	350	503.05	21.30	23.62	543.55	31.50	17.26
	500	515.00	20.30	25.37	547.00	29.50	18.54
	700	461.25	12.95	35.62	551.90	21.75	25.37

Table B. 2: pH and inorganic NH₄-N and NO₃-N concentrations for OM and PyOM of all feedstocks.

Feedstock	T (°C)	Treatment					
		Low N			High N		
		NH ₄ -N (mg g ⁻¹)	NO ₃ -N (mg g ⁻¹)	pH	NH ₄ -N (mg g ⁻¹)	NO ₃ -N (mg g ⁻¹)	pH
Maize leaves	60	9.42	0.33	5.04	4.60	1.33	9.42
	350	4.80	0.05	6.92	3.58	0.26	8.40
	700	0.79	0.12	9.42	0.44	0.02	9.40
Maize stalks	60	13.62	0.50	5.86	21.28	8.91	6.00
	350	6.83	0.11	7.12	3.64	0.16	8.40
	700	0.45	0.01	9.31	2.57	0.47	9.45
Willow leaves	60	11.78	0.24	5.23	4.80	0.38	5.32
	350	4.39	0.24	7.16	6.96	0.16	7.62
	700	0.40	0.00	9.85	0.70	0.00	10.12
Willow wood	60	33.31	2.02	5.18	12.68	0.67	5.33
	350	4.39	0.24	6.08	6.96	0.16	6.64
	700	2.63	1.06	8.93	1.81	0.38	9.19
Ryegrass	60	8.94	0.00	6.11	3.47	0.12	5.91
	350	6.73	0.08	7.07	4.25	0.05	7.07
	700	0.66	0.13	9.82	3.37	0.14	9.57

Table B. 3: Major features of TEY N K-edge NEXAFS spectra collected from N standard compounds. Peak centers and half widths at half maximum (hwhm) are shown in eV.

Standard compound	$1s \rightarrow \pi^*$	hwhm	$1s \rightarrow \pi^*$	hwhm	$1s \rightarrow \pi^*$	hwhm	$1s \rightarrow \sigma^*$	hwhm	$1s \rightarrow \sigma^*$	hwhm
Acridine	398.10	0.42					406.98	2.41		
2,3-Pyrazinedicarboxylic acid	398.72	0.30	400.25	0.41	402.48	0.37	407.50	1.48		
2,3-Pyridinedicarboxylic acid	398.89	0.33	400.04	0.61	402.47	1.60	403.88	0.47	408.12	1.24
2-Pyrimidinecarbonitrile	398.80	0.40	400.00	0.40	402.60	0.40	404.50	2.00	408.60	2.00
Cytosine	399.20	0.40	400.60	0.40	403.00	0.40	405.00	2.00	408.40	2.00
3,5-Pyrazoledicarboxylic acid	399.90	0.41	401.18	0.68			406.04	1.70	410.37	2.38
L-Histidine	399.97	0.40	401.41	0.51			406.25	1.95	412.82	3.06
4-Nitro-1H-pyrazole	400.35	0.40	401.02	0.50	403.79	0.37	412.77	3.77		
1-Ethyl-4-(methoxycarbonyl)-pyridinium iodide	400.49	0.36			404.04	0.36	408.36	2.05		
2-Pyridone	400.74	0.54					406.92	2.05		
Glycine anhydride	401.12	0.42					405.39	1.76	412.40	2.39
Carbazole	402.13	0.37					407.19	1.87		
4-Nitro-phenylacetic acid	403.44	0.43					411.78	2.48		
Ammonium sulfate							405.76	1.37		
L-Isoleucine							406.10	1.83		

Table B. 4: N K-edge NEXAFS TEY peak assignments used in deconvolution model.

N form	Bond	Peak Energy (eV) $1s \rightarrow \pi^*$	Fit position	Peak Energy (eV) $1s \rightarrow \sigma^*$
Aromatic C=N in 6-membered ring (putative)	C=N	398.1	398.1	
Aromatic C=N in 6-membered ring (1&2N)	C=N	398.70-398.89	398.78	407.80
Aromatic C=N in 6-membered oxygenated ring (2N)	C=N	399.4	399.4	
Aromatic C=N in 5-membered ring (2N)	C=N	399.90-399.97	399.93	406.14, 410.37, 412.82
Nitrile	C \equiv N	400	400.00	404.5, 408.6
Quaternary C-N in 6-membered ring	C-N	400.49	400.49	408.36
Aromatic C-N in 6-membered oxygenated ring (2N)	C-N	400.74	400.74	406.92
Non-aromatic C-N in 6-membered oxygenated ring (2N)	C-N	401.12	401.12	405.39, 412.4
Aromatic C-N in 5-membered ring (2N)	C-N	401.18-401.41	401.30	406.14, 410.37, 412.82
Aromatic C-N in 5-membered ring (1N)	C-N	402.13	402.13	407.19
Aromatic C=N in 6-membered ring (1&2N, secondary peak)	C=N	402.48-402.60	402.54	408.05
Aliphatic C-NH ₂ bonded to aromatic 6-membered ring	C-NH ₂	403	403	
Nitro C-NO ₂ bonded to aromatic 6-membered ring	C-NO ₂	403.44-403.79	403.61	412.28
Aromatic N secondary peak	C=N	403.86-404.04	403.95	408.24
Inorganic N-H	N-H			405.76
Aliphatic C-NH ₂	C-NH ₂			406.10

Median values were calculated for N structures represented in more than one standard compound, which constituted the designated fit position used in the final model. The peak centered at 398.10 eV is not associated with a specific standard compound, but was identified by deconvolution of PyOM spectra and is closest in position to spectral features associated with aromatic 6-membered rings.

Table B. 5: Proportion of absorption area (%) of N bonds measured with N K-edge NEXAFS for maize leaf OM and PyOM components.

				Low N									
N Form	Bond	Peak Energy (eV)	Transition	OM-60	py-350	py-500	py-700	e-350	e-500	e-700	tol-350	tol-500	tol-700
Aromatic C=N in 6-membered ring (putative)	C=N	398.10	1s → π*		4.76	8.20	13.88	5.50	9.59	12.82	0.00	0.00	0.00
Aromatic C=N in 6-membered ring (1&2N)	C=N	398.78	1s → π*		11.94	17.52	6.68	15.25	16.97	7.68	0.00	0.00	0.00
Aromatic C=N in 6-membered oxygenated ring (2N)	C=N	399.40	1s → π*		3.76	0.90	5.65	0.00	0.90	12.63	1.70	1.79	4.44
Aromatic C=N in 5-membered ring (2N)	C=N	399.93	1s → π*		9.04	9.85	5.19	12.44	9.37	0.52	2.05	1.24	3.29
Nitrile	C≡N	400.00	1s → π*		0.00	0.00	0.00	0.00	0.00	2.02	0.00	0.00	0.00
Quaternary C-N in 6-membered ring	C-N	400.49	1s → π*		2.40	1.39	6.90	1.13	1.81	5.83	0.00	0.00	7.92
Aromatic C-N in 6-membered oxygenated ring (2N)	C-N	400.74	1s → π*		4.74	3.48	1.50	4.67	4.10	6.74	13.18	13.76	3.99
Non-aromatic C-N in 6-membered oxygenated ring (2N)	C-N	401.12	1s → π*		0.00	0.00	0.00	0.00	0.00	0.00	0.00	0.00	0.00
Aromatic C-N in 5-membered ring (2N)	C-N	401.30	1s → π*	38.76	19.20	18.63	16.94	21.05	16.83	15.00	15.68	21.49	8.20
Aromatic C-N in 5-membered ring (1N)	C-N	402.13	1s → π*	25.09	19.13	14.54	15.82	16.77	13.59	11.87	15.45	11.16	19.21
Aromatic C=N in 6-membered ring (1&2N, secondary peak)	C=N	402.54	1s → π*	5.06	2.85	3.36	4.17	3.65	2.97	3.72	10.41	7.86	11.73
Aliphatic C-NH ₂ bonded to aromatic 6-membered ring	C-NH ₂	403.00	1s → π*	16.70	12.00	11.52	11.76	7.31	10.94	9.21	19.23	23.67	19.27
Nitro C-NO ₂ bonded to aromatic ring A15	C-NO ₂	403.62	1s → π*	12.31	7.11	7.97	8.81	8.44	8.06	7.89	15.22	12.92	15.05
Aromatic N secondary peak	C=N	403.95	1s → π*	2.08	3.08	2.66	2.70	3.78	4.89	4.07	7.09	6.10	6.90
				Mid N									
N Form	Bond	Peak Energy (eV)	Transition	OM-60	py-350	py-500	py-700	e-350	e-500	e-700	tol-350	tol-500	tol-700
Aromatic C=N in 6-membered ring (putative)	C=N	398.10	1s → π*		7.48	8.55	15.81	1.40	8.47	13.04	0.55	0.00	0.00
Aromatic C=N in 6-membered ring (1&2N)	C=N	398.78	1s → π*		18.84	18.76	6.57	6.74	17.27	6.47	7.04	0.00	0.00
Aromatic C=N in 6-membered oxygenated ring (2N)	C=N	399.40	1s → π*		12.68	1.32	6.72	4.22	1.64	14.51	3.82	1.39	0.00
Aromatic C=N in 5-membered ring (2N)	C=N	399.93	1s → π*		0.00	10.45	5.62	5.00	10.83	1.12	5.22	1.65	7.35
Nitrile	C≡N	400.00	1s → π*		0.00	0.00	0.00	0.00	0.00	0.00	0.00	0.00	0.00
Quaternary C-N in 6-membered ring	C-N	400.49	1s → π*		0.86	1.57	5.52	2.03	2.59	6.83	1.22	15.24	16.43
Aromatic C-N in 6-membered oxygenated ring (2N)	C-N	400.74	1s → π*		4.50	4.11	3.47	8.17	3.75	3.43	8.71	1.23	2.03
Non-aromatic C-N in 6-membered oxygenated ring (2N)	C-N	401.12	1s → π*		0.00	0.00	0.00	0.00	0.00	0.00	0.00	0.00	0.00
Aromatic C-N in 5-membered ring (2N)	C-N	401.30	1s → π*	40.41	22.59	17.38	14.90	20.01	16.12	16.10	20.29	12.16	12.78
Aromatic C-N in 5-membered ring (1N)	C-N	402.13	1s → π*	29.87	16.67	14.32	15.85	13.96	14.65	12.51	13.62	20.06	12.89
Aromatic C=N in 6-membered ring (1&2N, secondary peak)	C=N	402.54	1s → π*	1.31	3.86	3.06	4.06	6.18	1.86	5.24	6.97	9.10	12.87
Aliphatic C-NH ₂ bonded to aromatic 6-membered ring	C-NH ₂	403.00	1s → π*	16.30	6.81	10.90	10.23	15.05	10.61	11.32	14.33	17.22	14.39
Nitro C-NO ₂ bonded to aromatic ring	C-NO ₂	403.62	1s → π*	12.11	4.53	7.31	8.34	12.94	8.59	7.52	13.25	20.83	18.33
Aromatic N secondary peak	C=N	403.95	1s → π*	0.00	1.19	2.27	2.92	4.30	3.62	1.91	4.97	1.12	2.94
				High N									
N Form	Bond	Peak Energy (eV)	Transition	OM-60	py-350	py-500	py-700	e-350	e-500	e-700	tol-350	tol-500	tol-700
Aromatic C=N in 6-membered ring (putative)	C=N	398.10	1s → π*		3.00	8.50	13.31	5.81	8.86	13.90	0.00	0.00	0.00
Aromatic C=N in 6-membered ring (1&2N)	C=N	398.78	1s → π*		17.29	19.19	8.83	16.35	18.99	5.78	2.90	0.00	0.00
Aromatic C=N in 6-membered oxygenated ring (2N)	C=N	399.40	1s → π*		1.51	1.59	6.30	0.17	0.22	14.56	3.85	0.00	1.87
Aromatic C=N in 5-membered ring (2N)	C=N	399.93	1s → π*		15.20	9.66	6.36	13.30	11.99	1.92	0.53	4.22	5.37
Nitrile	C≡N	400.00	1s → π*		0.00	0.00	0.00	0.00	0.00	0.00	5.55	0.00	0.00
Quaternary C-N in 6-membered ring	C-N	400.49	1s → π*		0.56	2.58	5.40	1.23	1.11	6.72	0.27	0.00	6.14
Aromatic C-N in 6-membered oxygenated ring (2N)	C-N	400.74	1s → π*		3.45	3.62	2.14	3.64	3.18	4.23	10.01	9.43	2.28
Non-aromatic C-N in 6-membered oxygenated ring (2N)	C-N	401.12	1s → π*		0.00	0.00	0.00	0.00	0.00	0.00	0.00	0.00	0.00
Aromatic C-N in 5-membered ring (2N)	C-N	401.30	1s → π*	46.14	21.43	16.49	16.89	18.16	17.83	15.92	16.55	20.86	13.25
Aromatic C-N in 5-membered ring (1N)	C-N	402.13	1s → π*	20.90	14.85	13.71	15.18	14.19	12.29	12.97	16.81	10.21	23.44
Aromatic C=N in 6-membered ring (1&2N, secondary peak)	C=N	402.54	1s → π*	1.80	4.04	3.48	2.94	5.05	2.65	3.27	10.30	15.36	12.36
Aliphatic C-NH ₂ bonded to aromatic 6-membered ring	C-NH ₂	403.00	1s → π*	21.95	9.59	10.26	9.15	10.86	11.47	10.79	11.39	16.38	13.69
Nitro C-NO ₂ bonded to aromatic ring	C-NO ₂	403.62	1s → π*	6.95	6.42	8.12	10.50	8.40	7.73	9.22	15.79	18.32	18.12
Aromatic N secondary peak	C=N	403.95	1s → π*	2.26	2.65	2.79	2.99	2.82	3.67	0.70	6.04	5.22	3.47

Deconvolution of NEXAFS spectra collected from OM, PyOM, e-PyOM and tol-PyOM. PyOM was used to determine the π area represented by different N bonds. Proportions of areas were only calculated for π bonds because of the high degree of peak overlap in the σ region.

Table B. 6: Proportion of absorption regions (%) of N bonds measured with N K-edge NEXAFS for maize stover OM and PyOM components.

				Low N									
N Form	Bond	Peak Energy (eV)	Transition	OM-60	py-350	py-500	py-700	e-350	e-500	e-700	tol-350	tol-500	tol-700
Aromatic C=N in 6-membered ring (putative)	C=N	398.10	1s → π*		4.27	10.83	11.93	3.15	7.63	11.34	1.73	n/a	3.86
Aromatic C=N in 6-membered ring (1&2N)	C=N	398.78	1s → π*		8.20	18.93	6.31	13.10	14.80	8.02	14.30	n/a	4.16
Aromatic C=N in 6-membered oxygenated ring (2N)	C=N	399.40	1s → π*		4.13	1.36	8.67	7.27	8.12	15.94	7.29	n/a	9.25
Aromatic C=N in 5-membered ring (2N)	C=N	399.93	1s → π*		7.86	9.82	5.55	10.13	6.36	4.28	8.91	n/a	1.96
Nitrile	C≡N	400.00	1s → π*		0.00	0.00	0.00	0.00	0.00	2.02	0.00	n/a	4.49
Quaternary C-N in 6-membered ring	C-N	400.49	1s → π*		5.77	2.03	6.50	6.94	7.57	6.20	2.37	n/a	2.43
Aromatic C-N in 6-membered oxygenated ring (2N)	C-N	400.74	1s → π*	0.00	1.64	4.07	0.00	1.95	3.06	3.81	5.46	n/a	7.00
Non-aromatic C-N in 6-membered oxygenated ring (2N)	C-N	401.12	1s → π*	0.00	0.00	0.00	0.00	0.00	0.00	0.00	0.00	n/a	0.00
Aromatic C-N in 5-membered ring (2N)	C-N	401.30	1s → π*	41.99	17.72	16.77	16.87	19.72	12.87	13.10	19.60	n/a	11.77
Aromatic C-N in 5-membered ring (1N)	C-N	402.13	1s → π*	26.61	18.90	15.28	16.86	15.38	13.84	10.66	16.10	n/a	10.21
Aromatic C=N in 6-membered ring (1&2N, secondary peak)	C=N	402.54	1s → π*	5.99	3.73	1.58	3.81	0.90	0.30	1.10	3.36	n/a	5.81
Aliphatic C-NH ₂ bonded to aromatic 6-membered ring	C-NH ₂	403.00	1s → π*	13.19	10.91	11.06	12.15	12.40	13.49	11.80	9.88	n/a	11.56
Nitro C-NO ₂ bonded to aromatic ring	C-NO ₂	403.62	1s → π*	12.23	11.26	7.82	9.58	7.58	8.27	9.72	8.79	n/a	13.64
Aromatic N secondary peak	C=N	403.95	1s → π*	0.00	5.61	0.46	1.77	1.47	3.68	4.03	2.20	n/a	13.87
				Mid N									
N Form	Bond	Peak Energy (eV)	Transition	OM-60	py-350	py-500	py-700	e-350	e-500	e-700	tol-350	tol-500	tol-700
Aromatic C=N in 6-membered ring (putative)	C=N	398.10	1s → π*		n/a	8.66	n/a	4.67	6.89	7.83	2.29	0.00	0.00
Aromatic C=N in 6-membered ring (1&2N)	C=N	398.78	1s → π*		n/a	17.94	n/a	14.76	7.72	6.91	9.69	0.00	0.00
Aromatic C=N in 6-membered oxygenated ring (2N)	C=N	399.40	1s → π*		n/a	4.47	n/a	0.79	21.01	14.61	7.42	4.22	0.00
Aromatic C=N in 5-membered ring (2N)	C=N	399.93	1s → π*		n/a	9.52	n/a	16.30	5.24	1.33	7.49	0.00	0.00
Nitrile	C≡N	400.00	1s → π*		n/a	0.00	n/a	0.00	0.00	3.57	0.00	0.00	0.00
Quaternary C-N in 6-membered ring	C-N	400.49	1s → π*		n/a	4.67	n/a	3.55	9.51	7.49	0.00	1.42	0.00
Aromatic C-N in 6-membered oxygenated ring (2N)	C-N	400.74	1s → π*	0.00	n/a	1.53	n/a	3.01	0.00	0.00	4.26	2.83	0.00
Non-aromatic C-N in 6-membered oxygenated ring (2N)	C-N	401.12	1s → π*	0.00	n/a	0.00	n/a	0.00	0.00	0.00	0.00	0.00	0.00
Aromatic C-N in 5-membered ring (2N)	C-N	401.30	1s → π*	40.41	n/a	15.60	n/a	19.57	11.89	13.84	5.19	9.12	13.27
Aromatic C-N in 5-membered ring (1N)	C-N	402.13	1s → π*	23.61	n/a	15.84	n/a	16.90	13.34	11.59	21.18	18.55	25.49
Aromatic C=N in 6-membered ring (1&2N, secondary peak)	C=N	402.54	1s → π*	3.08	n/a	2.71	n/a	0.00	0.42	3.34	16.92	15.56	15.84
Aliphatic C-NH ₂ bonded to aromatic 6-membered ring	C-NH ₂	403.00	1s → π*	20.58	n/a	8.33	n/a	9.96	15.19	14.22	3.54	9.01	6.69
Nitro C-NO ₂ bonded to aromatic ring	C-NO ₂	403.62	1s → π*	9.00	n/a	10.02	n/a	8.49	7.44	11.56	12.25	22.80	27.71
Aromatic N secondary peak	C=N	403.95	1s → π*	3.32	n/a	0.71	n/a	1.99	1.34	3.69	9.79	16.49	11.00
				High N									
N Form	Bond	Peak Energy (eV)	Transition	OM-60	py-350	py-500	py-700	e-350	e-500	e-700	tol-350	tol-500	tol-700
Aromatic C=N in 6-membered ring (putative)	C=N	398.10	1s → π*		8.32	7.66	12.42	1.81	7.04	9.35	1.56	0.00	0.00
Aromatic C=N in 6-membered ring (1&2N)	C=N	398.78	1s → π*		22.50	17.68	4.79	15.27	12.23	8.83	4.65	0.00	0.00
Aromatic C=N in 6-membered oxygenated ring (2N)	C=N	399.40	1s → π*		0.76	3.92	9.15	1.82	12.33	17.62	4.54	4.15	2.25
Aromatic C=N in 5-membered ring (2N)	C=N	399.93	1s → π*		16.77	8.27	4.65	12.31	7.86	1.39	5.81	0.00	0.00
Nitrile	C≡N	400.00	1s → π*		0.00	0.00	0.00	0.00	0.00	4.96	0.00	4.10	2.20
Quaternary C-N in 6-membered ring	C-N	400.49	1s → π*		1.08	5.13	5.79	6.88	5.54	5.33	3.05	1.10	0.44
Aromatic C-N in 6-membered oxygenated ring (2N)	C-N	400.74	1s → π*	2.56	4.66	1.79	1.78	0.00	4.81	4.74	5.78	12.04	13.11
Non-aromatic C-N in 6-membered oxygenated ring (2N)	C-N	401.12	1s → π*	0.00	0.00	0.00	0.00	0.00	0.00	0.00	0.00	0.00	0.00
Aromatic C-N in 5-membered ring (2N)	C-N	401.30	1s → π*	42.02	19.79	16.77	15.95	21.52	12.36	12.51	18.37	14.18	22.31
Aromatic C-N in 5-membered ring (1N)	C-N	402.13	1s → π*	21.01	11.58	14.67	17.37	12.63	10.06	10.27	15.27	8.34	9.27
Aromatic C=N in 6-membered ring (1&2N, secondary peak)	C=N	402.54	1s → π*	2.79	1.31	2.73	4.57	0.83	6.10	1.29	7.89	7.88	7.41
Aliphatic C-NH ₂ bonded to aromatic 6-membered ring	C-NH ₂	403.00	1s → π*	20.05	7.47	10.26	8.88	13.16	5.81	10.47	14.39	21.96	18.77
Nitro C-NO ₂ bonded to aromatic ring	C-NO ₂	403.62	1s → π*	9.62	4.41	8.77	13.52	9.20	13.20	8.77	12.42	19.35	12.49
Aromatic N secondary peak	C=N	403.95	1s → π*	1.94	1.34	2.35	1.13	4.58	2.66	4.46	6.27	6.90	11.75

Table B. 7: Proportion of absorption regions (%) of N bonds measured with N K-edge NEXAFS for ryegrass OM and PyOM components.

				Low N									
N Form	Bond	Peak Energy (eV)	Transition	OM-60	py-350	py-500	py-700	e-350	e-500	e-700	tol-350	tol-500	tol-700
Aromatic C=N in 6-membered ring (putative)	C=N	398.10	1s→π*		2.45	8.13	11.03	2.31	7.66	9.75	0.00	5.67	0.00
Aromatic C=N in 6-membered ring (1&2N)	C=N	398.78	1s→π*		10.11	14.67	6.81	8.07	15.51	6.37	4.86	7.17	0.00
Aromatic C=N in 6-membered oxygenated ring (2N)	C=N	399.40	1s→π*		8.11	2.98	13.14	6.08	5.23	11.30	7.41	10.31	1.39
Aromatic C=N in 5-membered ring (2N)	C=N	399.93	1s→π*		8.20	10.05	3.17	1.43	4.98	0.74	6.88	6.36	2.55
Nitrile	C≡N	400.00	1s→π*		0.00	0.00	0.00	8.26	3.15	4.70	0.00	4.58	0.00
Quaternary C-N in 6-membered ring	C-N	400.49	1s→π*		8.69	2.72	9.31	3.06	5.84	4.11	6.40	3.85	7.58
Aromatic C-N in 6-membered oxygenated ring (2N)	C-N	400.74	1s→π*		3.60	5.87	0.45	11.74	14.16	12.96	3.17	3.68	1.50
Non-aromatic C-N in 6-membered oxygenated ring (2N)	C-N	401.12	1s→π*		0.00	0.00	0.00	0.00	0.00	0.00	0.00	0.00	0.00
Aromatic C-N in 5-membered ring (2N)	C-N	401.30	1s→π*	39.93	14.12	13.51	13.90	12.53	11.21	10.91	11.06	2.19	0.00
Aromatic C-N in 5-membered ring (1N)	C-N	402.13	1s→π*	21.88	13.43	10.54	13.81	2.54	3.54	3.19	19.13	14.92	21.64
Aromatic C=N in 6-membered ring (1&2N, secondary peak)	C=N	402.54	1s→π*	2.67	2.76	9.47	1.26	6.96	8.56	10.36	9.16	10.48	14.26
Aliphatic C-NH ₂ bonded to aromatic 6-membered ring	C-NH ₂	403.00	1s→π*	25.28	9.90	3.34	14.11	6.49	6.94	5.93	11.60	8.50	27.34
Nitro C-NO ₂ bonded to aromatic ring	C-NO ₂	403.62	1s→π*	7.48	11.84	14.82	9.27	1.59	2.25	0.90	9.15	6.54	16.23
Aromatic N secondary peak	C=N	403.95	1s→π*	2.76	6.77	3.89	3.73	28.94	10.97	18.76	11.17	15.74	7.50
				Mid N									
N Form	Bond	Peak Energy (eV)	Transition	OM-60	py-350	py-500	py-700	e-350	e-500	e-700	tol-350	tol-500	tol-700
Aromatic C=N in 6-membered ring (putative)	C=N	398.10	1s→π*		2.98	8.80	9.46	2.14	7.88	11.11	0.75	0.00	0.00
Aromatic C=N in 6-membered ring (1&2N)	C=N	398.78	1s→π*		8.71	15.47	8.10	12.92	19.32	6.18	4.06	3.85	0.39
Aromatic C=N in 6-membered oxygenated ring (2N)	C=N	399.40	1s→π*		6.83	2.26	14.66	9.30	2.50	20.05	7.96	4.36	1.24
Aromatic C=N in 5-membered ring (2N)	C=N	399.93	1s→π*		8.28	10.70	6.47	1.75	7.71	1.28	4.76	3.78	11.34
Nitrile	C≡N	400.00	1s→π*		0.00	0.00	0.00	0.00	0.00	0.00	0.00	4.99	0.00
Quaternary C-N in 6-membered ring	C-N	400.49	1s→π*		7.65	2.70	5.21	9.05	3.14	9.04	9.33	1.24	1.49
Aromatic C-N in 6-membered oxygenated ring (2N)	C-N	400.74	1s→π*		3.42	4.51	5.00	4.17	4.14	5.76	0.00	11.69	3.84
Non-aromatic C-N in 6-membered oxygenated ring (2N)	C-N	401.12	1s→π*		0.00	0.00	0.00	0.00	0.00	0.00	0.00	0.00	0.00
Aromatic C-N in 5-membered ring (2N)	C-N	401.30	1s→π*	37.11	13.70	15.65	12.42	18.74	16.92	14.51	9.88	8.88	17.65
Aromatic C-N in 5-membered ring (1N)	C-N	402.13	1s→π*	26.80	16.06	10.83	10.96	16.15	12.11	12.29	25.93	9.52	13.86
Aromatic C=N in 6-membered ring (1&2N, secondary peak)	C=N	402.54	1s→π*	2.74	4.54	5.44	2.71	4.28	4.29	1.54	2.92	16.37	4.54
Aliphatic C-NH ₂ bonded to aromatic 6-membered ring	C-NH ₂	403.00	1s→π*	17.03	9.70	8.54	7.78	12.25	11.18	10.82	18.45	9.97	31.27
Nitro C-NO ₂ bonded to aromatic ring	C-NO ₂	403.62	1s→π*	11.01	9.80	9.73	10.26	7.87	8.73	5.96	8.62	14.16	10.15
Aromatic N secondary peak	C=N	403.95	1s→π*	5.31	8.32	5.37	6.97	1.40	2.09	1.46	7.34	11.21	4.22
				High N									
N Form	Bond	Peak Energy (eV)	Transition	OM-60	py-350	py-500	py-700	e-350	e-500	e-700	tol-350	tol-500	tol-700
Aromatic C=N in 6-membered ring (putative)	C=N	398.10	1s→π*		2.38	n/a	10.48	3.24	8.41	10.74	0.85	0.00	2.31
Aromatic C=N in 6-membered ring (1&2N)	C=N	398.78	1s→π*		10.71	n/a	7.69	20.97	20.22	6.86	6.59	2.81	3.91
Aromatic C=N in 6-membered oxygenated ring (2N)	C=N	399.40	1s→π*		4.90	n/a	14.49	0.00	1.33	16.48	4.93	7.10	2.58
Aromatic C=N in 5-membered ring (2N)	C=N	399.93	1s→π*		10.29	n/a	5.90	9.24	9.59	2.23	7.47	5.79	8.09
Nitrile	C≡N	400.00	1s→π*		0.00	n/a	0.00	0.00	0.00	0.00	0.00	0.00	0.00
Quaternary C-N in 6-membered ring	C-N	400.49	1s→π*		4.94	n/a	5.80	2.70	1.28	6.85	0.94	6.01	4.78
Aromatic C-N in 6-membered oxygenated ring (2N)	C-N	400.74	1s→π*		4.39	n/a	3.36	5.09	5.56	5.59	10.85	5.01	0.00
Non-aromatic C-N in 6-membered oxygenated ring (2N)	C-N	401.12	1s→π*		0.00	n/a	0.00	0.00	0.00	0.00	0.00	0.00	0.00
Aromatic C-N in 5-membered ring (2N)	C-N	401.30	1s→π*	27.87	16.21	n/a	13.66	21.18	16.53	15.48	20.87	2.88	13.66
Aromatic C-N in 5-membered ring (1N)	C-N	402.13	1s→π*	19.20	17.19	n/a	12.24	15.18	10.69	11.65	10.80	11.56	19.82
Aromatic C=N in 6-membered ring (1&2N, secondary peak)	C=N	402.54	1s→π*	5.58	4.00	n/a	2.21	2.38	8.21	2.31	5.67	11.96	2.99
Aliphatic C-NH ₂ bonded to aromatic 6-membered ring	C-NH ₂	403.00	1s→π*	12.13	7.72	n/a	9.76	12.27	8.56	11.87	13.24	16.25	27.52
Nitro C-NO ₂ bonded to aromatic ring	C-NO ₂	403.62	1s→π*	11.45	14.01	n/a	9.79	6.68	9.62	7.42	8.66	11.47	9.93
Aromatic N secondary peak	C=N	403.95	1s→π*	23.78	3.25	n/a	4.63	1.06	0.00	2.50	9.13	19.16	4.42

Table B. 8: Proportion of absorption regions (%) of N bonds measured with N K-edge NEXAFS for willow wood OM and PyOM components.

				Low N									
N Form	Bond	Peak Energy (eV)	Transition	OM-60	py-350	py-500	py-700	e-350	e-500	e-700	tol-350	tol-500	tol-700
Aromatic C=N in 6-membered ring (putative)	C=N	398.10	1s → π*		1.41	7.09	10.30	0.55	5.45	4.44	0.00	0.42	0.00
Aromatic C=N in 6-membered ring (1&2N)	C=N	398.78	1s → π*		7.44	9.39	5.54	8.94	12.28	4.75	0.00	2.31	0.28
Aromatic C=N in 6-membered oxygenated ring (2N)	C=N	399.40	1s → π*		3.98	1.74	9.18	3.77	0.85	4.77	2.68	2.55	2.44
Aromatic C=N in 5-membered ring (2N)	C=N	399.93	1s → π*		5.68	6.44	0.00	6.91	6.72	3.43	0.00	1.86	0.00
Nitrile	C≡N	400.00	1s → π*		0.00	0.00	3.20	0.00	0.00	0.00	2.12	1.77	1.18
Quaternary C-N in 6-membered ring	C-N	400.49	1s → π*		7.22	6.67	6.18	7.83	7.07	8.07	0.00	1.58	0.00
Aromatic C-N in 6-membered oxygenated ring (2N)	C-N	400.74	1s → π*		0.00	0.00	0.00	0.00	0.00	0.00	11.09	4.86	9.69
Non-aromatic C-N in 6-membered oxygenated ring (2N)	C-N	401.12	1s → π*		0.00	0.00	0.00	0.00	0.00	0.00	10.07	11.64	10.46
Aromatic C-N in 5-membered ring (2N)	C-N	401.30	1s → π*	34.09	19.47	17.19	17.35	18.48	17.40	13.14	10.24	6.75	9.74
Aromatic C-N in 5-membered ring (1N)	C-N	402.13	1s → π*	28.82	18.02	15.54	15.41	17.33	16.64	17.05	13.49	4.86	7.80
Aromatic C=N in 6-membered ring (1&2N, secondary peak)	C=N	402.54	1s → π*	4.13	3.53	9.12	2.41	4.34	2.85	6.07	8.26	7.50	12.56
Aliphatic C-NH ₂ bonded to aromatic 6-membered ring	C-NH ₂	403.00	1s → π*	18.34	13.32	10.37	17.52	11.46	16.20	17.95	17.45	6.56	10.01
Nitro C-NO ₂ bonded to aromatic ring	C-NO ₂	403.62	1s → π*	14.62	9.91	13.59	9.50	12.29	12.35	14.26	14.17	7.66	0.72
Aromatic N secondary peak	C=N	403.95	1s → π*	0.00	10.01	2.86	3.40	8.08	2.19	6.08	10.43	39.69	35.11
				Mid N									
N Form	Bond	Peak Energy (eV)	Transition	OM-60	py-350	py-500	py-700	e-350	e-500	e-700	tol-350	tol-500	tol-700
Aromatic C=N in 6-membered ring (putative)	C=N	398.10	1s → π*		2.06	6.19	11.08	1.58	7.66	9.77	8.66	0.00	1.36
Aromatic C=N in 6-membered ring (1&2N)	C=N	398.78	1s → π*		11.68	15.49	4.54	10.38	13.97	4.58	4.29	2.22	3.70
Aromatic C=N in 6-membered oxygenated ring (2N)	C=N	399.40	1s → π*		2.94	0.16	7.23	3.82	0.88	5.80	9.48	2.09	4.61
Aromatic C=N in 5-membered ring (2N)	C=N	399.93	1s → π*		9.29	9.36	3.78	8.66	8.39	3.68	4.59	1.68	4.59
Nitrile	C≡N	400.00	1s → π*		0.00	0.00	0.00	0.00	0.00	0.00	0.00	0.32	0.00
Quaternary C-N in 6-membered ring	C-N	400.49	1s → π*		2.22	1.64	6.37	4.08	3.78	7.93	4.32	0.00	5.82
Aromatic C-N in 6-membered oxygenated ring (2N)	C-N	400.74	1s → π*		4.80	2.90	2.66	2.58	1.75	0.00	8.48	15.32	5.96
Non-aromatic C-N in 6-membered oxygenated ring (2N)	C-N	401.12	1s → π*		0.00	0.00	0.00	0.00	0.00	0.00	0.00	0.00	0.00
Aromatic C-N in 5-membered ring (2N)	C-N	401.30	1s → π*	42.52	17.70	19.05	16.52	20.30	18.08	15.03	16.06	17.45	13.19
Aromatic C-N in 5-membered ring (1N)	C-N	402.13	1s → π*	22.97	19.39	16.17	16.49	19.06	14.05	14.76	13.33	13.96	18.18
Aromatic C=N in 6-membered ring (1&2N, secondary peak)	C=N	402.54	1s → π*	1.69	2.53	3.58	3.16	3.73	3.92	6.16	7.81	6.74	7.76
Aliphatic C-NH ₂ bonded to aromatic 6-membered ring	C-NH ₂	403.00	1s → π*	22.56	11.55	11.80	14.29	14.45	15.44	14.81	13.20	25.20	13.47
Nitro C-NO ₂ bonded to aromatic ring	C-NO ₂	403.62	1s → π*	8.57	10.30	10.47	10.95	8.23	10.22	12.45	6.68	11.64	11.17
Aromatic N secondary peak	C=N	403.95	1s → π*	1.70	5.54	3.20	2.93	3.11	1.86	5.03	3.12	3.38	10.19
				High N									
N Form	Bond	Peak Energy (eV)	Transition	OM-60	py-350	py-500	py-700	e-350	e-500	e-700	tol-350	tol-500	tol-700
Aromatic C=N in 6-membered ring (putative)	C=N	398.10	1s → π*		4.74	6.79	12.35	1.25	7.59	11.12	0.00	0.00	0.92
Aromatic C=N in 6-membered ring (1&2N)	C=N	398.78	1s → π*		18.20	15.95	4.74	12.21	13.30	4.94	0.00	1.86	1.78
Aromatic C=N in 6-membered oxygenated ring (2N)	C=N	399.40	1s → π*		0.83	0.72	6.46	1.80	0.91	6.06	2.30	3.14	4.13
Aromatic C=N in 5-membered ring (2N)	C=N	399.93	1s → π*		12.04	9.91	4.64	8.72	9.39	4.41	0.00	0.00	0.00
Nitrile	C≡N	400.00	1s → π*		0.00	0.00	0.00	0.00	0.00	0.00	0.00	5.25	0.00
Quaternary C-N in 6-membered ring	C-N	400.49	1s → π*		1.36	2.29	5.94	2.15	2.68	6.08	7.18	1.47	4.04
Aromatic C-N in 6-membered oxygenated ring (2N)	C-N	400.74	1s → π*		4.41	2.90	1.98	3.66	2.97	3.77	15.39	9.29	9.86
Non-aromatic C-N in 6-membered oxygenated ring (2N)	C-N	401.12	1s → π*		0.00	0.00	0.00	0.00	0.00	0.00	7.41	0.00	0.00
Aromatic C-N in 5-membered ring (2N)	C-N	401.30	1s → π*	36.03	22.38	16.25	16.83	17.87	16.05	13.92	18.74	22.60	22.07
Aromatic C-N in 5-membered ring (1N)	C-N	402.13	1s → π*	32.79	14.34	9.64	15.66	16.82	14.62	15.60	5.30	8.71	11.83
Aromatic C=N in 6-membered ring (1&2N, secondary peak)	C=N	402.54	1s → π*	1.63	2.18	11.04	2.93	5.37	3.34	4.08	11.95	8.69	8.67
Aliphatic C-NH ₂ bonded to aromatic 6-membered ring	C-NH ₂	403.00	1s → π*	18.83	9.72	6.69	13.98	13.06	12.96	12.37	11.35	18.26	20.87
Nitro C-NO ₂ bonded to aromatic ring	C-NO ₂	403.62	1s → π*	10.72	6.63	14.70	11.50	9.50	10.63	12.14	13.80	11.04	10.36
Aromatic N secondary peak	C=N	403.95	1s → π*	0.00	3.16	3.14	2.99	7.58	5.56	5.51	6.59	9.70	5.47

Table B. 9: Proportion of absorption regions (%) of N bonds measured with N K-edge NEXAFS for willow leaf OM and PyOM components.

				Low N									
N Form	Bond	Peak Energy (eV)	Transition	OM-60	py-350	py-500	py-700	e-350	e-500	e-700	tol-350	tol-500	tol-700
Aromatic C=N in 6-membered ring (putative)	C=N	398.10	1s → π*		2.98	8.26	13.62	1.52	7.59	11.17	0.00	0.00	0.00
Aromatic C=N in 6-membered ring (1&2N)	C=N	398.78	1s → π*		13.35	16.37	5.99	8.50	13.55	7.16	0.92	0.00	4.07
Aromatic C=N in 6-membered oxygenated ring (2N)	C=N	399.40	1s → π*		1.02	0.89	6.98	4.16	6.30	9.61	9.98	3.08	4.97
Aromatic C=N in 5-membered ring (2N)	C=N	399.93	1s → π*		11.32	9.81	5.29	6.89	9.01	5.29	0.00	2.34	2.57
Nitrile	C≡N	400.00	1s → π*		0.00	0.00	0.00	0.00	0.00	0.00	1.48	2.16	4.26
Quaternary C-N in 6-membered ring	C-N	400.49	1s → π*		1.33	1.61	6.02	6.66	3.43	6.49	2.71	2.25	1.86
Aromatic C-N in 6-membered oxygenated ring (2N)	C-N	400.74	1s → π*		2.98	3.38	1.28	0.75	5.42	4.09	8.95	6.46	8.47
Non-aromatic C-N in 6-membered oxygenated ring (2N)	C-N	401.12	1s → π*		0.00	0.00	0.00	0.00	0.00	0.00	0.00	0.00	0.00
Aromatic C-N in 5-membered ring (2N)	C-N	401.30	1s → π*	36.42	23.40	18.82	18.36	19.27	14.33	11.77	16.40	13.47	12.48
Aromatic C-N in 5-membered ring (1N)	C-N	402.13	1s → π*	25.02	18.18	15.70	15.46	16.28	11.77	13.89	12.81	16.60	13.61
Aromatic C=N in 6-membered ring (1&2N, secondary peak)	C=N	402.54	1s → π*	6.58	3.70	2.88	2.57	5.03	4.78	4.73	6.97	8.46	10.58
Aliphatic C-NH ₂ bonded to aromatic 6-membered ring	C-NH ₂	403.00	1s → π*	16.59	11.14	10.46	12.04	10.74	6.43	11.03	12.78	17.51	10.20
Nitro C-NO ₂ bonded to aromatic ring	C-NO ₂	403.62	1s → π*	15.40	8.84	8.12	9.56	12.75	13.13	10.10	13.24	12.72	14.15
Aromatic N secondary peak	C=N	403.95	1s → π*	0.00	1.75	3.69	2.82	7.47	4.27	4.66	13.77	14.96	12.78
				Mid N									
N Form	Bond	Peak Energy (eV)	Transition	OM-60	py-350	py-500	py-700	e-350	e-500	e-700	tol-350	tol-500	tol-700
Aromatic C=N in 6-membered ring (putative)	C=N	398.10	1s → π*		6.58	7.59	12.23	3.92	8.77	11.39	0.49	0.00	0.00
Aromatic C=N in 6-membered ring (1&2N)	C=N	398.78	1s → π*		18.86	18.45	7.94	13.26	15.43	7.99	5.68	2.61	2.66
Aromatic C=N in 6-membered oxygenated ring (2N)	C=N	399.40	1s → π*		1.29	0.57	6.93	1.56	4.46	9.23	7.49	7.40	5.42
Aromatic C=N in 5-membered ring (2N)	C=N	399.93	1s → π*		12.61	10.63	7.77	13.72	9.94	6.33	6.80	0.00	1.09
Nitrile	C≡N	400.00	1s → π*		0.00	0.00	0.00	0.00	0.00	0.00	0.00	5.42	4.69
Quaternary C-N in 6-membered ring	C-N	400.49	1s → π*		1.49	1.89	5.11	1.34	3.47	6.61	7.50	6.27	1.95
Aromatic C-N in 6-membered oxygenated ring (2N)	C-N	400.74	1s → π*		6.56	2.84	1.83	4.12	4.40	3.93	5.40	8.68	8.02
Non-aromatic C-N in 6-membered oxygenated ring (2N)	C-N	401.12	1s → π*		0.00	0.00	0.00	0.00	0.00	0.00	0.00	0.00	0.00
Aromatic C-N in 5-membered ring (2N)	C-N	401.30	1s → π*	54.53	19.15	18.35	18.30	23.98	15.23	12.82	17.33	10.13	12.13
Aromatic C-N in 5-membered ring (1N)	C-N	402.13	1s → π*	25.15	21.58	14.40	14.92	15.53	11.44	14.07	15.05	17.83	14.69
Aromatic C=N in 6-membered ring (1&2N, secondary peak)	C=N	402.54	1s → π*	0.74	0.00	3.00	3.39	1.27	1.26	2.31	4.86	4.88	9.79
Aliphatic C-NH ₂ bonded to aromatic 6-membered ring	C-NH ₂	403.00	1s → π*	14.88	5.84	10.70	10.42	12.23	15.02	11.56	12.85	13.46	13.10
Nitro C-NO ₂ bonded to aromatic ring	C-NO ₂	403.62	1s → π*	4.71	4.82	7.81	9.58	7.64	7.09	10.59	10.72	13.83	16.30
Aromatic N secondary peak	C=N	403.95	1s → π*	0.00	1.23	3.76	1.57	1.41	3.50	3.19	5.82	9.49	10.17
				High N									
N Form	Bond	Peak Energy (eV)	Transition	OM-60	py-350	py-500	py-700	e-350	e-500	e-700	tol-350	tol-500	tol-700
Aromatic C=N in 6-membered ring (putative)	C=N	398.10	1s → π*		2.55	7.61	14.44	3.43	6.93	11.92	0.00	1.45	1.21
Aromatic C=N in 6-membered ring (1&2N)	C=N	398.78	1s → π*		13.83	18.72	6.42	12.19	17.09	8.16	6.63	4.07	3.59
Aromatic C=N in 6-membered oxygenated ring (2N)	C=N	399.40	1s → π*		0.64	1.24	8.91	4.12	3.95	9.48	3.95	5.21	4.62
Aromatic C=N in 5-membered ring (2N)	C=N	399.93	1s → π*		11.93	11.21	6.12	9.20	11.35	6.76	6.99	5.08	4.48
Nitrile	C≡N	400.00	1s → π*		0.00	0.00	0.00	0.00	0.00	0.00	0.00	3.45	3.29
Quaternary C-N in 6-membered ring	C-N	400.49	1s → π*		0.95	1.79	4.97	4.82	2.80	6.15	0.75	2.80	1.99
Aromatic C-N in 6-membered oxygenated ring (2N)	C-N	400.74	1s → π*		3.04	4.14	4.80	3.50	4.69	4.07	8.52	6.97	8.50
Non-aromatic C-N in 6-membered oxygenated ring (2N)	C-N	401.12	1s → π*		0.00	0.00	0.00	0.00	0.00	0.00	0.00	0.00	0.00
Aromatic C-N in 5-membered ring (2N)	C-N	401.30	1s → π*	39.73	23.37	18.45	15.72	18.38	15.75	13.20	21.09	16.44	16.43
Aromatic C-N in 5-membered ring (1N)	C-N	402.13	1s → π*	26.24	18.35	13.18	14.35	17.43	10.79	13.69	10.63	11.71	12.29
Aromatic C=N in 6-membered ring (1&2N, secondary peak)	C=N	402.54	1s → π*	6.47	3.50	2.50	2.70	2.03	3.59	2.72	7.46	7.29	5.64
Aliphatic C-NH ₂ bonded to aromatic 6-membered ring	C-NH ₂	403.00	1s → π*	15.72	11.25	11.67	10.02	9.60	9.16	11.00	14.88	11.68	14.29
Nitro C-NO ₂ bonded to aromatic ring	C-NO ₂	403.62	1s → π*	11.84	8.56	6.72	8.51	8.20	9.30	9.67	9.91	13.34	13.28
Aromatic N secondary peak	C=N	403.95	1s → π*	0.00	2.02	2.79	3.04	7.09	4.60	3.17	9.18	10.51	10.39

Reference

Cheng C.-H., Lehmann J., Thies J. E. and Burton S. D. (2008) Stability of black carbon in soils across a climatic gradient. *J. Geophys. Res. Biogeosciences* **113**, G02027.